Department of Mechanics, Mathematics and Management

MECHANICAL AND MANAGEMENT ENGINEERING
PH.D. PROGRAM

SSD: ING-IND/14 - MECHANICAL DESIGN AND MACHINE CONSTRUCTION
ING-INF/01 - ELECTRONICS

Final dissertation

Integrated optomechanical devices for sensing

by
MARTINO DE CARLO

Supervisors:
Prof. Vittorio M. N. PASSARO
Prof. Luciano LAMBERTI

Coordinator of the Ph.D. Program:
Prof. Giuseppe P. Demelio

Course n°33, 01/11/2017 - 31/10/2020

Department of Mechanics, Mathematics and Management

MECHANICAL AND MANAGEMENT ENGINEERING
PH.D. PROGRAM

SSD: ING-IND/14 - MECHANICAL DESIGN AND MACHINE CONSTRUCTION
ING-INF/01 - ELECTRONICS

Final dissertation

Integrated optomechanical devices for sensing

by
MARTINO DE CARLO

<u>Referees:</u>

Prof. Carlos A. Barrios

Prof. Wolfgang Osten

<u>Supervisors:</u>

Prof. Vittorio M. N. PASSARO

Prof. Luciano LAMBERTI

Coordinator of the Ph.D. Program:
Prof. Giuseppe P. Demelio

Course n°33, 01/11/2017 - 31/10/2020

alla mia famiglia
e ad Annalisa

Acknowledgements

Firstly, I would like to express my sincere gratitude to my supervisors for their support over the three years of my PhD. I would like to thank Prof. Vittorio Passaro for guiding, inspiring, helping and aiding me during all the time of research and the writing of the thesis. I am grateful to Prof. Luciano Lamberti for his motivation, his profound belief in my work and his experienced advices in technical subjects. Then, I would like to thank the PhD coordinator, Prof. Giuseppe Pompeo Demelio, for his availability and support during my PhD course.

My sincere thanks also goes to Prof. Francesco De Leonardis for our constructive technical and non-technical talks, for his advices and his ability to find an answer to all my questions and the patience to solve even my most trivial doubts.

I am also grateful to Goran Mashanovich, Milos Nedeljkovic and all the people of the Silicon Photonics Group I met at the Optoelectronics Research Centre of the University of Southampton, who helped me and made me feel at home during my period abroad.

Then, I would like to thank the group “I pirati di Carrassi”, for our productive breaks, exciting challenges and hilarious moments at lunchtime. Thanks also to all the students of my PhD Course for the coffees, the summer school and the nights spent together.

I deeply thank my parents and my sister, for their trust and their patience, for their support and their encouragement during these three years, which helped me achieve my objectives in the most positive way.

A final thanks goes to Annalisa, who has always been present during all my university studies, who listened with curiosity to all the technical topics I wanted to share with her, who helped me in doubtful moments, who believed and believes in me more than I do.

Contents

List of Figures

List of Tables

Introduction to optomechanics

Optomechanics is a developing field of research exploring the interaction between light and mechanical motion. The modern nanofabrication techniques for mechanical devices and ultralow dissipation optical structures have provided a way for giving an important experimental progress to optomechanics, both for applications and for fundamental investigations. In this thesis Optomechanics will be investigated in several different aspects, in its general meaning, both theoretically and experimentally.

There are different ways in which light and mechanics interact with each other (Figure 1). In this thesis three different areas of Optomechanics will be examined. The interaction between light and mechanical motion will be investigated starting from the concept of optical gyroscopes. Optical gyroscopes are sensors of angular velocity. In the present state of the art, the physical principles and the configurations used for realizing optical gyroscopes are not suitable for miniaturizing them to the microscale. So, some new configurations exploiting the concept of "exceptional points" will be here presented.

Secondly, the concept of optomechanical forces will be investigated in the following chapter. A new generalized energetic model to evaluate optical forces will be developed to provide an easy way to design new optomechanical devices. A modelling of the dynamics of optomechanically coupled waveguides will be investigated analytically and numerically. Then, an experimental work about an optomechanical switch will be presented, to demonstrate the feasibility of a new generation of optomechanical devices in optical networks and for different applications.

Finally, Photoacoustic Spectroscopy will be analysed in the last chapter. The state-of-art Quartz-Enhanced PhotoAcoustic Spectroscopy (QEPAS) sensor will be modelled and simulated and a proposal for a new semi-integrated sensor will be presented.

Here a brief background on the three subjects developed in the next chapters is presented. Moreover, some principles of fabrication technology is given, to clarify the fabrication steps involved in the fabrication all the devices presented in this thesis.

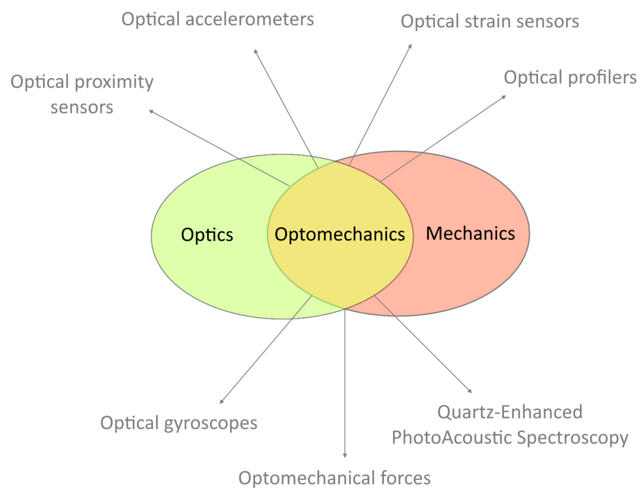

Figure 1: Graphical visualization of Optomechanics, with some examples of applications.

Optical gyroscopes

Sensors for angular velocity

The gyroscope, which measures angular velocity around a fixed axis with respect to an inertial space, is a key sensor in modern navigation systems enabling the possibility to plan, record and control the movement of a vehicle from one place to another [1].

There are three main categories of gyroscopes: spinning mass gyroscopes, optical gyroscopes and vibrating gyroscopes. In the first category, all the devices with a mass spinning steadily with respect to a free movable axis are included. Optical gyroscopes are based on the Sagnac effect. Finally, vibrating gyros are based on Coriolis effect, inducing a coupling between two resonant modes of a mechanical resonator [1].

Spinning mass gyroscope

The first conception of a gyroscope is the mechanical one using a spinning mass. A mechanical gyroscope essentially consists of a spinning mass that rotates around its axis. In particular, when the mass is rotating on its axis, it tends to remain parallel to itself and to oppose any attempt to change its orientation. This mechanism was invented in 1852 by physicist Léon Foucault during his studies of the Earth's rotation [2]. When the system is suspended and free to rotate, its spinning axis will remain oriented in the same direction, even if the external frame is changing direction. When the axis is forced to change direction, the system reacts with a counterbalancing torque related to the angular velocity imposed to the frame. By constraining the spinning mass to the rotating frame through a known stiffness, the emerging torque can be retrieved and the angular velocity of the frame can be indirectly measured (Figure 2a). This is called "rate mechanical gyroscope".

Vibrating gyroscopes

Vibrating gyroscopes generally use a vibrating mechanical part as a sensing element for detecting the angular velocity [2]. They do not have rotating parts that require bearings and this enables an easy miniaturization and the use of the manufacturing techniques typical of MEMS (Micro Electro Mechanical Systems) devices. All MEMS gyroscopes with vibrating element are based on the transfer of energy between two vibration modes caused by the acceleration of Coriolis. [2] The Coriolis acceleration, proportional to the angular velocity, is an apparent acceleration that is observed in a rotating frame of reference and can be used to sense the angular velocity of the frame.

Sagnac gyroscope

Optical gyroscopes are based on the Sagnac effect, which states that the phase shift between counterpropagating optical waves in a rotating ring interferometer is proportional to the angular velocity of the structure around the axis perpendicular to the ring. In 1963 the first Ring Laser Gyroscope was fabricated [3], using mirrors to create the Sagnac loop. Then, fibre solutions to exploit the Sagnac effect have been developed, called Fibre Optic Gyroscopes (FOGs). The trend of the recent years of miniaturizing sensors to save space, weight and money, lead to the interest in the possibility of the integration of gyroscopes. The miniaturazion of spinning mass gyroscope presents different technological problems. Differently, vibrating and optical gyroscopes can be effectively miniaturized, leading to MEMS and integrated optical gyroscopes. However, there is an intrinsic limit in a further miniaturization of MEMS gyroscopes up to micro- and nanometric dimensions: the sensitivity of the sensor depends on the physical mass of the inertial part of the device. Whereas, the limit in a further integration of optical gyroscopes to the micrometric scale is that in the Sagnac effect the phase shift between counterpropagating waves is proportional to the radius of the ring. So, a different approach is necessary to develop a new generation of gyroscopes, that can be scaled to micrometric and nanometric dimensions.

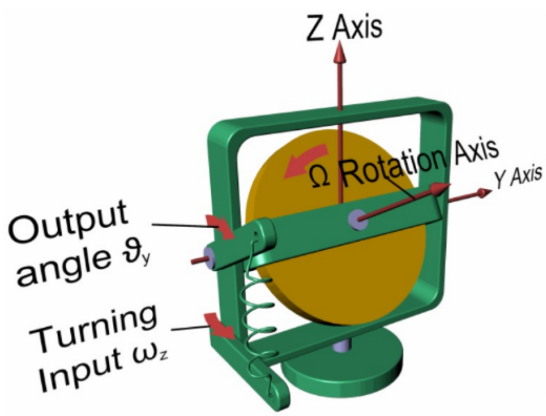

(a)

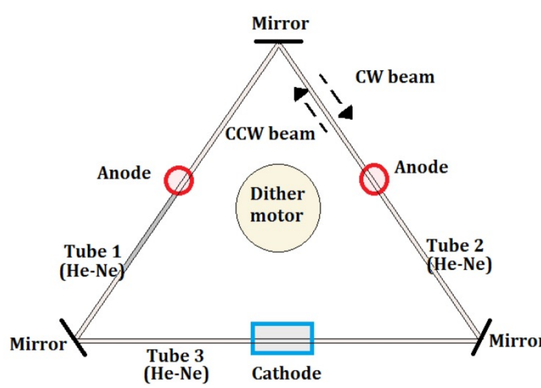

(b)

Figure 2: Spinning mass gyroscope [2] (a). Ring Laser Gyroscope [2] (b).

Recent advances in the integration of optical gyroscopes

There are many applications where angular velocities in the range of 0.1-100°/h need to be detected. Despite ring laser gyroscopes can easily reach such a precision, it is out of reach in fully integrated platforms, where the area of the loop is generally smaller. Moreover, the resolution of optical gyroscopes is often limited by the lock-in effect, due to unwanted coupling between the two counterpropagating modes [4]. Currently, several research groups are trying to implement chip-scale laser gyroscopes. One approach uses a Mach-Zehnder Interferometer into the coupling region between a ring resonator and a straight waveguide. [5] An alternative solution is an integrated resonant optical gyroscope constructed by active long-range surface plasmon-polariton (LRSPP) waveguide resonator [6]. In [7], a monolithic micro cavity is shown, capable of detecting rotations as low as 22 deg/h using counterpropagating laser fields. The proof-of-concept gyroscope features an 18-mm silica-on-silicon disk resonator with an intrinsic Q-factor over 200 million. In [8] a novel highly integrated optical gyroscope using low loss silicon nitride waveguides is proposed and analysed. Active three-dimensional vertically coupled resonators have been proposed in [9] to be used as a gyroscope, the sensitivity of which is enhanced by loss compensation, unidirectional propagation and large sensing area, while maintaining the same bulk volume. In [10] a gyroscope structure with tailored local dispersion profile to enhance sensitivity has been proposed, which uses lithium niobate (LiNbO3) thin film as the on-chip material of gyroscope resonator. The structure of the gyroscope proposed in [11] is claimed to achieve very high sensitivities, reaching a theoretical sensitivity enhancement of 10^6 with respect to a classical Sagnac gyroscope, by exploiting the concept of parity-time symmetry. Moreover, it overcomes the problem of the lock-in effect, using only unidirectional waves.

Contribution of this thesis

The contribution of this thesis in the field of optical gyroscopes will start by analysing the parity-time symmetric solution proposed by [11]. It will be shown that in such configuration, a real splitting is not visible in the spectrum of the light exiting the gyroscope, when set in rotation. This is due to the presence of the imaginary part of the complex eigenfrequencies on the output spectrum. It will be shown that, differently from what is claimed in [11], the output transfer function of the light exiting the device does not exhibit any spectral splitting. It will be demonstrated, instead, that the full width at half maximum (FWHM) of the output transfer function is proportional to the square root of the angular velocity of the frame if the system is designed to be at the exceptional point. These results have been published in [12]. Secondly, a new configuration about an anti-parity-time symmetric gyroscope will be proposed. Anti-parity-time symmetry will be investigated as a new solution for solving the problem of the integration of angular velocity sensors. In particular, it will be demonstrated that anti-parity-time-symmetric gyroscope presents several advantages in terms of easiness of readout and stability with respect to the parity-time-symmetric one. The used device exploits a U-shaped configuration to indirectly couple two optical resonators. The anti-parity-time-symmetric gyroscope here proposed has been published in [13]. Thirdly, another new configuration for an anti-parity-time-symmetric gyroscope will be presented. The main advantage of this configuration with respect to the one with the U-shaped waveguide is the fabrication robustness.

Optomechanical forces

A brief history

The term "optomechanics" is recently being adopted especially for the particular area of this subject dealing with optomechanical forces. Optical forces are very feeble forces that manifest themselves only in particular conditions (e.g. during star formation) [14]. Light, in fact, carries a momentum, that can be transferred to material objects. The tails of the comets are one of the examples of the manifestation of optical forces. Being the forces of the order of pico- and nanonewtons per milliwatt, the applications of these forces are especially interesting in integrated devices. The trend of the miniaturization of devices and sensors reaching the microscale is perfectly compatible with the orders of magnitude of optomechanical forces. Optical forces are usually divided into two categories: radiation pressure, acting along the direction of propagation of light, and optical gradient force, acting transversely to the direction of propagation of light.

The concept that electromagnetic radiation can exert a force on material objects was theoretically predicted by Maxwell [15], and the radiation pressure of light was first observed experimentally more than a century ago [16].

Braginskiǐ firstly investigated the ability of radiation pressure to provide cooling for large objects [17]. He considered the dynamical influence of radiation pressure on a suspended end mirror of an optical cavity. With his analysis, the retarded nature of the force was revealed, due to the finite cavity lifetime. Such effect resulted on damping or antidamping of mechanical motion, that he demonstrated using a microwave cavity.

In the 1970s, Ashkin demonstrated that focused laser beams can trap and control dielectric particles, including feedback cooling [18]. In 2018 Ashkin was awarded a Nobel Prize in Physics for his work on optical trapping.

In 1975, the non-conservative nature of radiation pressure force and the consequent possibility of using it for cooling atomic motion were pointed out [19, 20]. Consequently, laser cooling was experimentally realized in 1980s, becoming an important technique [21]

Recently, the interest for optomechanical devices has led to a lot of work about the manipulation of the center-of-mass of motion of mechanical oscillator, including macroscopic mirrors in the Laser Interferometer Gravitation Wave Observatory (LIGO) project [22], nano- or micromechanical cantilevers [23, 24, 25], vibrating microtoroids [26, 27] and membranes [28]. Cooling of motion has been demonstrated using positive radiation pressure damping, whereas negative damping permits parametric amplification of small forces [26, 29].

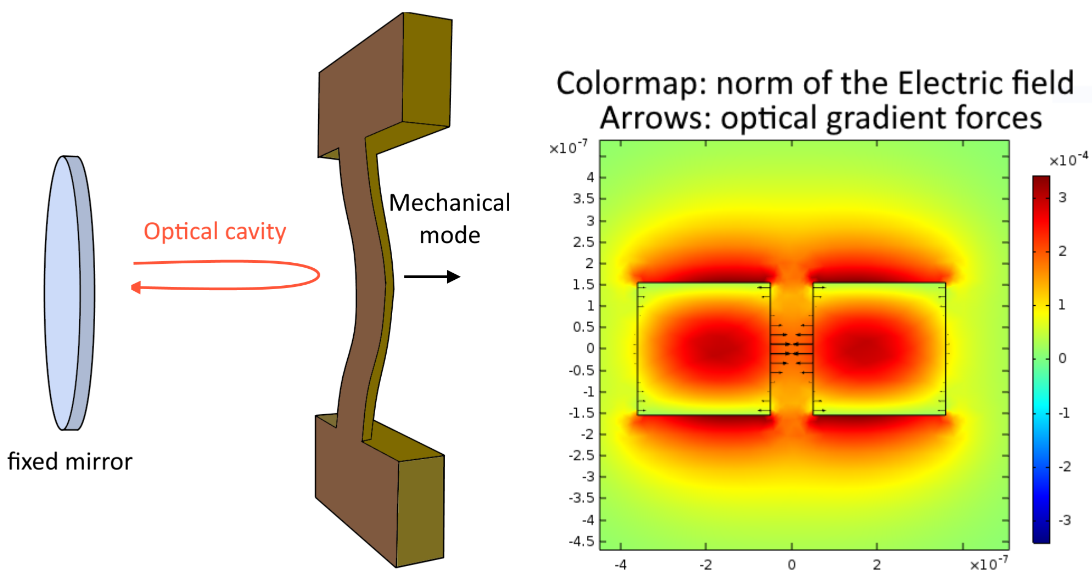

(a) (b)

Figure 3: Classical optomechanical cavity (a). Arrow lines representing optical gradient forces evaluated through Maxwell Stress Tensor (b).

Recent advances

Thanks to recent advances in nanophotonics, the dimensions of optical devices have been reduced to micro and nanometers, making optical actuation possible even for levels of power of microwatts [26]. In these cases, optical forces can be scaled to higher values through high-Q resonance enhancement [30, 31]. Such results paved the way to light-driven mechanically variable systems for trapping [32, 33], actuation [34, 31] and manipulation of nanoscale objects [32]. Since the optical state of a system is linked to its mechanical state, mechanical forces can be used to realize variable directional couplers [35, 33], parametric optical processes [26, 36, 31], ultra-widely tunable microcavities [32], and microcavity athermalization via self-adaptive optomechanical behaviours [32, 37]. The possibility to arrange an optical system to generate optical torques has been used to realize microscopic machines [38, 39, 40] and integrated light devices for actuation, trapping and sensing [41, 42, 43, 44].

In order to proper design such optomechanical systems, an easy tool is needed. In fact, Maxwell Stress Tensor (MST) is well known to be useful for calculating optical forces, but it is computationally expensive, especially in complex systems with resonant architectures (three-dimensional FDTD needs to be performed). Moreover, the MST method is reliable, but it is not intuitive to design a system with a desired optical force profile. In [45], Rakich developed a general analytical formalism which can handle the calculation of optical forces in complex optical systems. Before the Response Theory of Optical Forces (or RTOF) by Rakich, the optical field distribution was needed for computing optical forces. The RTOF method enables the evaluation of optical forces in open lossless mechanically variable optical systems using a formalism which takes into account the energy and photon number conservation principles in the context of such systems.

It has been widely demonstrated that high-quality-factor resonant systems are interesting for the generation of large optical forces [30, 31].

Contribution of this thesis

In this thesis, a generalized version of RTOF method will be presented, which takes into account also the presence of gain or loss sources. Using the generalized RTOF method, it will be shown that resonant optical structures can produce a further enhancement of optical forces, when the system approaches the parity-time symmetry condition. These results have been published in [46]. Then, a proposal for the modelling of the dynamics of coupled suspended optical waveguides will be presented and a numerical algorithm to predict and design the transient behaviour of optomechanical devices will be shown. The results have been published in [47]. Finally, an experimental work on an optomechanical switch will be shown. The experiment includes the fabrication and the optical measurement, performed at the Optoelectronics Research Centre of the University of Southampton.

Quartz-Enhanced PhotoAcoustic Spectroscopy

Photoacoustic Spectroscopy

PhotoAcoustic Spectroscopy (PAS) is an indirect absorption spectroscopy based on the photoacoustic effect and typically using lasers as excitation sources [48]. When light at a specific wavelength is absorbed by the gas sample, the excited molecules will subsequently relax to the ground state either through emission of photons or by means of non-radiative processes. These processes produce localized heating in the gas, which in turn results in an increase of the local pressure. The local pressure contains information about the gas in the proximity of the light beam and its measurement can be used to calculate the composition of the gas mixture in its proximity. If the incident light intensity is modulated, the generation of thermal energy in the sample will also be periodic and a pressure wave, i.e. a sound wave, will be produced at the same frequency of the light modulation. The PAS signal can be amplified by tuning the modulation frequency to the acoustic resonance of the gas sample cell. The advantage is that no optical detector is needed for this technique and commercially available hearing aid microphones can be used to sense the sound waves. PAS has been successfully applied in trace gas sensing applications, which include atmospheric chemistry, volcanic activity, agriculture, industrial processes, workplace surveillance, and medical diagnostics.

Quartz-Enhanced PhotoAcoustic Spectroscopy

Quartz-Enhanced PhotoAcoustic Spectroscopy (QEPAS) is an alternative approach to PAS, using a quartz tuning fork (QTF) as a sharply resonant acoustic transducer [49] to detect weak photoacoustic excitation, thus permitting the use of very small volumes. QTFs have a quality factor of the order of 10^5 or higher in vacuum and 10^4 at normal atmospheric pressure [49]. Usually QTFs with resonant frequency of 32768 Hz are used. This means that the light is modulated at the same frequency, meaning an acoustic wavelength of around 1 cm. The only way to excite the QTF (with 1 mm distance between the two prongs) is to use a source located between the two QTF prongs, without touching them. To enhance the QEPAS signal and to confine the sound wave, a mechanical microresonator is employed. Usually it consists of two thin tubes aligned perpendicularly to the QTF plane (Figure 4). The complete module including the QTF sensor and the microresonator is called Acoustic Detection Module (ADM) [50, 51, 52]. It is critical for the laser beam entering the microresonator to avoid touching the walls of the resonator, to prevent photothermal effects. The overall quality factor of the system decreases with the use of microresonators, since the total losses increase. However, the intensity of the pressure signal is increased. Moreover, the laser beam must not hit the prongs of the QTF since otherwise a large undesirable non-zero background arises due to the laser contribution, hence limiting the sensor detection sensitivity [53]. This problem triggered several solutions, for instance the use of the Hollow Core Waveguides (HCW) to be coupled with the laser sources for guiding the light and clean up the laser beam mode profile [54, 55, 56].

The short optical pathlength, the capability to reach high detection sensitivity, high compactness and robustness represent the main distinct advantages which made QEPAS the leading-edge technique mature for out-of-laboratory operation, targeting in-situ applications such as environmental monitoring and leak detection [57, 58]. Nevertheless, for those applications in which sensors must work in challenging environments like downhole analysis of natural gas or early fire detection empowered by the drone technology, the further miniaturization step requires a different level of integration of the opto-acoustic components [59, 60, 61].

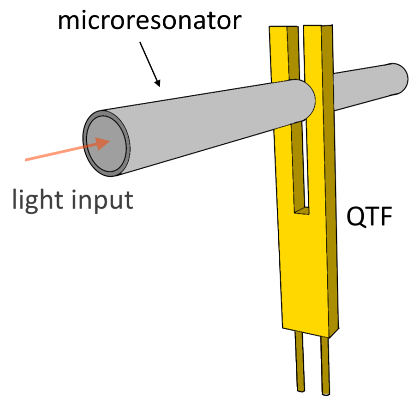

Figure 4: Acoustic Detection Module (ADM).

Contribution of this thesis

In this thesis a modelling of the QEPAS state-of-the-art sensor will be shown. Moreover, a new approach will be presented, aimed at miniaturizing the QEPAS sensor, making it available for those applications where compactness is a key requirement. Exploiting optical resonance and mechanical cavities, a semi-integrated version of the QEPAS sensor will be demonstrated to achieve performance comparable with the state-of-the-art sensor. These results have been published in [62]

Principles of Fabrication technology

All the thesis is focused on the integration of optomechanical devices. The fabrication processes behind the manufactoring of integrated devices make use of lithography to transfer a pattern on a resist and then transfer the pattern from the resist to a thin film of a material or a bulk substrate, through etching processes [63]

Photolithography and Electron-beam lithography

Nowadays, the most used approaches in lithography are photolithography and electron-beam lithography. Photolithography is a process using light to transfer a geometric pattern from an optical mask to photosensitive material called "photoresist" [64].

Electron-beam lithography (often abbreviated as e-beam lithography, EBL) is the practice of scanning a focused beam of electrons to draw custom shapes on a surface covered with an electron-sensitive film called “resist”. The electron beam changes the solubility of the resist, thus enabling the selective removal of the exposed or the non exposed region of the resist, when immersed in a solvent. [65]

The aim of both the lithography processes is to create very small structures in the resist that can be transferred to the material on the wafer, often by etching technique. The key advantage of the electron-beam lithography is the sub-10 nm resolution. Whereas the most important advantage of the photolithography is the presence of a photomask that can be reused for massive production.

Etching

The etching process consist in transferring the pattern from the resist to a thin film of material or to a substrate. Traditionally the process of etching consisted on the use of strong acid to cut the unprotected part of metal surfaces to create a design incised in the metal [66]. In modern manufactoring different chemicals are used and several materials can be incised. The etch-speed depends on the chemical used and on the material to be etched. Often, a calibration is needed before the etching process. Figure 5 shows the complete process of lithography and etching.

Deposition or growth

Sometimes etching is not sufficient to create a pattern we need on the microfabricated chip. The deposition of thin films of materials is needed for different applications [67]. For example, in optical devices a thin film of silicon dioxide is often used as cladding of optical waveguides. Some examples of deposition techniques are:

- Thermal oxidation
- Local oxidation of silicon
- Chemical vapor deposition (CVD)
- Physical Vapor Deposition
- Epitaxy

Micromachining

The recent industrial interest in Micro-Electro-Mechanical-Systems (MEMS) has increased the ability in microfabrication technologies as micromachining. The term micromachining refers to the fabrication of micromechanical structures with the aid of etching techniques to remove part of the substrate or a thin film [68]. Having excellent mechanical properties, silicon is an ideal material for micromachining and has been widely used in the field of MEMS. Usually techiniques as vapor HF etching or wet HF etching combined with Critical Point Drying (CPD) are required to selectively underetch thin films or the substrate.

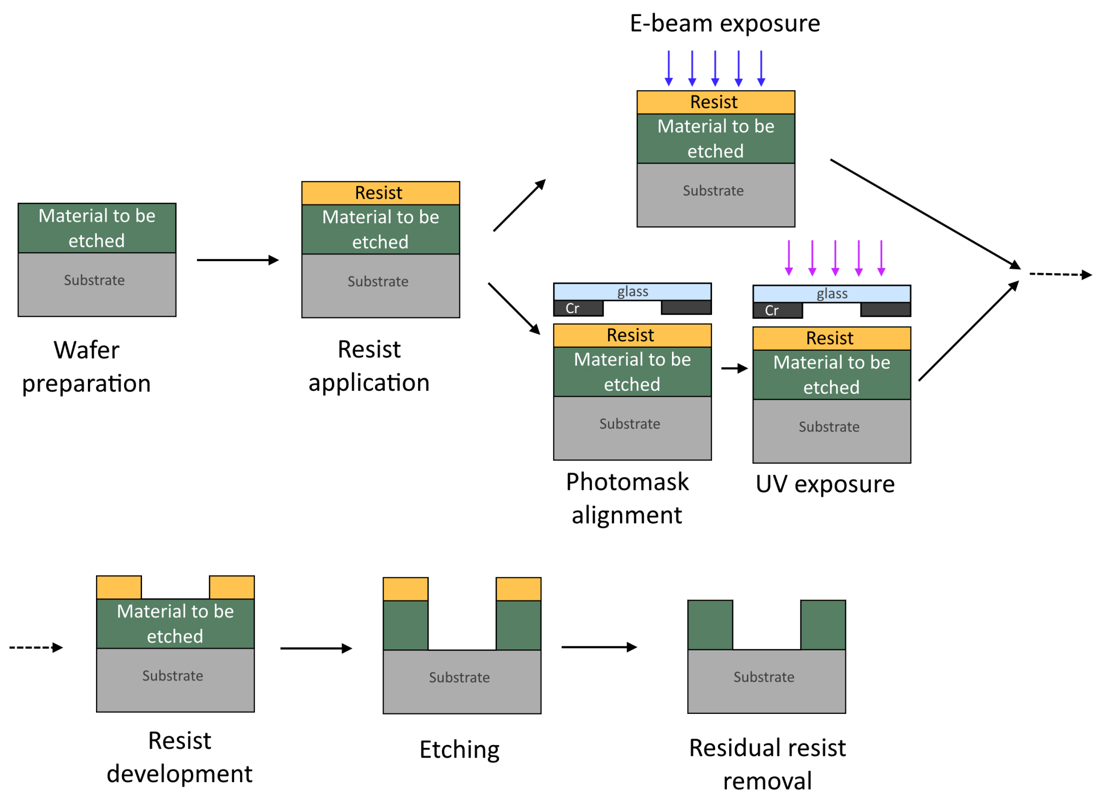

Figure 5: Microfabrication processes of integrated devices including lithography and etching.

Focused Ion Beam

A Scanning Electron Microscope (SEM) is a microscope that scans a focused beam of high-energy electrons to produce images of samples. A Focused Ion Beam (FIB) instrument is almost identical to a SEM, but uses a beam of ions rather than electrons [69]. At low beam currents, FIB can be used for imaging. However, unlike the SEM, the FIB is inherently destructive to the specimen. Consequently the focused ion beam can "mill" the specimen surface, via a sputtering process (Figure 6). Because of the sputtering capability, the FIB is used as micro- and nano-machining tool, to modify or machine materials at the micro- and the nanoscale. The smallest milled features are of the order of 10 nanometers.

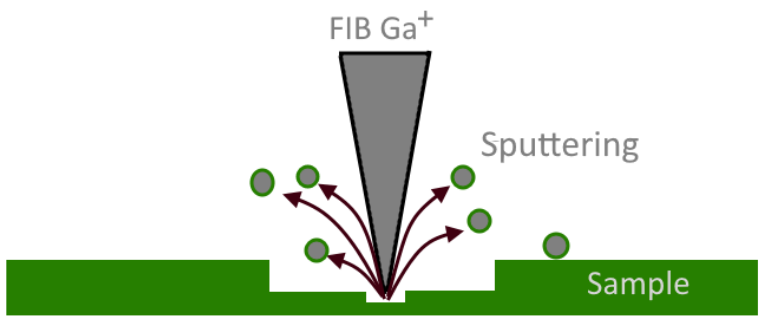

Figure 6: FIB milling process via a beam of Ga^{+} ions.

Chapter 1

Exceptional points for optical gyroscopes

In this chapter an overview about Sagnac gyroscopes will be shown. Then, new results about the modelling and the design of a parity-time-symmetric gyroscope will be presented. Next, a proposal about an anti-parity-time-symmetric-gyroscope will be shown. Finally, a different configuration about an anti-parity-time symmetric gyroscope will be presented.

1.0.1 Optical gyroscopes

Gyroscopes are devices mounted on a frame, able to sense angular velocity. There are different classes of gyroscopes, depending on the physical principles they use. Optical gyroscopes operate by sensing the difference in propagation time between counter-propagating beams travelling in opposite directions in closed or open optical paths. A rotation-induced change in the path lengths generates a phase difference between the counter-propagating light beams. This rotation-induced phase difference is called Sagnac effect, and is the basic operating principle of all optical gyroscopes [2]. Based on the measurement technique of the Sagnac effect, it is possible to classify optical gyroscopes. The two main different typologies of optical gyroscopes consist in active and passive architectures (see Figure 1.1). In the active configurations, the closed-loop optical path (i.e., the ring cavity) contains the optical source, forming a ring laser. The active configurations can be built in Bulk Optics or in Integrated

Optics technology, although only the Bulk Optics solutions have achieved commercial maturity. Among the ring laser gyros, there are different categories depending on the method employed to overcome the lock-in effect (a condition for which the active gyroscope response results insensitive to low rotation rates) which occurs at low rotational rates (tens of degrees/hour). Lock-in can be reduced by introducing a mechanical dither, a magneto-optic biasing, or by using of multiple optic frequencies configuration. Differently, in passive architectures, the optical source is external to the closed optical loop (i.e., a fibre coil) as in the Interferometric Fibre Optic Gyroscope. Ring Laser Gyroscopes and Interferometric Fibre Optic Gyroscopes, whose features differ in terms of size, weight, power requirements, performance, and cost, are the more diffused optical gyroscope technology. [2].

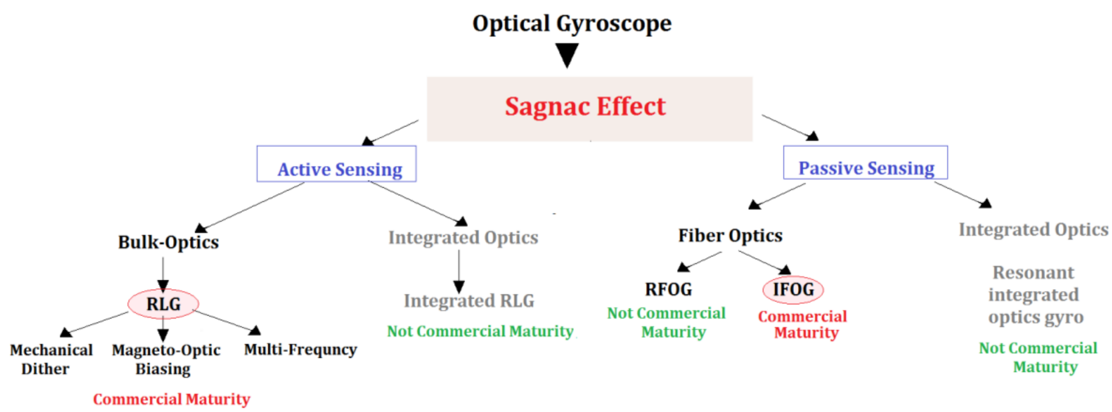

Figure 1.1: Classes of optical gyroscopes [2]

.

Sagnac effect

The Sagnac effect is the operating principle of almost all optical gyroscopes. It was discovered in 1913 by George Marc Sagnac as a result of the study of dynamics of Earth rotation by Michelson-Morley [70]. The effect manifests itself in a setup called "ring inteferometer". The relative phase between two optical beams counterpropagating in a ring structure changes of a quantity proportional to the angular velocity of the ring structure (which rotates over a rotational axis perpendicular to the plane of the structure). Let's consider a ring configuration with a radius R, that rotates over a rotational axis perpendicular to the plane of the ring with angular velocity Ω. The two optical counterpropagating beams experience two different optical paths, due to the rotation of the frame:

$$L^{\pm} = 2\pi R - R\Omega t^{\pm} = c^{\pm} t^{\pm} \tag{1.1}$$

with $t^{\pm}$ the time needed to cover the distance $L^{\pm}$ and $c^{\pm}$ the light speed of the two counterpropagating beams.

We can obtain:

$$\Delta t = t^{+} - t^{-} = 2\pi R \left[\frac{2R\Omega(c^{+} - c^{-})}{c^{+} c^{-}} \right] \tag{1.2}$$

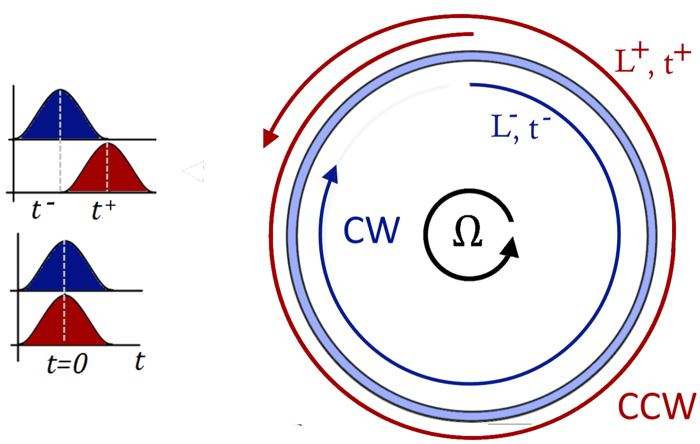

Figure 1.2: Counterpropagating beams in a ring structure, and revolution times.

Let's consider that the light is propagating into a medium with refractive index n and let's consider the relativistic composition of propagation speed and tangential speed of medium. The speeds c^{-} and c^{+} can be rewritten as [2]:

$$c^{-} = \frac{c/n + R\Omega}{1 + R\Omega/(nc^2)} = \frac{c}{n} + R\Omega \left(1 - \frac{1}{n^2}\right) + ..., \tag{1.3}$$

$$c^+ = \frac{c/n - R\Omega}{1 - R\Omega/(nc^2)} = \frac{c}{n} - R\Omega\left(1 - \frac{1}{n^2}\right) + ... \tag{1.4}$$

where c is the speed of light in vacuum and the right terms of the equations are the Taylor series expanded at the first term.

So using Eqs. 1.3 and 1.4 in Eq. 1.2, we obtain:

$$\Delta t = t^+ - t^- = 2\pi R\left[\frac{2R\Omega - 2R\Omega(1 - 1/n^2)}{c/n^2}\right] = \frac{4\pi R^2\Omega}{c^2}. \tag{1.5}$$

The relative phase can be found using the definition of the phase:

$$\Delta\Phi = \frac{2\pi c\Delta t}{\lambda} = \frac{8\pi A}{\lambda c}\Omega \tag{1.6}$$

with A the area of the ring resonator. It could be shown that the formula is valid also for non-circular closed paths. The last equation provides an easy way for setting up an angular velocity sensor. By reading the intereference signal between the two counterpropagating waves in a ring structure, we can obtain information about the angular velocity of the frame on a rotational axis orthogonal to the plane of the structure. When this kind of sensor is realized using optical fibres, it is called Interferometric Fibre Optic Gyroscope (IFOG).

If the ring structure is a closed loop, resonance conditions arise for both the counterpropagating modes. In particular, the resonance condition happens when the optical path ($n_{eff}^{\pm}L^{\pm}$, with $n_{eff}^{\pm}$ the effective index of the clockwise (CW) and counterclockwise (CCW) modes in the resonator) is an integer multiple of the wavelength:

$$\frac{n_{eff}^{\pm}L^{\pm}}{\lambda_R^{\pm}} = m. \tag{1.7}$$

with m an integer representing the order of resonance, equal to the order of resonance in the absence of rotation $m = nL/\lambda_R$ (with λ_R the resonance wavelength in the absence of rotation and L the absolute length of the resonator). The effective index of the counterpropagating modes, $n_{eff}^{\pm}$, can be calculated as the ratio between the speed of light in vacuum and the effective speed of light of the mode, $v^{\pm}$. Moreover, the effective speed of light of the counterpropagating waves is the ratio between the effective length and the time required to cover it ($v^{\pm} = L^{\pm}/t^{\pm}$), so:

$$\lambda_R^{\pm} = \frac{ct^{\pm}}{Ln}\lambda. \tag{1.8}$$

Thus, we have:

$$\Delta\lambda_R = \frac{c\Delta t}{Ln}\lambda = \frac{2R\Omega}{cn}\lambda. \tag{1.9}$$

The splitting between the angular resonances become:

$$\Delta\omega_R = \frac{4\pi R\Omega}{n\lambda}. \tag{1.10}$$

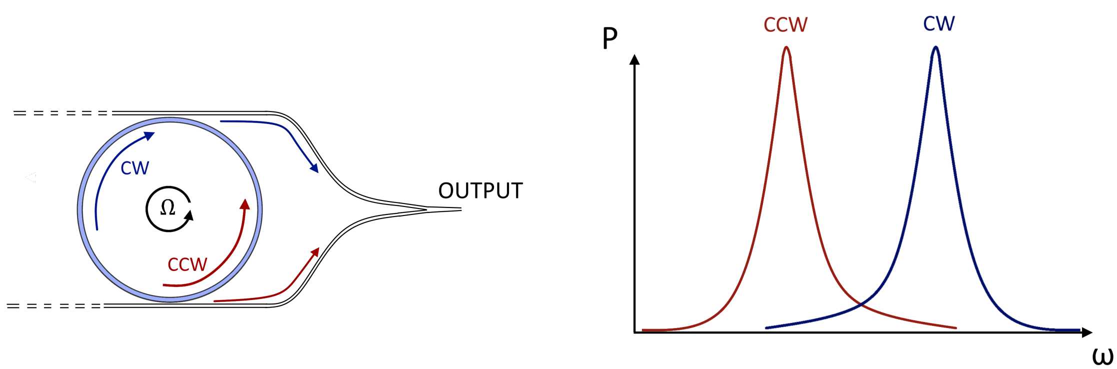

(a) (b)

Figure 1.3: Structure of a resonant ring Sagnac gyroscope (a). Resonance peaks of the CCW and CW waves during rotation. (b).

A sensor of angular velocity can be easily set up by reading the distance between the resonance frequencies of the CW and the CCW resonant modes. This is what is called Resonant Micro Optic Gyroscope (RMOG) [2]. The limitation of this kind of sensor is the sensitivity. In fact, in Equation 1.10, the splitting between the resonance angular frequencies is linearly dependent on the radius of the ring structure. That's the main reason why the integration of optical gyroscopes is still an open challenge in research. In fact, in the presence of the lock-in effect (acting as a noise source) a small resonance splitting could be impossible to be read. In order to let the miniaturization of these devices, other solutions should be investigated.

Lock-in effect

In the presence of undesired backscattering in the medium where the modes counterpropagate, the phase shift ψ between the counterpropagating optical signals can be modelled by the following differential equation [1]:

$$\frac{d\psi}{dt} = S\Omega + b\sin\psi \tag{1.11}$$

where S is a sensitivity term (related to geometrical parameters of the gyroscope and to the laser operating wavelength) and b is the backscattering coefficient which has units of frequency and takes into account all the back-reflections. If b is comparable with $S\Omega$, the differential equation exhibits a stationary solution and the frequency difference between the CW and the CCW signals vanishes [1]. So, the backscattering acts as a source of noise for the optical gyroscope and creates the so called "dead band", that is a region of angular velocities that cannot be detected. In order to reduce the lock-in effect, an external controlled constant bias is applied to let the gyroscope operate in the unlocked region (for example a constant physical known rotation to the gyroscope).

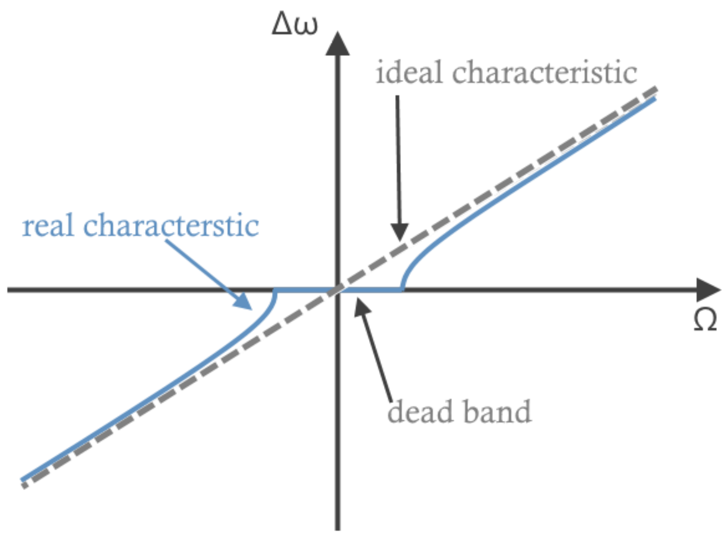

Figure 1.4: Lock-in effect.

1.0.2 Parity-time symmetry

In this thesis, the idea of parity-time (PT) symmetry for enhancing the sensitivity of classical Sagnac optical gyroscopes is investigated. Since Bender et al. discovered that non-Hermitian Hamiltonians with PT symmetry can exhibit entirely real spectra [71, 72] , lots of studies about PT symmetry have been carried on also in optics [73], such as in whispering-gallery modes [74], nanobeam cavities [75], coupled optical waveguides [76, 77], photonic lattices [78], plasmonics [79], and pumped lasers at the exceptional point [80]. In fact, several physical processes are known in optics to obey equations formally equivalent to that of Schrödinger in quantum mechanics (e.g. spatial diffraction and temporal dispersion) [73]. In order to satisfy the PT symmetry condition, the Hamiltonian describing the system must commute with the PT operator ($[PT, \hat{H}] = 0$) [71], where P is the parity operator and T is the time reversal operator:

$$P : \begin{pmatrix} x \\ y \\ z \end{pmatrix} \rightarrow \begin{pmatrix} -x \\ -y \\ -z \end{pmatrix} \tag{1.12}$$

$$T : t \rightarrow -t \tag{1.13}$$

The parity-time symmetry is verified when the complex potential (V) of the system is subject to the symmetry constraint $V(x, y, z) = V^*(-x, -y, -z)$ [75], where the complex conjugation derives from the time reversal transformation as shown in [81]. In the optical diffraction equation, the complex refractive index distribution plays the role of an optical potential [73]. So, an optical PT-symmetric system could be realized by modulating the real part of the refractive index to be an even function and the imaginary part to be an odd function. One of the most interesting things about PT-symmetric systems is the existence of a particular condition, called exceptional point (EP), above which the spectrum ceases to be real and starts to show imaginary eigenvalues. This means the onset of a spontaneous PT symmetry-breaking, that is a "phase transition" from the exact to the broken PT phase. This is the ideal condition for the enhancement of the sensitivity of angular velocity sensors. The idea of the next section is to combine the enhancement of the sensitivity provided by exceptional points of parity-time-symmetric system with the Sagnac effect.

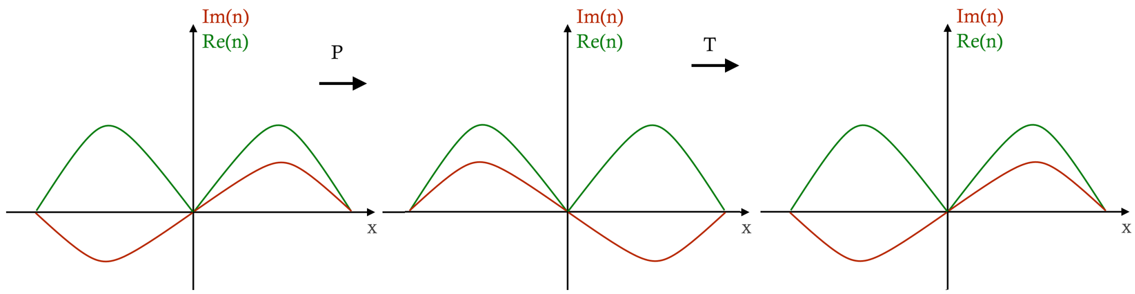

Figure 1.5: Real part and imaginary part of refractive index in parity-time-symmetric systems.

1.1 Parity-Time-symmetric gyroscope

1.1.1 Theoretical background

The resonance conditions in a non-rotating optical ring are the same for clockwise (CW) and counter-clockwise (CCW) propagating modes, whereas, in the presence of an angular speed (Ω), the resonance angular frequencies associated to CW and CCW modes are separated by:

$$\Delta\omega = \frac{8\pi A\Omega}{n_{eff} L\lambda} = 2\Delta\omega_s \tag{1.14}$$

where A and L are the enclosed area and the ring perimeter, respectively, λ is the wavelength of light in vacuum and n_{eff} the effective index in the ring resonator. The idea proposed in [11] uses two coupled rings to avoid the lock-in effect, as in Figure 1.6.

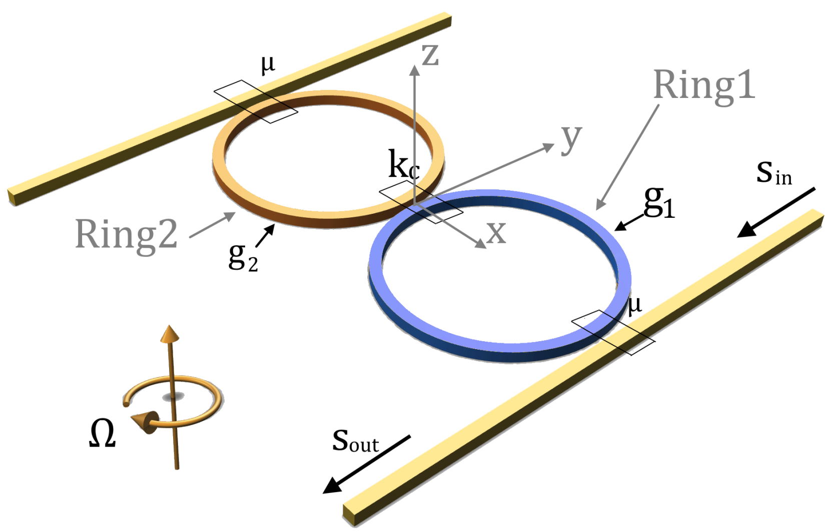

Figure 1.6: Schematic of a PT-symmetric gyroscope system [12].

In a non-rotating frame, if the system is excited as in Figure 1.6, the interplay between the electric modal fields in the two identical rings can be described through the following coupled differential equations [82]:

$$\frac{d}{dt}a_1 = j\omega_0 a_1 + g_1 v_g a_1 - jk_c a_2 - j\mu s_{in} \tag{1.15}$$

$$\frac{d}{dt}a_2 = j\omega_0 a_2 + g_2 v_g a_2 - jk_c a_1 \tag{1.16}$$

where $a_{1/2}$ represents the energy amplitude in the first/second cavity, normalized so that $|a_{1/2}|2$ is the total energy stored in the first/second ring. The term s_{in} is the amplitude of the wave travelling in the input bus, normalized such that $|s_{in}|^2$ represents the total power flowing through any cross-section; ω_0 is the resonance angular frequency for each uncoupled ring resonator, v_g is the light group velocity in a medium, μ is the mutual coupling coefficient between the ring and the external bus, k_c is coupling strength between the rings. The coefficient $g_{1/2}$ (expressed in m^{-1}) represents the amplitude gain (or loss if negative) of the first/second ring. According to Eqs. 1.15 and 1.16 the term $g_{1/2}v_g$ represents the gain rate and is measured in s^{-1}. In this context the $g_{1/2}$ coefficient can be expressed as:

$$g_{1/2} = -\frac{1}{v_g}\left(\frac{1}{\tau_k} + \frac{1}{\tau_e} + \frac{1}{\tau_s}\right) + g_{r1/2} = -\alpha_k - \alpha_e - \alpha_s + g_{r1/2} \tag{1.17}$$

where $1/\tau_k$ is the photon decay rate (expressed in s-1) due to the coupling between rings ($\tau_k = 2v_g/(2\pi R k_c^2)$); $1/\tau_e$ is the photon decay rate due to the coupling between the rings and the external buses ($\tau_e = 2/\mu^2$); $1/\tau_s$ is the photon decay rate related to the sidewall roughness scattering loss; $g_{r1/2}$ is the net modal gain (or loss, if negative) of the first/second ring. In order to make the system PT-symmetric, it is necessary that parity (P) and time (T) symmetries of the potential of the Hamiltonian of the system are simultaneously verified [83]. By defining the domains Ring1 and Ring2 as in Figure 1.6 and

$$g(x,y,z) = \begin{cases} g_1 & \forall (x,y,z) \in \ Ring\,1 \\ g_2 & \forall (x,y,z) \in \ Ring\,2 \\ 0 & elsewhere \end{cases}, \tag{1.18}$$

the term $\omega_0 + jgv_g$ plays the role of the potential of the Hamiltonian. So, the system becomes PT-symmetric only when

$$g(x,y,z) = -g(-x,-y,-z). \tag{1.19}$$

It implies that g_1=-g_2. Since the system is linear and time-invariant, with ω the angular frequency of the laser emission, the following stationary condition is verified:

$$\frac{d}{dt}a_{1,2} = j\omega a_{1,2}. \tag{1.20}$$

Substituting 1.20 in 1.15 and 1.16, and solving them for a_1, we find:

$$\frac{a_1}{s_{in}} = -\frac{j\mu\left(j\omega - j\omega_0 - g_2 v_g\right)}{\left(g_1 g_2 v_g^2 - \left(\omega-\omega_0\right)^2 - jv_g\left(g_1+g_2\right)\left(\omega-\omega_0\right) + k_c^2\right)} \tag{1.21}$$

with eigenfrequencies:

$$\omega_{PT_{1,2}} = \omega_0 - \frac{jv_g\left(g_1+g_2\right)}{2} \pm \sqrt{(k_c^2) - \left(\frac{g_1 v_g - g_2 v_g}{2}\right)^2}. \tag{1.22}$$

It is important to observe that these resonance angular frequencies are generally complex. If the system is PT-symmetric (g_1=-g_2), the resonance frequencies become real if $k_c^2 > v_g^2(g_1 - g_2)2/4$, and the splitting of resonances is visible in the spectral response of the transfer function S_{out}/S_{in} (being $S_{out,in} = |s_{out,in}|^2$). The condition $2k_c = v_g|g_1 - g_2|$ represents the exceptional point where the two resonance frequencies coalesce and only one peak is visible in the spectral response. If the system is rotating, with reference to an inertial frame, 1.15 and 1.16 can be rewritten as:

$$\frac{d}{dt}a_1 = j\omega_0 a_1 + {g_1}^* v_g a_1 - jk_c a_2 - j\mu s_{in} \tag{1.23}$$

$$\frac{d}{dt}a_2 = j\omega_0 a_2 + {g_2}^* v_g a_2 - jk_c a_1. \tag{1.24}$$

where $g_1^* = g_1 - j\Delta\omega_s/v_g$ and $g_2^* = g_2 + j\Delta\omega_s/v_g$. Solving for a_1, we obtain that the new eigenfrequencies are (for a PT-symmetric system designed at the exceptional point $2k_c = v_g|g_1 - g_2|$):

$$\begin{aligned} &\omega_{PT1,2} = \omega_0 \pm \sqrt{(k_c^2) - \left(\tfrac{g_1 v_g - g_2 v_g - 2j\Delta\omega_S}{2}\right)^2} \cong \\ &\cong \omega_0 \pm (1+j)\sqrt{\Delta\omega_S k_c}. \end{aligned} \tag{1.25}$$

It should be observed that, when the gyroscope system rotates, the resonance frequencies become complex even at the exceptional point $2k_c = v_g|g_1 - g_2|$. The eigenfrequencies in Eq. 1.25 correspond to those obtained in [11], particularized for a PT-symmetric system ($g_1 = -g_2$). Indeed, according to [74], the PT-symmetry condition requires an average gain equal to zero ($(g_1 + g_2)/2 = 0$). The transfer function $|s_{out}|^2/|s_{in}|^2$ could be obtained through the following relation:

$$s_{out} = s_{in} - j\mu a_1. \tag{1.26}$$

A second order system with two complex eigenfrequencies, symmetrically placed with respect to a central real frequency ($\omega_{R,1,2} = \omega_0 \pm (\omega_D + j\omega_D))$), has only one peak, and a FWHM equal to $2\sqrt{2\omega_D}$. So, we obtain a FWHM equal to:

$$\Delta\omega_{FWHM} = 2\sqrt{2\left|\Delta\omega_S\right| k_c}. \tag{1.27}$$

Figure 1.7a shows the relation between the coupling strength and the full width at half maximum, at different radius sizes. So, the theoretical full width at half maximum is:

$$\Delta\omega_{FWHM} = 4\sqrt{2\frac{\pi A\Omega}{L\lambda_0}k_c}. \tag{1.28}$$

It is also possible to demonstrate that the peak of the transfer function is proportional to Ω^{-2}.

$$\left.\frac{S_{out}}{S_{in}}\right|_{peak} \propto \frac{\lambda_0}{R^2\Omega^2 k_c^2}. \tag{1.29}$$

Under rotative condition, the spectral output of the gyroscope appears like that shown in Figure 1.7b. It is easy to show that, differently from what is stated in [11], splitting does not occur. The spectral response appears to have a larger linewidth with respect to the system at rest, as expected. It should be also observed that, in order to identify the direction of rotation of the gyroscope, the system cannot be PT-symmetric at rest.

In Figure 1.8 the spectrum of the power exiting the gyroscope is shown at different operating conditions. The first line shows the eigenfrequencies of the system in the complex plane and the simulated output spectrum in PT-symmetric condition, at the exceptional point in a non-rotative frame. In the second and third lines, the cases of a PT-symmetric system at rest, not at the exceptional point, are shown.

The fourth line represents the case of a rotating PT-symmetric system placed at the exceptional point. The last line represents the case of a system that is outside the PT-symmetric condition even at rest.

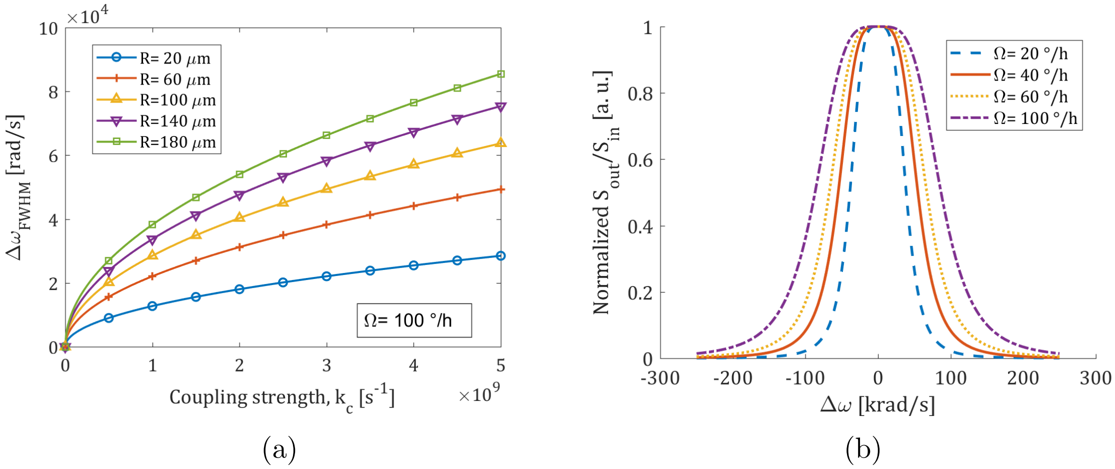

Figure 1.7: Coupling strength as a function of the full width at half maximum, at different radius sizes [12] (a). Normalized transfer function S_{out}/S_{in} at different angular velocities, with g_1=-g_2=5 cm^{-1}, μ=2.17·10^5 s$^{-1/2}$ [12] (b).

1.1.2 Numerical results

Waveguide cross-section

In this section a practical configuration is proposed to realize the gyroscope. The theoretical approach shown in the previous paragraph is completely general. In order to perform our simulations, we chose to use the SiGeSn heterostructures. Even though silicon and Germanium indirect bandgaps represent a drawback for optoelectronic devices, SiGeSn heterostructures have been demonstrated to be suitable for advancing monolithic integration of photonic active devices. Indeed, they enable a complete suite of active on-chip photonic components, guaranteeing good flexibility in realizing heterostructures working in the mid infrared and far infrared, and being compatible with CMOS platform, that represents the most popular technology in the electronic chip design industry [84][85].

Operating condition	Complex eigenfrequencies	Output spectrum
$g_1 = -g_2$ $4k_c^2 = v_g^2 (g_1 - g_2)^2$ $\Omega = 0°/h$	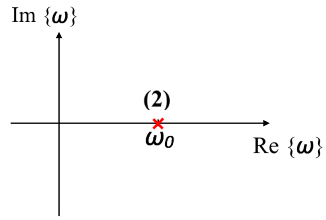	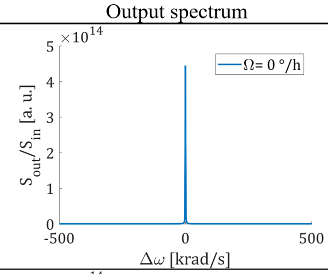
$g_1 = -g_2$ $4k_c^2 > v_g^2 (g_1 - g_2)^2$ $\Omega = 0°/h$	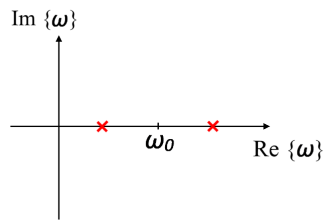	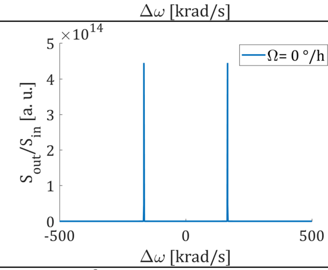
$g_1 = -g_2$ $4k_c^2 < v_g^2 (g_1 - g_2)^2$ $\Omega = 0°/h$	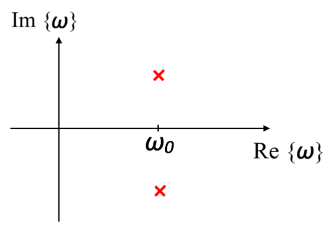	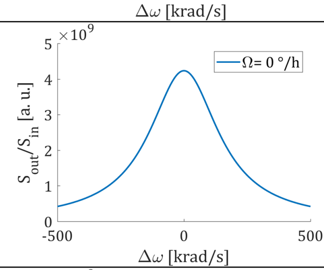
$g_1 = -g_2$ $4k_c^2 = v_g^2 (g_1 - g_2)^2$ $\Omega > 0°/h$	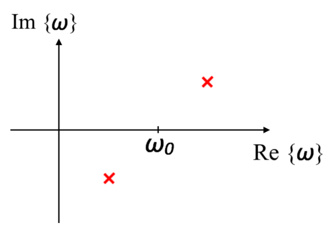	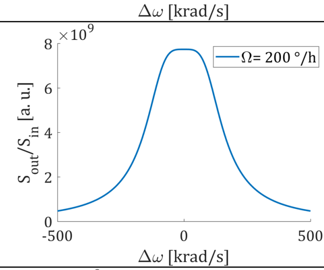
$g_1 > 0\ m^{-1}$ $g_2 < 0\ m^{-1}$ $g_1 > -g_2$ $4k_c^2 = v_g^2 (g_1 - g_2)^2$ $\Omega > 0°/h$	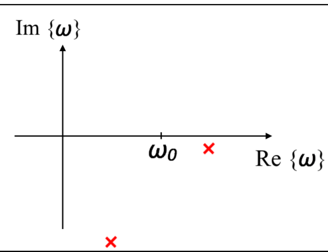	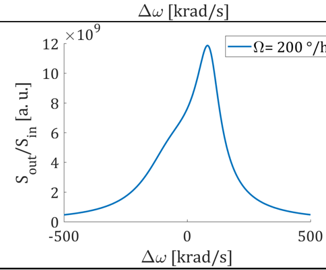

Figure 1.8: Operating conditions (first column); eigenfrequencies in the complex plane (second column); transfer function of the power exiting the gyroscope (third column). All the simulations have been performed with g_1=-g_2=5 cm^{-1}, μ=2.17·10^5 s$^{-1/2}$ [12].

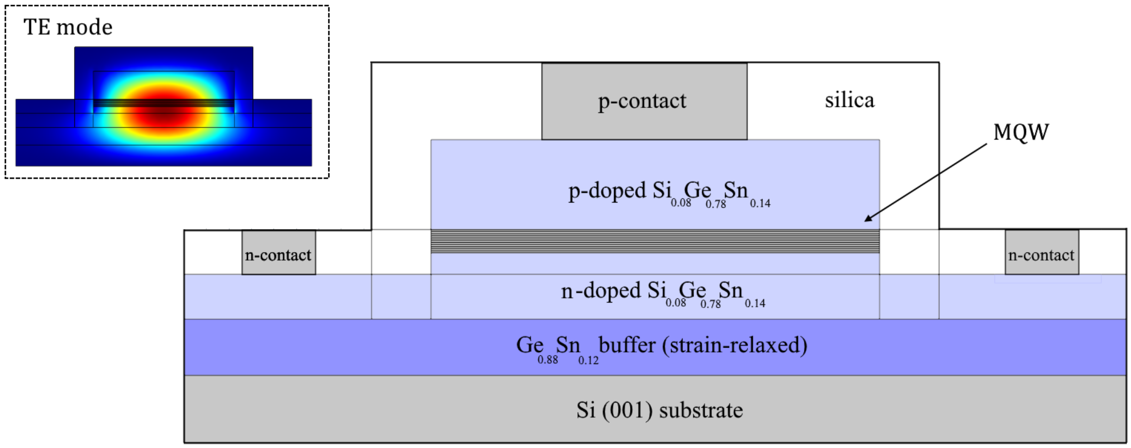

Figure 1.9: Waveguide cross-section: structure design. Inset: TE optical field [12].

The external laser wavelength is chosen to be 3 µm. The gain region has been realized through a strain-balanced Ge_zSn_{1-z}-$Si_xGe_ySn_{1-x-y}$ multiple-quantum-well (MQW) amplifier, using the structure proposed in [86]. In particular, the structure in Figure 1.9 shows the cross section of the waveguide composing the active ring resonator. The same structure could be also used to achieve the needed loss. In fact, tuning the current density in the multiple-quantum-well structure it is possible to modulate the loss, up to the needed value. The structure is a ridge waveguide. A fully strain-relaxed $Ge_{0.88}Sn_{0.12}$ buffer layer is grown on a 001-oriented Si substrate. Then an n-type $Si_{0.08}Ge_{0.78}Sn_{0.14}$ layer is grown as the bottom contact. Five pairs of $Ge_{0.84}Sn_{0.16}/Si_{0.09}Ge_{0.8}Sn_{0.11}$ quantum-wells (five $Ge_{0.84}Sn_{0.16}$ wells and six $Si_{0.09}Ge_{0.8}Sn_{0.11}$ barriers) are then grown. Finally, a p-type $Si_{0.08}Ge_{0.78}Sn_{0.14}$ layer is grown at the top. A silica cover is used to provide a high contrast in the refractive indices and, consequently, a major optical confinement in the ridge. The width of the ridge is 2 µm, whereas the thickness is 0.6 µm. The well width is set to 10 nm, whereas the barrier width is set to 9 nm, as proposed in [86]. The doping concentration is 10^{19} cm^{-3} for the p-doped regions and $5{\cdot}10^{18}$ cm^{-3} for the n-doped region.

Gyro design and performance

According to the results in [86], it is possible to reach a material amplitude gain (g_m) with values ranging from -375 cm^{-1} (loss) to 550 cm^{-1} (gain), when the total injected surface carrier densities varies from 10^{12} cm^{-2} to 6 $\cdot 10^{12}$ cm^{-2}. This means that it is possible to control the loss/gain of the quantum-well region by applying different values of voltage to the PIN structure. The absorption amplitude loss in the n-doped layer has been considered equal to 16.44 cm^{-1} [86], and then, a n-modal loss (α_n) of 6.65 cm^{-1} has been estimated (being the confinement factor in the n-doped layer equal to 40.48 %, according to our simulations). The absorption amplitude loss in the p-doped layer has been considered equal to 92.88 cm^{-1} [86], and then, a p-modal loss (α_p) of 23.15 cm^{-1} has been estimated (being the confinement factor in the p-doped layer equal to 24.93 %, according to our simulations). The net modal gain ($g_{r1,2}$) of the structure depends on the confinement factors in the wells (Γ_w= 6.54 %) and in the p-doped and n-doped regions, according to the following relation:

$$g_{r1,2} = \Gamma_{\mathrm{w}} g_m - \alpha_p - \alpha_n. \tag{1.30}$$

This means that the net modal gain ranges from -54.33 cm^{-1} to 6.16 cm^{-1}, when the total injected surface carrier density varies from 10^{12} cm^{-2} to 6 $\cdot 10^{12}$ cm^{-2}. Then, the coupling strength (k_c) between the rings has been evaluated by adopting the method shown in [87], covering all the structure with the same silicon oxide layer in the proximity of the coupling region. The dimensionless power coupling factor K_{rr} between the two rings has been calculated as shown in [87] and then k_c has been evaluated as [82]

$$k_c = \frac{K_{rr} v_g}{2\pi R}. \tag{1.31}$$

The value of k_c results to be dependent on the distance g_0 (gap between the edges of the ridges of the rings), whereas it is nearly invariant with radius, because of a quasi-punctual coupling. It is possible to obtain values of k_c from 1.6 $\cdot 10^9$ s^{-1} to 0.9 $\cdot 10^9$ s^{-1}, for a gap g_0 ranging from 50 nm to 150 nm. A gap of 80 nm has been chosen for our design, which corresponds to a coupling strength of 1.4 $\cdot 10^9$ s^{-1}. A full width at half maximum of 3.37$\cdot 10^4$ rad/s for a Ω =100 °/h can be reached using this structure, being the radius of the rings equal to 100 µm.

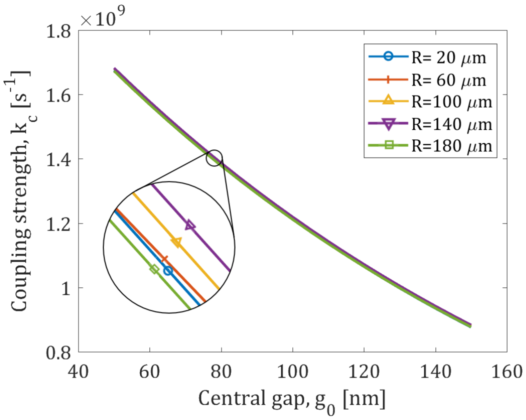

(a)

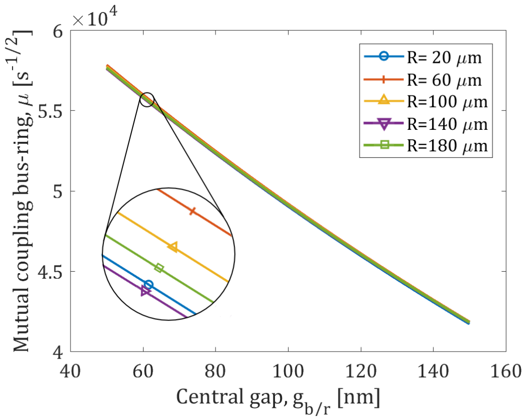

(b)

Figure 1.10: Coupling strength as a function of gap g_0 [12] (a). Mutual coupling μ as a function of gap $g_{b/r}$ [12] (b).

The mutual coupling between the ring and the bus (μ) has been evaluated in the same way as for k_c (Figure 1.10b). In particular the dimensionless power coupling factor K_{rb} between rings and buses has been calculated with the same procedure shown in [87] and then μ has been evaluated as [82]:

$$\mu = \sqrt{\frac{K_{rb} v_g}{2\pi R}}. \tag{1.32}$$

The value of the mutual coupling depends on the distance $g_{b/r}$, whereas it is nearly invariant with radius. A distance $g_{b/r}$ between the edges of the ridges of the rings and the buses of 100 nm has been chosen, which corresponds to a mutual coupling of $4.91 \cdot 10^4$ s$^{-1/2}$ (having a radius of 100 μm). Our investigations show that g_1 and g_2 can be tuned from 0 cm^{-1} to 4.78 cm^{-1} and from -55.71 cm^{-1} to 0 cm^{-1}, respectively, within the considered range of injected carriers. Then, assuming k_c=1.4·109 s^{-1}, the exceptional point condition, $2k_c = v_g|g_1 - g_2|$, and the PT-symmetry condition, $g_1 = -g_2$, can be achieved with g_1=-g_2=0.189 cm^{-1}, included within the above-mentioned ranges. Figure 1.11 shows the operating characteristics of the designed sensor on a log-log graph and it is compared with the Sagnac spectral shift of a single ring resonator with the same radius of one of the ring of the PT-symmetric gyroscope. Differently from [11], in which one ring is shown to act as a laser, in our approach the active ring acts as a travelling-wave amplifier. So, the direction of optical beams is forced by the input signal. This approach drastically reduces the negative effects of backscattering. In fact, typical values for backscattering decay rate are one order of magnitude lower than the chosen value of k_c.

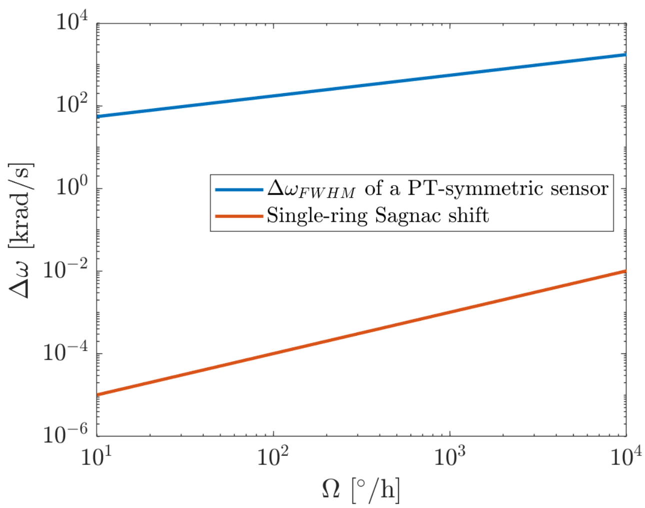

Figure 1.11: Full width at half maximum of the designed PT-symmetric gyroscope as a function of the angular velocity (on a log-log graph) compared with the classical Sagnac spectral shift on a gyroscope with a single ring with the same radius.

1.1.3 Considerations about parity-time-symmetric gyroscope

It has been shown an optical gyroscope in the proximity of the exceptional point of a PT-symmetric optical system has sensitivity several orders of magnitude higher than the classical Sagnac gyroscope. Since the sensitivity is proportional to the square root of the angular velocity rather than to the angular velocity (as it happens in classical Sagnac gyroscopes), the sensitivity enhancement is only present at low angular velocities (corresponding to a Sagnac splitting lower than the value of the coupling strength). For integrated devices the coupling strength can be of the order of 10^{10} rad/s - 10^{11} rad/s, so, for reasonable values of angular velocities, the sensitivity enhancement is still present. However, the stability of the system has not been verified up to now. In the next section, the concept of anti-parity-time will be investigated and a new optical anti-parity-time-symmetric gyroscope will be shown.

1.2 Anti-PT-symmetric gyroscope

1.2.1 Anti-PT symmetry vs PT symmetry

As said, a system is considered to be PT-symmetric provided that its Hamiltonian $\hat{H}$ commutes with the time reversal operator (T) and the parity operator (P) ($[PT, \hat{H}] = 0$). Whereas, in an anti-PT-symmetric system, the Hamiltonian satisfies the anti-commutation relation $\{PT, \hat{H}\} = 0$ [88] [89]. Anti-PT symmetry is a special case of charge-conjugation symmetry [90] [91].

In optics, PT-symmetric systems are usually realized through an active cavity and a passive cavity, with the same resonant frequency, and with perfectly balanced gain and loss. Anti-PT-symmetric systems have been investigated less than the parity-time-symmetric ones in literature. However, for some kinds of sensing, they are better suitable than the PT-symmetric ones.

Eqs. 1.33 and 1.34 describe the energy exchanges between two generic coupled resonant cavities:

$$j\frac{da_1}{dt} = -\omega_1 a_1 + j\gamma_1 a_1 + k_1 a_2, \tag{1.33}$$

$$j\frac{da_2}{dt} = -\omega_2 a_2 + j\gamma_2 a_2 + k_2 a_1 \tag{1.34}$$

where $a_{1/2}$ represents the energy amplitude in the first/second cavity, normalized so that $|a_{1/2}|^2$ is the total energy stored in the first/second cavity; $\omega_{1/2}$ is the resonance angular frequency of the first/second isolated cavity; $\gamma_{1/2}$ is the gain in the first/second cavity; $k_{1,2}$ is related to the mutual energy coupling between the two cavities.

For $\omega_1 = \omega_2$, $\gamma_1 = -\gamma_2$ and $k_1 = k_2^*$, the system is parity-time-symmetric. Relaxing the condition on the gains (with $|\gamma_1| \neq |\gamma_2|$), the system is said to be quasi-PT-symmetric.

In order to be anti-PT-symmetric, a system should have $\gamma_1 = \gamma_2$, $\omega_1 = -\omega_2$ and $k_1 = -k_2^*$. Relaxing the condition on ω_1 and ω_2 (with $|\omega_1| \neq |\omega_2|$), the system can be called “quasi-anti-PT-symmetric” (in analogy with the quasi-PT-symmetric one). Practically, negative frequencies don’t make sense. So, from now on we will say anti-PT-symmetric to indicate a quasi-anti-PT-symmetric system.

It should be noted that, considering reciprocal systems ($k_1 = k_2$), k_1 and k_2 are real in PT-symmetric systems, whereas k_1 and k_2 are imaginary in anti-PT-symmetric systems.

Table 1.1 summarizes the concept of PT- and anti-PT-symmetric resonant systems. We would like to underline that PT-symmetric and anti-PT-symmetric systems can be designed also with non-resonant systems [92].

Table 1.1: PT symmetry and anti-PT symmetry summary in resonant systems. Different colors of rings correspond to different gains.

Gain/loss	**Resonances**	**Coupling**	**Symmetry**
$\gamma_1 = -\gamma_2$	$\omega_1 = \omega_2$	$k_1 = k_2^*$	PT 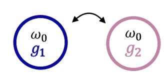
$\lvert\gamma_1\rvert \neq \lvert\gamma_2\rvert$	$\omega_1 = \omega_2$	$k_1 = k_2^*$	quasi-PT 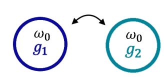
$\gamma_1 = \gamma_2$	$\omega_1 = -\omega_2$	$k_1 = -k_2^*$	anti-PT ?
$\gamma_1 = \gamma_2$	$\lvert\omega_1\rvert \neq \lvert\omega_2\rvert$	$k_1 = -k_2^*$	quasi-anti-PT 

1.3 Anti-PT-symmetric gyroscope

As seen in the previous sections, resonant angular frequencies related to an optical beam propagating in a single ring resonator, that is rotating with an angular velocity Ω changes of a quantity $\Delta\omega_s$, with respect to a rest condition, that could be evaluated as:

$$\Delta\omega_s = \pm\frac{4\pi A\Omega}{Ln_{eff}\lambda}, \tag{1.35}$$

where λ is the wavelength in vacuum, n_{eff} is the effective index in the ring resonator, A and L are the area and the perimeter of the surface enclosed by the resonator, respectively. The sign minus (plus) is chosen if the mechanical rotation is in the same (the opposite) direction of the rotation of the optical beam in a cavity.

The optical gyroscope that we propose is shown in Fig. 1.12.

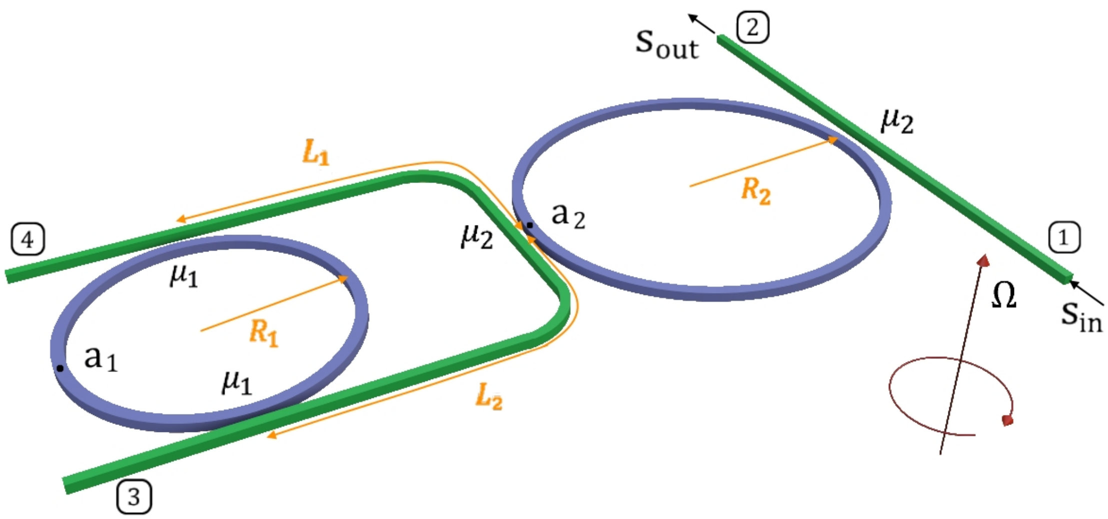

Figure 1.12: Example of the structure of an anti-PT-symmetric gyroscope [13].

The equations describing the anti-PT-symmetric system are:

$$\frac{da_1}{dt} = j\omega_1 a_1 + g a_1 - j\mu_2(-j\mu_1)e^{-j\phi_1}a_2, \tag{1.36}$$

$$\frac{da_2}{dt} = j\omega_2 a_2 + g a_2 - j\mu_1(-j\mu_2)e^{-j\phi_2}a_1 - j\mu_2 s_{in}, \tag{1.37}$$

where g is the total gain in each ring, μ_i is the real mutual coupling between the buses and the i-th ring, s_{in} is the input field amplitude, normalized so that $|s_{in}|^2$ represents the input power. The terms ϕ_1 and ϕ_2 are the phase shifts between the points where a_1 and a_2 are evaluated:

$$\phi_{1,2} = \frac{2\pi}{\lambda}n_{eff}L_{1,2} + \frac{2\pi}{\lambda}n_{eff}\frac{\pi R_1}{2}, \tag{1.38}$$

with n_{eff} the group index, R_1 the radius of the first ring and L_1 and L_2 the geometrical lengths in Fig. 1.12.

Eqs. 1.36 and 1.37 can be easily rewritten in the form of Eqs. 1.33 and 1.34, with $k_{1,2} = -j\mu_1\mu_2 e^{-j\phi_{1,2}}$. So, the system will be anti-PT-symmetric, provided that $e^{-j\phi_1} = e^{j\phi_2}$. A possible solution is given by $\phi = \phi_1 = \phi_2 = m\pi$ (with $m \in \mathbb{N}$), around $\omega_0 = (\omega_1 + \omega_2)/2$. We choose L_1 and L_2 to satisfy that solution. It should be noted that two indirectly coupled ring resonators have been used to achieve an imaginary coupling. The concept of imaginary coupling has been already shown in [93, 94, 95].

Finally, we will choose the same gain γ in both the rings, so:

$$\gamma = \gamma_{1,ext} - 2\mu_1^2 - \alpha_1 = \gamma_{2,ext} - 2\mu_2^2 - \alpha_2, \tag{1.39}$$

where $\gamma_{1,ext}$ and $\gamma_{2,ext}$ are the external gains in first and second rings, respectively, and α_1 and α_2 represent the intrinsic losses in each ring resonator. It should be noted that $\gamma_{1,ext}$ and $\gamma_{2,ext}$ will be chosen to keep the total gain (g) negative. In this way the system doesn't start to oscillate. This solution will be useful to recognize the sign of the angular velocity.

Defining $k_c = -j\mu_1\mu_2$, Eqs. 1.36 and 1.37 can be rewritten as:

$$\frac{da_1}{dt} = j\omega_1 a_1 + g a_1 - jk_c e^{-j\phi} a_2, \tag{1.40}$$

$$\frac{da_2}{dt} = j\omega_2 a_2 + g a_2 - jk_c e^{-j\phi} a_1 - j\mu_2 s_{in}. \tag{1.41}$$

The resonant frequencies of the anti-PT-symmetric system are easily found, by forcing $s_{in} = 0$ in the periodic regime:

$$\omega_{aPT_{1,2}} = \frac{\omega_1 + \omega_2}{2} - jg \pm \sqrt{\left(\frac{\omega_1 - \omega_2}{2}\right)^2 + k_c^2}. \tag{1.42}$$

The exceptional point is reached when the argument of the square root vanishes:

$$|\omega_1 - \omega_2| = 2jk_c. \tag{1.43}$$

Let's now consider the same system in a frame rotating with an angular velocity Ω. The resonant frequency of each isolated ring changes according to Eq. 1.35.

If the system is designed to be at the exceptional point when it is at rest, the rotation forces the system to depart from the exceptional point and the eigenfrequencies become:

$$\omega_{EP_{1,2}} = \frac{\omega_1 + \omega_2}{2} - jg \pm \sqrt{\mu_1 \mu_2 \Delta\omega_\Omega}, \tag{1.44}$$

where

$$\Delta\omega_\Omega = \frac{4\pi\Omega}{\lambda n_{eff}} \frac{R_1 + R_2}{2}. \tag{1.45}$$

Recalling from [82] that $\mu_{1,2}^2$ is proportional to the fraction of the power coupled from the bus to the ring ($\kappa_{1,2}^2$) and to the inverse of the radius of the ring ($\mu_{1,2}^2 = \kappa_{1,2}^2 \frac{v_g}{2\pi R_{1,2}}$), if the system is designed to have $\kappa_1 = \kappa_2 = \kappa$ and $R_1 \approx R_2$, we can rewrite the spectral splitting as:

$$\Delta\omega_{EP} \approx \sqrt{\frac{2\kappa^2 v_g}{\lambda n_{eff}} \Omega}. \tag{1.46}$$

The important result is that the splitting can be approximated to be independent from the dimension of the device. It means that the intrinsic limitation of the classical Sagnac effect (due to dependence of the Sagnac splitting on the R^{-1}) is overcome. It should be observed that the frequency splitting is real, differently from the complex splitting in the PT-symmetric gyroscope ($\Delta\omega_{PT,EP} = (1 + j)\sqrt{k_c \Delta\omega_S}$, with $\Delta\omega_S$ the Sagnac shift in a single ring), causing different measurable output spectra (Fig. 1.13).

The reader could object that κ and the radii R_1 and R_2 are linked by Eq. 1.43. However, it should be noted that once κ is fixed for a required sensitivity, the radii are not uniquely determined. Starting from Eq. 1.43 it could be demonstrated that:

$$\frac{|m_1 R_2 - m_2 R_1|}{\sqrt{R_1 R_2}} = \frac{\kappa^2}{\pi}, \tag{1.47}$$

with m_1 and m_2 the orders of resonance in each ring resonator. Solving 1.47, it is easy to prove that, for $m_1 = m_2$, R_1 and R_2 can be always chosen so that the approximation in Eq. 1.69 is still valid, even for $\kappa = 1$.

Fig. 1.13 gives a graphical representation of the resonance splitting in the proximity of the exceptional point of an anti-PT-symmetric gyroscope with $R_1 = 20\mu$m,

$R_2 = 19.95$ μm and $\gamma_1 = \gamma_2 = -0.5$ Mrad/s. The rotation-induced frequency splitting is equivalent to moving from the exceptional point to the so called "broken phase", unlike the PT-symmetric gyroscope, which, under rotation, exits even from the condition of the PT symmetry. Fig. 1.14 shows the enhancement of the splitting of an anti-PT-symmetric gyroscope at the exceptional point with respect to a classical Sagnac splitting. It is possible to appreciate a sensitivity enhancement of 6 orders of magnitude thanks to the exploitation of the exceptional point.

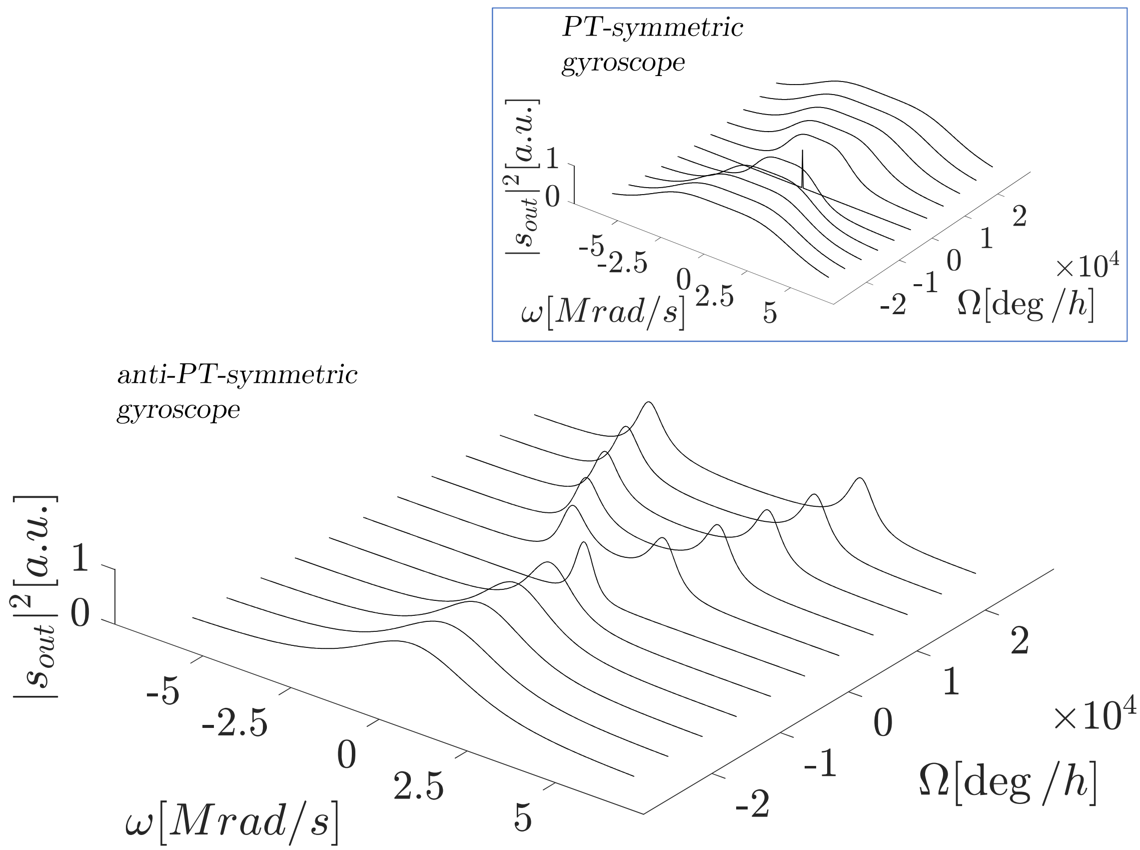

Figure 1.13: Normalized output spectrum in the proximity of the exceptional point of an anti-PT-symmetric gyroscope (with $R_1 = 20$ μm, $R_2 = 19.95$ μm and $\gamma_1 = \gamma_2 = -0.5$ Mrad/s) around $\lambda = 1.55$ μm. The inset shows the output spectrum of a PT-symmetric gyroscope (with $R_1 = 20\mu$m, $R_2 = 20$ μm and $\gamma_1 = -\gamma_2 = 1$ Trad/s) [13].

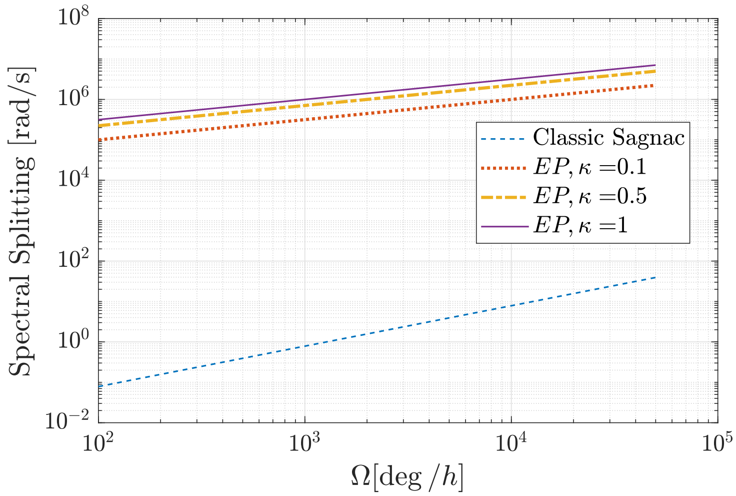

Figure 1.14: Comparison between the spectral splitting at the exceptional point of an anti-PT-symmetric gyroscope (with $R_1 = 20$ μm and $R_2 = 19.95$ μm) and the splitting due to the classical Sagnac effect in a single ring with radius $(R_1 + R_2)/2$, around $\lambda = 1.55$ μm [13].

1.3.1 Detectivity of an anti-PT-symmetric gyroscope

A problem in realizing this structure is represented by the accuracy in approaching the exceptional point and the enhanced noise at the exceptional point [96, 97]. If at rest condition the system is not at the exceptional point, Eq. 1.66 holds until:

$$\delta_{EP} = \left| \left(\frac{\omega_1 - \omega_2}{2} \right)^2 + k_c^2 \right| << \left| \mu_1 \mu_2 \Delta\omega_\Omega \right| . \tag{1.48}$$

The minimum detectable angular velocity should satisfy condition in Eq. 1.48. So, we can give an estimation of the minimum detectable angular velocity by considering the right term of Eq. 1.48 ten times greater than δ_{EP}:

$$\Omega_{min} \approx 10\pi n_g n_{eff} \frac{\delta_{EP}}{\kappa^2 \omega_0}. \tag{1.49}$$

So, a fine tuning method would be required either on the k_c or on the isolated resonant frequencies, in order to keep the system near the exceptional point. A feedback loop to control the phase over each of the resonator would be necessary to constantly keep the system around the exceptional point. The relative error over the isolated resonant frequencies could be much less than the relative error over the gains, that is necessary in PT-symmetric gyroscope to keep the system at the exceptional point. Moreover, the anti-PT-symmetric gyroscope requires only the exceptional point condition to be verified, whereas, in the PT-symmetric solution, the condition $\gamma_1 = -\gamma_2$ is also critical.

1.3.2 Readout

The presence of two distinct resonances in the measurable output power spectrum makes the readout process simpler than in the PT-symmetric gyroscope. In particular, a photodiode connected at the port 2 and followed by an oscilloscope would be sufficient as a readout system. The low-pass-filtered electronic signal at the oscilloscope, would have a resonance peak at the angular frequency $\omega_{EP,1} - \omega_{EP,2}$:

$$[sin(\omega_{EP,1}t) + sin(\omega_{EP,2}t)]^2 \xrightarrow{\text{LPF}} cos[(\omega_{EP,1} - \omega_{EP,2})t]. \tag{1.50}$$

So, for reading the angular velocity in an anti-PT-symmetric gyroscope, it would be sufficient to apply the Fast Fourier Transform (FFT) to the electrical signal read by the oscilloscope.

Moreover, in the anti-PT-symmetric gyroscope it is easy to detect the sign of the angular velocity, differently from the PT-symmetric gyroscope. In order to distinguish the direction of rotation in the anti-PT-symmetric gyroscope, it should be noted that the rotation-induced splitting, $\Delta\omega_{EP}$, is real only if $\Delta\omega_\Omega > 0$. In case of rotation in the opposite direction, no real splitting would be appreciated, because $\Delta\omega_{EP}$ becomes imaginary. Identifying the angular velocity from imaginary frequency splitting would need a fitting model. A much easier solution would need to inject the input light from port 3 and read the output at port 4. In this case $\Delta\omega_\Omega$ becomes negative and $\Delta\omega_{EP}$ real. So, having light sources at both port 1 and 3 would let the device read the angular velocity in both directions of rotation.

Stability analysis of parity-time- and anti-parity-time-symmetric gyroscopes

We want to underline that the so proposed anti-PT-symmetric gyroscope has the important advantage over the PT-symmetric counterpart (where $\omega_0 = \omega_1 = \omega_2$ and $\gamma_1 = -\gamma_2$) of exhibiting a real splitting, differently from the complex splitting in the PT-symmetric gyroscope ($\Delta\omega_{PT,EP} = (1+j)\sqrt{k_c \Delta\omega_\Omega}$, with k_c the direct coupling strength between the two resonators). The real splitting of the anti-PT-symmetric gyroscope can be easily read through the beating frequency at the output of the photoreceiver. The real splitting has an important consequence over the stability analysis. In order to analyse the stability of the proposed gyroscope, we need to perform a time-domain analysis. The time behaviour of the of the modes in the cavities are easily found in the time domain, by using the found eigenfrequencies [98]:

$$a_{1,2} \approx e^{j\omega_{EP_{1,2}}} = e^{j\left(\frac{\omega_1+\omega_2}{2} \pm \sqrt{|k_c|\Delta\omega_\Omega}\right)t} e^{-\gamma t}. \tag{1.51}$$

These two modes are both stable, because the real part of the argument of the exponential term is negative (provided that $\Delta\omega_\Omega > 0$).

Whereas, in the PT-symmetric case,

$$a_{1,2_{PT}} \approx e^{j\omega_{PT,EP_{1,2}}} = e^{j\omega_0} e^{\pm\sqrt{k_c \Delta\omega_\Omega}}, \tag{1.52}$$

the square root term leads to a divergent mode, making the system unstable. A solution to make the PT-symmetric stable would be to make it quasi-PT-symmetric, with the average gain of the resonators being negative ($\gamma_1' + \gamma_2' < 0$), by adding an additional common loss to both the resonators. However, as the eigenfrequency splitting is complex, the readout system would be difficult (see Table 1.2).

PT	quasi-PT	anti-PT
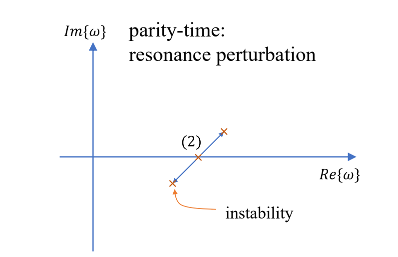	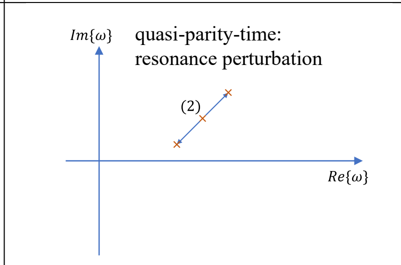	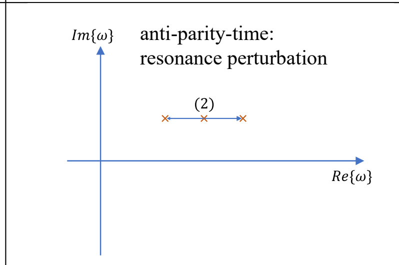
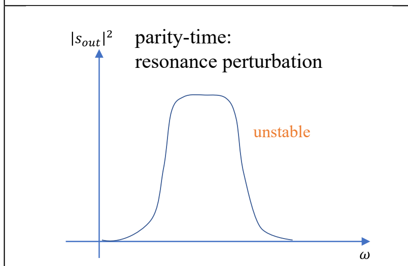	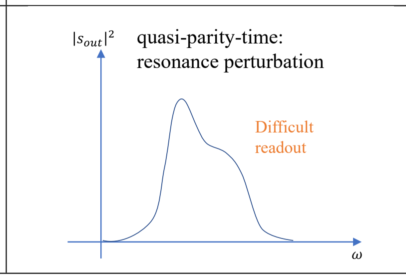	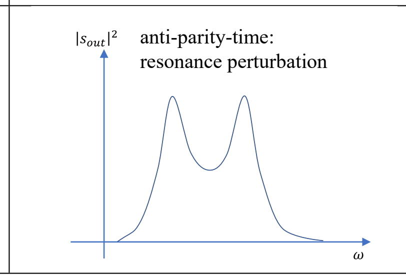

Table 1.2: PT vs quasi-PT vs anti-PT analysis.

1.3.3 Considerations about anti-parity-time-symmetric system

In this section the idea of an anti-parity-time-symmetric gyroscope has been developed. In particular, it has been shown that its sensitivity is independent from the dimensions of the device. As a result, the device presents an incredibly enhanced sensitivity, even at the microscale. For integrated devices (micrometric dimensions) the sensitivity of a anti-PT-symmetric device could be 10^6 times higher than a classical Sagnac gyroscope. However, the configuration proposed could present some difficulties in terms of fabrication. In particular, making $\phi_{1,2}$ in Eq. 1.38 an exact multiple of π could be experimentally difficult, since the uncertainty on the effective index during the design. Consequently, k_c could show also a real part, and the minimum detectable angular velocity would increase accordingly to Eqs. 1.48 and 1.49.

1.4 A real-splitting resonator-waveguide-resonator anti-parity-time-symmetric integrated optical gyroscope

1.4.1 Indirect-coupling anti-parity-time-symmetric optical systems

The configuration for an anti-parity-time symmetric-gyroscope recently proposed in literature for the first time [13] has been extensively shown in the previous section. As, demonstrated, the anti-parity-time-symmetric system requires an indirect coupling between optical resonator. The solution for the indirect coupling proposed in the previous section makes use of an auxiliary U-shaped waveguide to couple two resonators. However, in such a way, the coupling between the cavities could be easily nonreciprocal and could be affected by fabrication errors and mismatches between the length of auxiliary waveguides, causing the system to exit the exceptional point and vanishing all the advantages of the anti-parity-time-symmetric solution. A critical control over the design and fabrication constraints on the coupling waveguide would then be necessary. The goal of this section is to design an indirectly-coupled-resonators anti-parity-time-symmetric optical gyroscope making use of only one straight auxiliary waveguide to couple the two resonators and achieve reciprocal indirect coupling. With the proposed design, we can avoid any problem in terms of design and fabrication errors over the length of the auxiliary waveguides. In order to achieve this goal a resonator-waveguide-resonator coupler is proposed.

To demonstrate the feasibility of the device, a solution compatible with the InP-platform will be investigated. The proposed device is shown in Figures 1.15a (configuration A, with external buses) and 1.15b (configuration B, without external coupling buses) in two different configurations. Equation 1.53 describes the energy exchanges between the optical modes a_1 and a_2 inside the two resonators in the time domain for the configuration A [99]:

$$\frac{d\boldsymbol{a}}{dt} = \left(j\boldsymbol{\omega} - \boldsymbol{\gamma_i} - \boldsymbol{\gamma_{ext}} - \boldsymbol{\Gamma}\right)\boldsymbol{a} + j\boldsymbol{\mu_{ext}}\boldsymbol{s_{in,A}}, \tag{1.53}$$

$$s_{out} = j\boldsymbol{\mu}\boldsymbol{a}, \tag{1.54}$$

with

$$\begin{gathered}\boldsymbol{a} = \begin{bmatrix} a_1 \\ a_2 \end{bmatrix}, \boldsymbol{\omega} = \begin{bmatrix} \omega_1 & 0 \\ 0 & \omega_2 \end{bmatrix}, \boldsymbol{\gamma_i} = \begin{bmatrix} \gamma_{i1} & 0 \\ 0 & \gamma_{i2} \end{bmatrix}, \boldsymbol{\gamma_{ext}} = \begin{bmatrix} \gamma_{ext,1} & 0 \\ 0 & \gamma_{ext,2} \end{bmatrix}, \\ \boldsymbol{\mu} = \begin{bmatrix} \mu_1 \\ \mu_2 \end{bmatrix}^T, \boldsymbol{\mu_{ext}} = \begin{bmatrix} \mu_{ext,1} & 0 \\ 0 & \mu_{ext,2} \end{bmatrix}, \boldsymbol{s_{in,A}} = \begin{bmatrix} s_{in} \\ 0 \end{bmatrix},\end{gathered} \tag{1.55}$$

where the parameters with subscript 1 and 2 correspond to resonators 1 and 2, respectively. The term $\omega_{1,2}$ represents the resonance angular frequency of each isolated resonator, $\gamma_{i1,i2}$ is the inverse of the photon lifetime in the isolated ring (net value of the intrinsic loss and the applied gain), $\gamma_{ext,1,ext,2}$ is the inverse of the photon lifetime due to the coupling to the external buses, $\mathbf{\Gamma}$ is the decay rate matrix (it takes into account the energy exchange between the resonators and will be evaluated by using energy conservation observations), s_{in} is the amplitude of the input wave and $\mu_{1,2}$ ($\mu_{ext1,2}$) is the coupling strength between the central bus (external buses) and each resonator and can be evaluated as follows [82]:

$$\begin{aligned}\mu_{1,2}^2 &= \frac{\eta_{1,2}^2 v_g}{P_{1,2}}, \\ \mu_{ext1,2}^2 &= \frac{\eta_{ext1,2}^2 v_g}{P_{1,2}},\end{aligned} \tag{1.56}$$

with $\eta_{1,2}^2$ ($\eta_{ext1,2}^2$) the fraction of coupled power across the corresponding coupler.

Equation 1.53 can be modified to describe the energy exchanges between the optical modes a_1 and a_2 inside the two resonators in the time domain for the configuration B [99]:

$$\frac{d\boldsymbol{a}}{dt} = (j\boldsymbol{\omega} - \boldsymbol{\gamma_i} - \mathbf{\Gamma})\,\boldsymbol{a} + j\boldsymbol{\mu}^T s_{in}, \tag{1.57}$$

$$s_{out} = s_{in} + j\boldsymbol{\mu}\boldsymbol{a}. \tag{1.58}$$

As shown in [99] the terms $\boldsymbol{\mu}$ and $\boldsymbol{\Gamma}$ can be related using power conservation. Since the overall power is being conserved, we can evaluate $\boldsymbol{\Gamma}$, when all the other sources of loss are neglected [99]:

$$\frac{d(\boldsymbol{a}\boldsymbol{a}^*)}{dt} + s_{out}s_{out}^* = -2\boldsymbol{a}\boldsymbol{\Gamma}\boldsymbol{a}^* + \boldsymbol{a}^*\boldsymbol{\mu}^*\boldsymbol{\mu}\boldsymbol{a} = 0. \tag{1.59}$$

We can obtain the expression of the matrix $\boldsymbol{\Gamma}$:

$$\boldsymbol{\Gamma} = \frac{1}{2}\boldsymbol{\mu}^*\boldsymbol{\mu} = \frac{1}{2}\begin{bmatrix} \mu_1^2 & \mu_1\mu_2 \\ \mu_1\mu_2 & \mu_2^2 \end{bmatrix}, \tag{1.60}$$

After defining $\gamma'_{1,2} = \left(\gamma_{i,2} + \frac{\mu^2_{ext,1,2}}{2} + \frac{\mu^2_{1,2}}{2}\right)$ (with $\mu_{ext,1,2} = 0$ for configuration B) and $\kappa = \mu_1\mu_2/2$, we can rewrite Eq. 1.53, for the configuration A, as:

$$\frac{da_1}{dt} = j\omega_1 a_1 - \gamma'_1 a_1 - \kappa a_2 + j\mu_{ext}s_{in}, \tag{1.61}$$

$$\frac{da_2}{dt} = j\omega_2 a_2 - \gamma'_2 a_2 - \kappa a_1 \tag{1.62}$$

and Eq. 1.57, for the configuration B, as:

$$\frac{da_1}{dt} = j\omega_1 a_1 - \gamma'_1 a_1 - \kappa a_2 + j\mu_1 s_{in}, \tag{1.63}$$

$$\frac{da_2}{dt} = j\omega_2 a_2 - \gamma'_2 a_2 - \kappa a_1 + j\mu_2 s_{in}. \tag{1.64}$$

For $\omega_1 \neq \omega_2$, $\gamma' = \gamma'_1 = \gamma'_2$, after a simple variable change ($\tilde{a_{1,2}} = a_{1,2}e^{-j\omega_0 t}$, with $\omega_0 = (\omega_1 + \omega_2)/2$) the system (in both the configurations) is found to be anti-parity-time-symmetric and we can use this device to design an anti-parity-time-symmetric gyroscope. We will continue to refer to equations 1.61, 1.62,1.63 and 1.64 since the properties of the eigenfrequencies are the same without the variable change. The problem of an accurate design of the length of the coupling waveguides in [13] is thus overcome, since we have designed an anti-parity-time-symmetric optical system with a single auxiliary coupling waveguide, without requirements on its length accuracy.

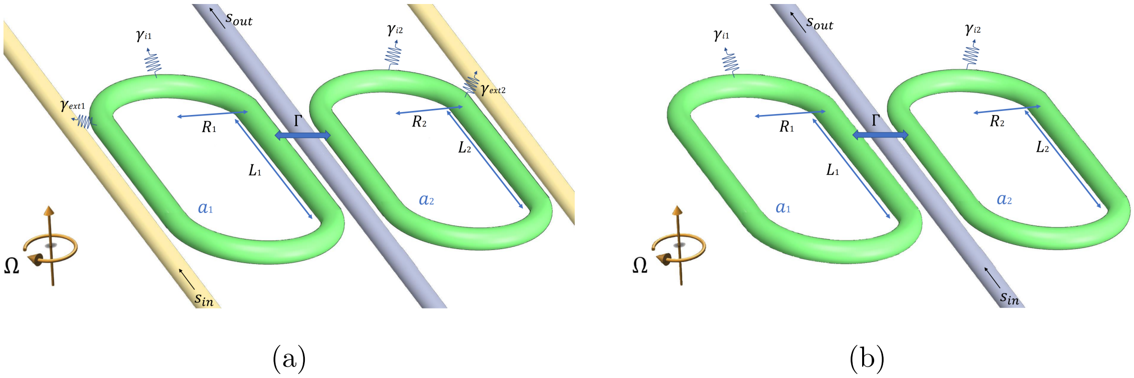

Figure 1.15: (a) Indirect-coupling anti-parity-time-symmetric optical system with external buses (Configuration A). (b) Indirect-coupling anti-parity-time-symmetric optical system, without external buses (Configuration B).

1.4.2 Anti-PT-symmetric gyroscope

Eigenfrequency splitting

The eigenfrequencies of the anti-PT-symmetric system described by Eqs. 1.61, 1.62, 1.63 and 1.64 are easily found to be:

$$\omega_{aPT_{1,2}} = \frac{\omega_1 + \omega_2}{2} + j\frac{\gamma_1' + \gamma_2'}{2} \pm \sqrt{\left(\frac{\omega_1 - \omega_2}{2}\right)^2 - \kappa^2}. \tag{1.65}$$

When the eigenfrequencies coalesce the system is said to be at the exceptional point ($|\omega_1 - \omega_2| = 2\kappa$).

If the system is designed to work around its exceptional point when the angular velocity $\Omega = 0$, for $\Omega \neq 0$ the eigenfrequencies become:

$$\omega_{EP_{1,2}} = \frac{\omega_1 + \omega_2}{2} + j\gamma' \pm \sqrt{\kappa \Delta\omega_\Omega}, \tag{1.66}$$

where

$$\Delta\omega_\Omega = \frac{4\pi\Omega}{\lambda}(A_1/P_1 + A_2/P_2), \tag{1.67}$$

where λ is the wavelength in vacuum, P_i and A_i are the perimeter and the enclosed area of the i-th resonator.

Recalling from [82] that $\mu_{1,2}^2$ is proportional to the fraction of the power coupled from the bus to the ring ($\eta_{1,2}^2$) and to the inverse of the length of the cavity ($\mu_{1,2}^2 = \eta_{1,2}^2 \frac{v_g}{P_{1,2}}$), if the system is designed to have $A_1 \approx A_2$ and $P_1 \approx P_2$, we can define:

$$c_i = \frac{A_i}{P_i^2} = \frac{2R_i/L_i + \pi(R_i/L_i)^2}{(2\pi R_i/L_i + 2)^2}, \tag{1.68}$$

with R_i and L_i the radius of curvature and the length of the straight waveguide of the racetrack resonator (see Figure 1.15a). Starting from Eq. 1.67 and using Eq. 1.68 and Eq. 1.56, we can obtain:

$$\Delta\omega_{EP} \approx \sqrt{\frac{4\pi\eta_1\eta_2 v_g}{\lambda} c\Omega}, \tag{1.69}$$

where $c = c_1 \approx c_2$.

As in the previously proposed ring-resonator-based PT-symmetric [11] and anti-PT-symmetric gyroscopes [13], the eigenfrequency splitting is independent on the dimensions of the device, once the ratios R_i/L_i have been chosen. In this way the limitation of the Sagnac splitting is overcome. As in the PT-symmetric case, the splitting is proportional to $\sqrt{\Omega}$, thus leading to enhanced splitting between the eigenfrequencies in the proximity of the exceptional point.

Coupling strength control

We want to stress that, using a single waveguide to couple two resonators has an important advantage. When using the U-shaped waveguide to couple two resonators (as shown in [13] and [89]), an error over the length of the coupling waveguides could not only increase the difficulty in approaching the exceptional point condition (worsening the detectivity of the device), but could also cause the coupling strength and, consequently, the eigenfrequency splitting to become complex, making the read-out scheme not efficient. The resonator-waveguide-resonator coupler ensures much more reliability and control over the coupling strength of the system, by keeping the value of κ^2 real. Moreover, with the proposed structure, an easy way to electrically fine tune the system around the exceptional point is possible through the control of the loss/gain in the coupling region and the consequent variation of the coupling strength.

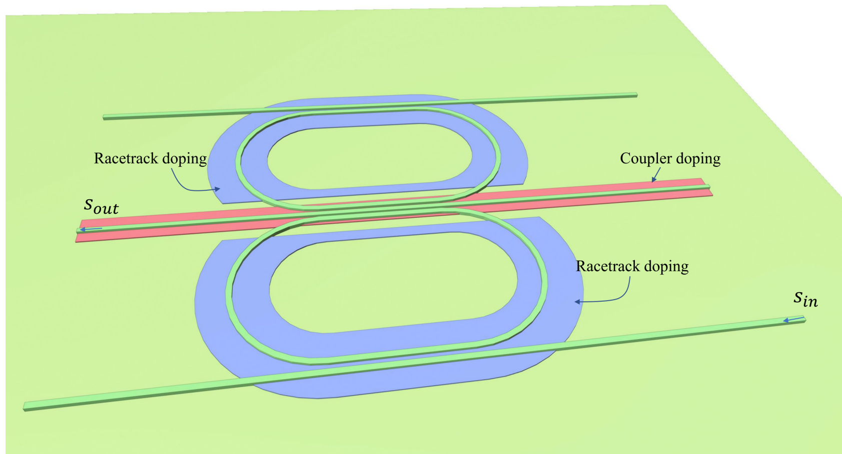

Figure 1.16: Design proposal for an optical anti-parity-time-symmetric optical gyroscope on InP platform.

In the previous paragraph the coupling mechanism has been supposed to be lossless, however, when considering a lossy coupler, an additional source of loss should be accounted in $\gamma'_{1,2}$

$$\gamma'_{1,2} = \left(\gamma_{i,2} + \frac{\mu^2_{add,1,2}}{2} + \frac{\mu^2_{ext,1,2}}{2} + \frac{\mu^2_{1,2}}{2}\right), \tag{1.70}$$

where:

$$\mu^2_{add_{1,2}} = \frac{\chi^2_{1,2} v_g}{(2\pi R_{1,2})}, \tag{1.71}$$

with $\chi^2_{1,2}$ the fraction of power lost in the coupling region.

Design and results

In this section we show our proposal for integrating the anti-parity-time-symmetric gyroscope on an InP platform, using the configuration A. The proposed architecture is shown in Fig. 1.16 and will be explained in the following paragraphs.

Cross-section design

Here the material composition and the thickness of each layer of the cross-section in Figure 1.17a (where the symbols in brackets represent the type of doping) is listed, with the corresponding p-type (p) or n-type (n) doping concentration:

-InP-p (1000 nm, $p = 1.5 \cdot 10^{18}$ cm^{-3}, refractive index=3.17)

-InP-p (250 nm, $p = 8 \cdot 10^{17}$ cm^{-3}, refractive index=3.17)

-InP-p (150 nm, $p = 5 \cdot 10^{17}$ cm^{-3}, refractive index=3.17)

-$In_{0.6}Ga_{0.4}As_{0.85}P_{0.15}$ (250 nm, refractive index = 3.50 [100])

-InP-n (1000 nm, $n = 1 \cdot 10^{18}$ cm^{-3}, refractive index=3.17)

The material gain of the InGaAsP has been evaluated using the semi-empirical model proposed in [101], using the parameters used in the simulation tool (Table I of [101]). The predicted material gain as a function of the carrier density for a wavelength of 1.55 μm is shown in Figure 1.17b. The predicted gain is the linear gain of the material, excluding saturation effects. However, since in [101] the gain refers to power, the values obtained using the model [101] have been halved, in order to obtain the amplitude gain. Such an approach is a good approximation for small gains and small field amplitudes, in order to avoid saturation and cross-saturation effects. Once the confinement factor $\Gamma_g = 59,93\%$ has been evaluated, the net gain can be calculated as $\gamma_i = -\Gamma_g g_m$ (by considering the other materials lossless).

Figure 1.17a shows the cross section of the InP waveguide, common to all the waveguides and the resonators of the designed gyroscope, including the auxiliary waveguide.

Coupler design

After that, we designed the coupling region with a propagator software. The value of $\eta_{1,2}$ can be obtained by evaluating the fraction of power coupled from the racetrack to the auxiliary waveguide (same in the opposite direction). After that, Eq. 1.56 can be used to compute $\mu_{1,2}$. It should be noted that the coupling region can be electrically isolated from the rest of the device (by means of an undoped region in between), in order to make it possible to control the coupling strength by tuning the gain in the coupling region, separately from the gain of the two resonators (Figure 1.16). In fact, by controlling the gain in the coupling region, while compensating

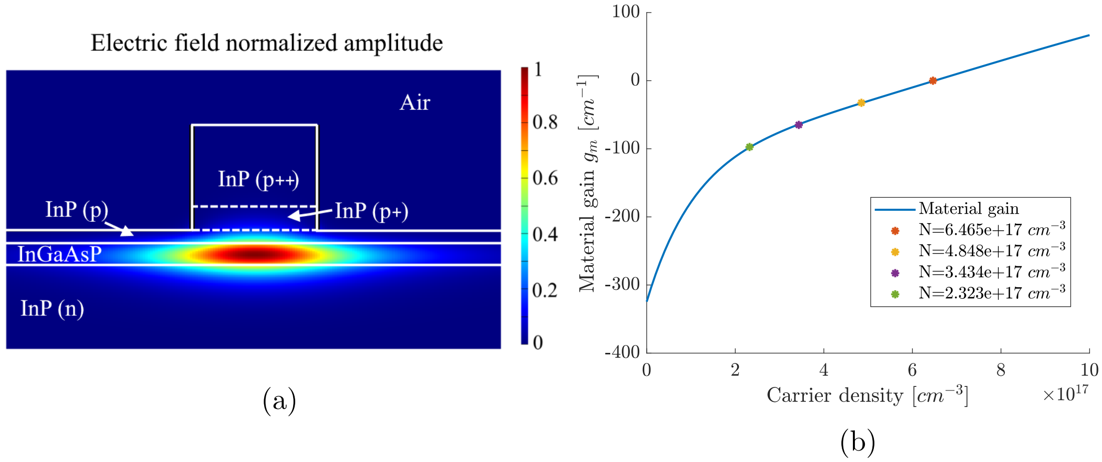

Figure 1.17: (a) Normalized electric field and cross section of the waveguide adopted in all the regions of the integrated gyroscope. (b) Material gain of InGaAsP as a function of the density of the injected carriers, obtained by halving the material gain obtained from model in [101] (to obtain the amplitude gain). The marked dots in the legend represent the values of the carrier density, used in the design of the coupler.

the losses of the InGaAsP material, it is possible to control the quantity $\eta_{1,2}$. Figure 1.18 shows the coupling power coefficient for different carrier injection level in the coupling region, varying with the length of the straight coupling region.

As it can be seen for a InGaAsP material gain ranging from -24 to 0 cm^{-1} (corresponding to a carrier injection ranging from 2.323×10^{17} to 4.465×10^{17}cm^{-3}, the coupled power fraction at $L_1 = L_2 = 84$ μm goes from less than 10% to 55%. This means having a wide range of tuneability for κ. The value of the gain is negative, because we only use carrier injection to partially compensate the losses due to absorption up to the transparency condition.

Gyroscope design

For evaluating the performances of the device, we designed it at the exceptional point.

The values chosen for the simulations are summarized in Table 1.3.

In particular, after the isolated eigenfrequencies ω_1 and ω_2 have been calculated, by using the effective index (value in Table 1.3) and the lengths of the perimeters of

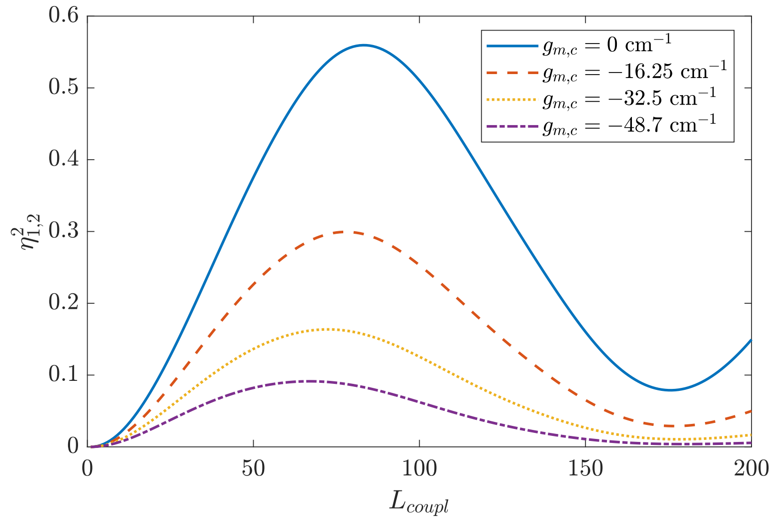

Figure 1.18: Coupling efficiency $\eta_{1,2}$ for different values of the material gain of the InGaAsP region, corresponding to the carrier density N marked in Figure 1.17b.

Parameter	Value
n_{eff}	3.26
R_1	50 μm
R_2	50.6 μm
L_1	84 μm
L_2	84 μm
γ'_1	5×10^4 rad/s
γ'_2	5×10^4 rad/s

Table 1.3: Parameters used in the simulations.

the racetracks ($P_{1,2} = 2\pi R_{1,2} + 2L_{1,2}$), the coupling strength κ has been designed as:

$$\kappa = |\omega_1 - \omega_2|/2 \tag{1.72}$$

Once the value of κ has been obtained ($\kappa \approx 1.90 \times 10^{11}$rad/s), we fixed $\eta_1 = \eta_2$ and evaluated μ_1 and μ_2 using Eq. 1.56 and knowing that $\kappa = \mu_1\mu_2/2$. We obtained $\mu_1 \approx 6.1783 \times 10^5$ (rad/s)$^{1/2}$ and $\mu_2 \approx 6.1543 \times 10^5$ (rad/s)$^{1/2}$ ($\eta^2_{1,2} \approx 0.4989$).

We will use consider configuration A to evaluate the internal gain of the resonators (-$\gamma'_{i,1,2}$). Using $\gamma'_{1,2}$ in Table 1.3, by neglecting $\mu^2_{add,1,2}/2$ (since the coupler is designed near transparency), using the calculated values for μ_1 and μ_2, and assuming $\mu_{ext,1,2} = \mu_{1,2}$ we obtain $\gamma_{i,1} = -9.5022 \times 10^{10}$ rad/s and $\gamma_{i,2} = -9.4284 \times 10^{10}$ rad/s, corresponding to gains per length of 10.32 cm^{-1} and 10.24 cm^{-1}, respectively. To obtain these values approximate carrier injections of 7.37×10^{17} cm^{-3} and 7.38×10^{17} cm^{-3} are necessary, respectively (calculated using the value of the confinement factor Γ_g and the model in Figure 1.17b). It should be noted that these values are approximated, arising from a simplified model. They should be helpful in the design of the device, but the external tuning is critical to place the device at the exceptional point. The results of the output spectrum ($|s_{out}|^2$) are shown in Figure 1.19a. Figure 1.19b shows the eigenfrequency splitting as a function of the angular velocity of the proposed anti-PT-symmetric gyroscope compared to the classical Sagnac splitting on a single resonator of the same dimensions of one the designed resonators. The performance obtained with the new proposed resonator-waveguide-resonator configuration is comparable with that obtained in [13]. In fact, equations 1.61-1.64 are formally equivalent to those describing the anti-PT-symmetric gyroscope in [13]. So, provided that the coupling strengths are the same, the same sensitivity can be achieved.

Finally, Figures 1.20a and 1.20b show the time behaviour of output optical power $|s_{out}|^2$ read at a photodetector. In this way it is easy to appreciate that the system is stable and that it would be possible to extract the angular velocity of the gyroscope using some basic electronic signal processing.

1.4.3 Final considerations

A new architecture for an anti-PT-symmetric integrated optical gyroscope has been shown. The gyroscope is realized using two resonators indirectly coupled by means of one auxiliary waveguide. With respect to the previously proposed anti-PT-symmetric gyroscope, the use of only one straight auxiliary waveguide drastically reduces the critical problems in achieving the exceptional point. Moreover, the sensitivity of the gyroscope has been demonstrated to be independent from the dimensions of the device, even for racetrack resonators. Such a conclusion represents a noticeable progress with respect to the classical Sagnac effect, limited by the dependence of the sensitivity on the radius of the ring resonator.

As a result, the device shows an incredibly enhanced sensitivity with respect to the classical Sagnac effect on a device of the same dimensions: the sensitivity of

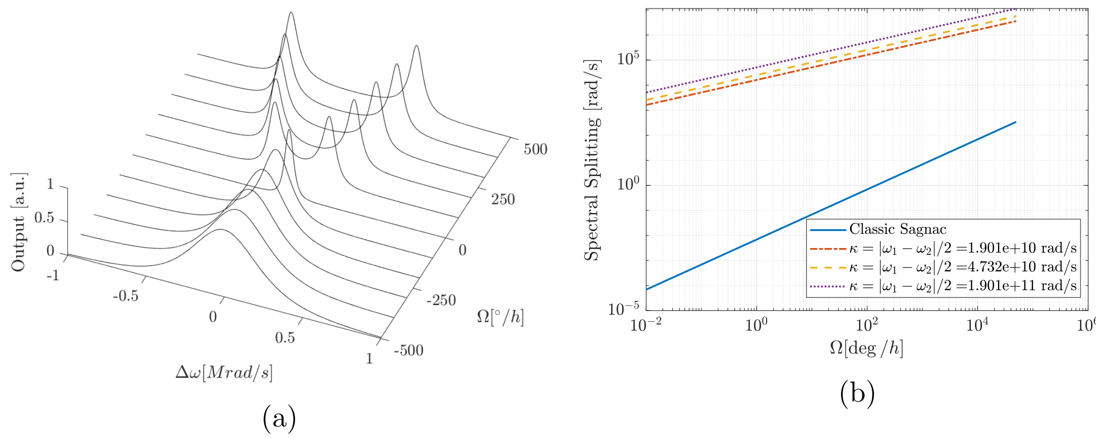

Figure 1.19: (a) Spectrum of the output signal of the gyroscope as a function of the angular velocity and of the frequency detuning from ω_0. (b) Splitting as a function of the angular velocity.

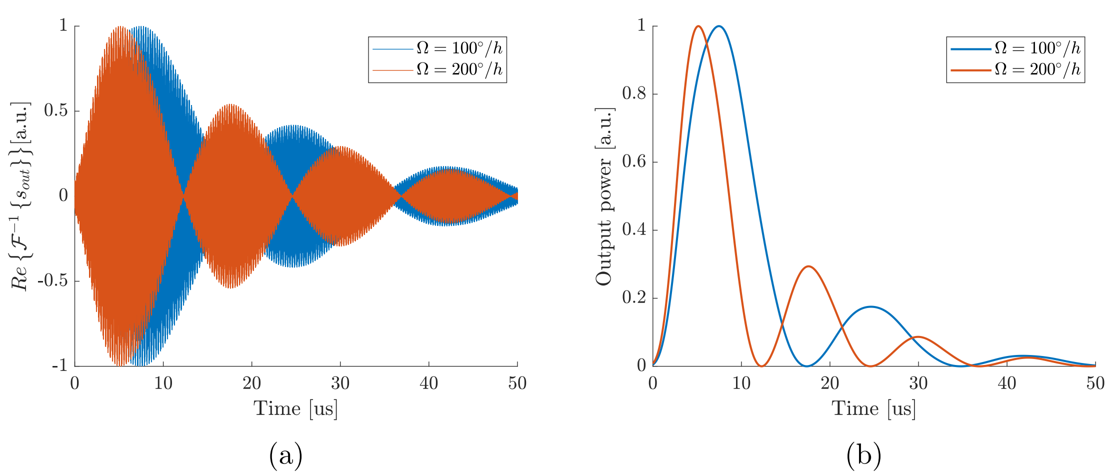

Figure 1.20: (a) Normalized real part of the output signal s_{out} in the time domain. (b) Normalized $|s_{out}|^2$ in the time domain, representing the average optical power at the photoreceiver.

an anti-PT-symmetric micrometric gyroscope could be several orders of magnitude higher than a classical Sagnac gyroscope.

This solution seems to be much more suitable for angular velocity sensing than the PT-symmetric gyroscope. In fact, the anti-PT-symmetric gyroscope exhibits a real resonance splitting, with respect to the PT-symmetric one. Finally, we believe that the device we modelled could pave the way to a new generation of integrated optical gyroscopes, breaking the limit of micrometric dimensions.

Chapter 2

Optomechanical forces

2.1 Optomechanical forces

In this chapter an overview about optical forces will be presented. Then, new results will be shown, both theoretical and experimental. In particular, a generalized method for evaluating optical forces in an optomechanical system using an energetic approach will be investigated. Next the dynamics of coupled suspended optical waveguides, excited by optical forces, will be carried on and a numerical algorithm to simulate the time evolution of the system will be proposed. Finally, an experimental work about an optomechanical switch, performed at the Optoelectronics Research Centre of the University of Southampton, will be presented.

2.1.1 Radiation pressure and optical gradient force

Optical forces can be generally divided into two major categories, i.e., radiation pressure and transverse gradient forces. Radiation pressure acts along the light propagation direction. The momentum carried by an electromagnetic wave of irradiance (power per unit of surface) I_f is:

$$p = \frac{I_f}{c}, \tag{2.1}$$

with c the speed of light in vacuum. If the light is totally absorbed by a black body, the component of that momentum normal to the surface of the body is transferred to

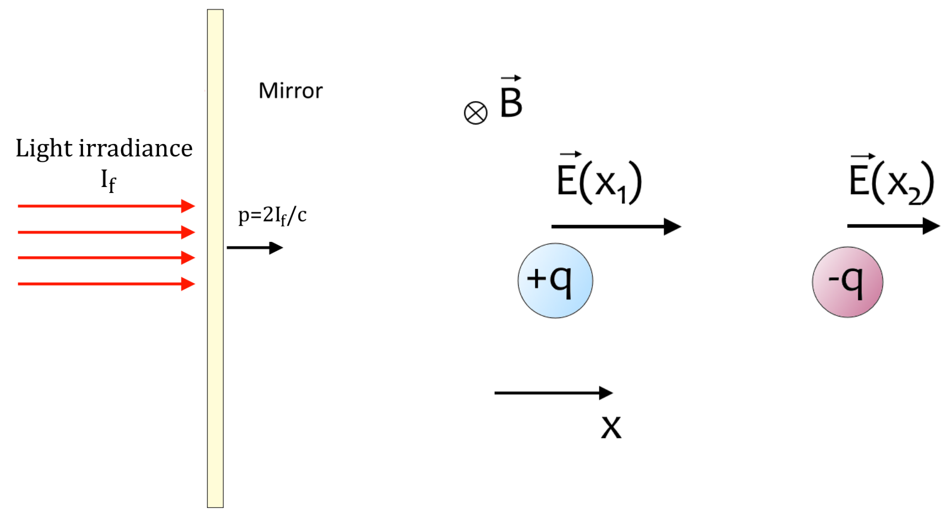

(a)

(b)

Figure 2.1: Radiation pressure on a moveable mirror (a). Electric field and magnetic field on a dipole, causing optical gradient force (b).

it. The transferred momentum is called "radiation pressure". If the body hit by the electromagnetic wave is a perfect reflector, according to the momentum conservation law, the radiation pressure is equal to [14]:

$$p = p_{incident} + p_{emitted} = 2\frac{I_f}{c}. \tag{2.2}$$

Differently, the optical gradient force acts transversely to the propagation direction of the light. The force acting on a single charge in an electromagnetic field is [102]:

$$\mathbf{F}_1 = q\left(\mathbf{E}(\mathbf{x}_1) + \frac{d\mathbf{x}_1}{dt} \times \mathbf{B}\right). \tag{2.3}$$

Let's suppose to have a dipole (representing a molecule of a dielectric material), with a distance between the two charges of $\mathbf{x_1} - \mathbf{x_2}$:

$$\mathbf{F} = q\left(\mathbf{E}(\mathbf{x}_1) - \mathbf{E}(\mathbf{x}_2) + \frac{d\left(\mathbf{x}_1 - \mathbf{x}_2\right)}{dt} \times \mathbf{B}\right) = q\left(\left(\left(\mathbf{x}_1 - \mathbf{x}_2\right) \cdot \nabla\right)\mathbf{E} + \frac{d\left(\mathbf{x}_1 - \mathbf{x}_2\right)}{dt} \times \mathbf{B}\right). \tag{2.4}$$

By defining the dipole momentum $\mathbf{p} = q(\mathbf{x_1} - \mathbf{x_2})$ and supposing a linear medium, with $\mathbf{p} = \alpha\mathbf{E}$:

$$\mathbf{F} = (\mathbf{p} \cdot \nabla)\mathbf{E} + \frac{d\mathbf{p}}{dt} \times \mathbf{B} = \alpha\left[(\mathbf{E} \cdot \nabla)\mathbf{E} + \frac{d\mathbf{E}}{dt} \times \mathbf{B}\right]. \tag{2.5}$$

By using the vectorial identity

$$(\mathbf{E} \cdot \nabla)\mathbf{E} = \nabla\left(\frac{1}{2}E^2\right) - \mathbf{E} \times (\nabla \times \mathbf{E}) \tag{2.6}$$

and the Maxwell equation

$$\nabla \times \mathbf{E} = -\frac{\partial \mathbf{B}}{\partial t}, \tag{2.7}$$

we can find the final expression:

$$\mathbf{F} = \alpha\left[\frac{1}{2}\nabla E^2 - \mathbf{E} \times (\nabla \times \mathbf{E}) + \frac{d\mathbf{E}}{dt} \times \mathbf{B}\right] = \alpha\left[\frac{1}{2}\nabla E^2 + \frac{d}{dt}(\mathbf{E} \times \mathbf{B})\right]. \tag{2.8}$$

Being $\mathbf{E} \times \mathbf{B}$ proportional to the Poyinting vector, that is constant (or slowly variable, depending on the case), its derivative in time is equal to zero. So, the final expression for the optical gradient force is:

$$\mathbf{F} = \frac{1}{2}\alpha\nabla E^2 \tag{2.9}$$

The name of the force arises from the expression of the force that is proportional to the gradient of the square of the norm of the electric field.

2.1.2 Maxwell stress tensor

In order to derive a general way to evaluate optical forces, we start with the Lorentz force law [103]:

$$\mathbf{F} = q(\mathbf{E} + \mathbf{v} \times \mathbf{B}). \tag{2.10}$$

The force per unit volume is:

$$\mathbf{f} = \rho\mathbf{E} + \mathbf{J} \times \mathbf{B}. \tag{2.11}$$

By using Gauss's law and Ampère's circuital law, we can replace ρ and $\mathbf{J}$ and obtain:

$$\mathbf{f} = \epsilon_0(\boldsymbol{\nabla} \cdot \mathbf{E})\mathbf{E} + \frac{1}{\mu_0}(\boldsymbol{\nabla} \times \mathbf{B}) \times \mathbf{B} - \epsilon_0 \frac{\partial \mathbf{E}}{\partial t} \times \mathbf{B}. \tag{2.12}$$

In order to rewrite the time derivative term, we can use the product rule and the Maxwell equation ($\nabla \times \mathbf{E} = -\frac{d\mathbf{B}}{dt}$)

$$\frac{\partial}{\partial t}(\mathbf{E} \times \mathbf{B}) = \frac{\partial \mathbf{E}}{\partial t} \times \mathbf{B} + \mathbf{E} \times \frac{\partial \mathbf{B}}{\partial t} = \frac{\partial \mathbf{E}}{\partial t} \times \mathbf{B} - \mathbf{E} \times (\nabla \times \mathbf{E}). \tag{2.13}$$

The term $\mathbf{f}$ can now be rewritten as:

$$\mathbf{f} = \epsilon_0[(\boldsymbol{\nabla} \cdot \mathbf{E})\mathbf{E} - \mathbf{E} \times (\boldsymbol{\nabla} \times \mathbf{E})] + \frac{1}{\mu_0}[-\mathbf{B} \times (\boldsymbol{\nabla} \times \mathbf{B})] - \epsilon_0 \frac{\partial}{\partial t}(\mathbf{E} \times \mathbf{B}). \tag{2.14}$$

In order to create a symmetry between $\mathbf{E}$ and $\mathbf{B}$, we can add the term $(\nabla \cdot \mathbf{B})\mathbf{B}$ (null because of one Maxwell equation):

$$\mathbf{f} = \epsilon_0[(\boldsymbol{\nabla} \cdot \mathbf{E})\mathbf{E} - \mathbf{E} \times (\boldsymbol{\nabla} \times \mathbf{E})] + \frac{1}{\mu_0}[(\boldsymbol{\nabla} \cdot \mathbf{B})\mathbf{B} - \mathbf{B} \times (\boldsymbol{\nabla} \times \mathbf{B})] - \epsilon_0 \frac{\partial}{\partial t}(\mathbf{E} \times \mathbf{B}). \tag{2.15}$$

Now we can eliminate the curl, using the vector calculus identity

$$\frac{1}{2}\boldsymbol{\nabla}(\mathbf{A} \cdot \mathbf{A}) = \mathbf{A} \times (\boldsymbol{\nabla} \times \mathbf{A}) + (\mathbf{A} \cdot \boldsymbol{\nabla})\mathbf{A} \tag{2.16}$$

and obtain

$$\begin{aligned}\mathbf{f} = \epsilon_0[(\boldsymbol{\nabla}\cdot\mathbf{E})\mathbf{E} + (\mathbf{E}\cdot\boldsymbol{\nabla})\mathbf{E}] + \tfrac{1}{\mu_0}[(\boldsymbol{\nabla}\cdot\mathbf{B})\mathbf{B} + (\mathbf{B}\cdot\boldsymbol{\nabla})\mathbf{B}] + \\ -\tfrac{1}{2}\boldsymbol{\nabla}\left(\epsilon_0 E^2 + \tfrac{1}{\mu_0}B^2\right) - \epsilon_0\tfrac{\partial}{\partial t}(\mathbf{E}\times\mathbf{B}).\end{aligned} \tag{2.17}$$

We can finally define the Maxwell Stress Tensor as

$$\sigma_{ij} \equiv \epsilon_0\left(E_iE_j - \frac{1}{2}\delta_{ij}E^2\right) + \frac{1}{\mu_0}\left(B_iB_j - \frac{1}{2}\delta_{ij}B^2\right) \tag{2.18}$$

and rewrite $\mathbf{f}$:

$$\mathbf{f} = \nabla\cdot\boldsymbol{\sigma} - \epsilon_0\mu_0\frac{\partial\mathbf{S}}{\partial t}. \tag{2.19}$$

2.1.3 Optical gradient force in coupled optical waveguides

Using the Maxwell Stress Tensor can be computationally too expensive. So, energetic approaches are usually preferred, where applicable.

The calculation of the optical gradient force between two optical coupled waveguides is one of the cases where an energetic approach can be used. Let's suppose that energy $U = N\hbar\omega$ (with ω the angular frequency, $\hbar$ the Planck constant and N the number of injected photons) is coupled into an eigenmode (even or odd supermode [104]) of the system of two waveguides separated by a distance ξ. An adiabatic change in separation $\Delta\xi$ will shift the eigenmode angular frequency by $\Delta\omega$ (the wave vector is conserved because of the preservation of translational invariance) and will result in the mechanical force [35]:

$$F = -\left.\frac{dU}{d\xi}\right|_{\mathbf{k}} = -\left.\frac{d(N\hbar\omega)}{d\xi}\right|_{\mathbf{k}} = -N\hbar\left.\frac{d\omega}{d\xi}\right|_{\mathbf{k}}. \tag{2.20}$$

So by using the chain rule, we obtain:

$$F = -\frac{U}{\omega}\left.\frac{d\omega}{dn_{eff}}\right|_{\mathbf{k}}\left.\frac{dn_{eff}}{d\xi}\right|_{\omega} = -\frac{U}{n_{eff}}\left.\frac{dn_{eff}}{d\xi}\right|_{\omega}. \tag{2.21}$$

Finally, considering a lenght L of the waveguide, the force per unit length is:

$$\frac{F}{L} = -\frac{P}{c}\left.\frac{dn_{eff}}{d\xi}\right|_{\omega}. \tag{2.22}$$

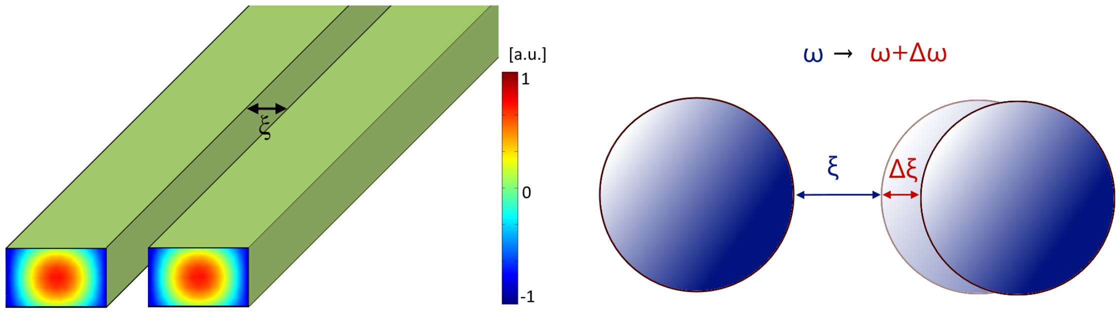

(a) (b)

Figure 2.2: Systems of coupled waveguides (a). Closed system of two coupled resonators (b).

2.1.4 Optical forces in closed system of coupled resonant cavities

Coupled resonators are another case where energetic approach is usually used to evaluate optical forces. Let's consider a closed system of two resonators separated by a degree of freedom ξ (Figure 2.2b). Let's suppose that the eigenmode of the full system with frequency ω is excited and its energy is U. An adiabatic change in the separation $\Delta\xi$ will shift the eigenfrequency by an amount $\Delta\omega$. Since the system is closed and the change in ξ is adiabatic, the total energy U is conserved, so we obtain a mechanical force on each object given by:

$$F = -\frac{dU}{d\xi}. \tag{2.23}$$

By expressing $U = N\hbar\omega$, with N the total number of photons in the resonator and $\hbar\omega$ the energy of each photon and by supposing that the photon number is unchanged by the adiabatic shift, due to the absence of absorption mechanisms,

$$F = -\frac{d(N\hbar\omega)}{d\xi} = -N\hbar\frac{d\omega}{d\xi} = -\frac{1}{\omega}\frac{d\omega}{d\xi}U. \tag{2.24}$$

2.2 Generalized Modelling of Optomechanical Forces Applied to PT-Symmetric Optical Microscale Resonators

The optical force between the two resonators obtained in the previous section is calculated through an energetic approach. However, the used hypothesis of a closed system is often not verified. In fact in order to excite an optical resonator an input waveguide is necessary, that couples the resonator with the external environment, making the system open. The approximation of optical systems as closed is often unrealistic. That's the reason why Rakich developed the Response Theory of Optical Forces (RTOF) method [45], that is an energetic approach used to evaluate optical forces, even in cases of open systems. The method by Rakich considers only systems without gain or loss. In this section a generalization of the RTOF method will be developed, including gain and loss effects. The method will be then applied to evaluate optical forces in coupled resonators of a parity-time-symmetric system. The aim is to demonstrate, that the optical forces can be enhanced by approaching the parity-time symmetry.

2.2.1 Generalized modelling of optical forces

Let's consider a reflectionless M-input, N-output system enclosed within a volume V, outside of which electromagnetic fields are negligible (Figure 2.3).

Let's consider only one mechanical degree of freedom inside the volume, which is represented by the knob q. P_i is the total power entering the system, P_o is the total power exiting the system through all the output ports. In the limit of large photon flux, we can write:

$$P_i = \sum_{m=1}^{M} \Phi_{i,m} \hbar\omega = \Phi_i \hbar\omega \tag{2.25}$$

$$P_o\left(t\right) = \sum_{n=1}^{N} \Phi_{o,n}\left(t\right) \hbar\omega'_n\left(t\right), \tag{2.26}$$

where $\hbar$ is the reduced Plank constant, $\Phi_{i,m}$ is the photon flux at the m-th input

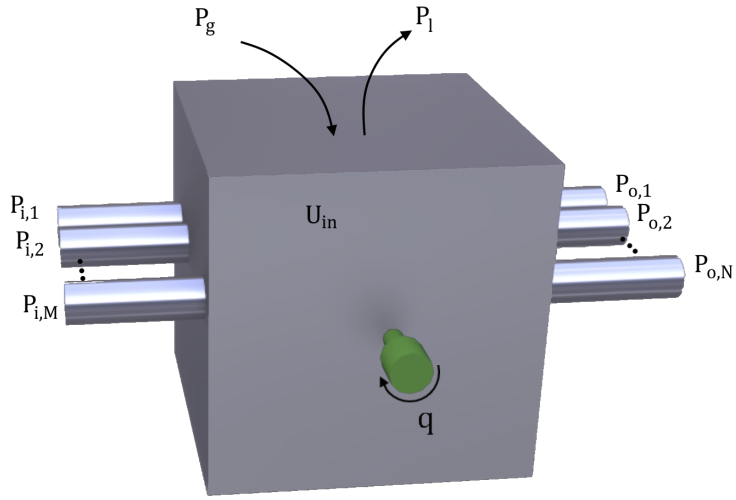

Figure 2.3: Black-box model of the optomechanical system [46].

port, ω is the photon frequency at all the input ports, $\Phi_{o,n}$ and $\omega_n'(t)$ are the photon flux and the mean frequency at the n-th output port. It should be noticed that P_i is assumed to be constant, even during dynamical evolution of the system, whereas $P_o(t)$ exhibits a dependence from time, because the motion of the degree of freedom q changes the frequency of the photons transiently stored in the optical system while modifying the capacity of the system to store energy [45]. The electromagnetic energy transiently stored in volume V can be expressed as $U_{in} = N\hbar\omega_{in}$, where N is the number of photons transiently stored at a mean frequency ω_{in}. Taking into account the lost power ($P_l = \Phi_l(t)\hbar\omega_l(t)$, with $\omega_l(t)$ the angular frequency of the lost photons) and the power increase due to gain ($P_g = \Phi_g(t)\hbar\omega_g(t)$, with $\omega_g(t)$ the angular frequency of the gained photons), the conservation principles of power and photon number in the volume V, in the presence of loss and gain, can be expressed as:

$$\begin{cases} P_i + P_g\left(t\right) = \frac{\partial U_{in}}{\partial t} + P_l\left(t\right) + F_{opt} \cdot \frac{dq}{dt} + P_o\left(t\right) \\ \Phi_i + \Phi_g = \sum\limits_{n=1}^{N} \Phi_{o,n}\left(t\right) + \frac{dN}{dt} + \Phi_l \end{cases}, \tag{2.27}$$

where F_{opt} is the instantaneous optical force component in the direction of the displacement of the generalized coordinate q, U_{in} is the optical energy stored in the volume V, Φ_l is the number of photons lost per second, Φ_g is the number of photons gained per second, P_g is the optical power flowing into the volume V because of gain, P_l is the optical power lost, due to optical loss. In the adiabatic hypothesis, the optical force is only a function of q. By expressing $F_{opt} \cdot dq/dt = -\partial W/\partial t$, with W the work done on the electromagnetic fields through the displacement of q, the system of equations 2.27 gives:

$$\sum_{n=1}^{N} \Phi_{o,n}(t)\,\hbar\omega_n'(t) - \Phi_i\hbar\omega + \frac{d\left[N(t)\,\hbar\omega_{in}(t)\right]}{dt} - \Phi_g\hbar\omega_g + \Phi_l\hbar\omega_l = \frac{\partial W}{\partial t}. \qquad (2.28)$$

By expressing $\omega_n'(t) = \omega + \Delta\omega_n'(t)$, $\omega_g(t) = \omega + \Delta\omega_g(t)$ and $\omega_l(t) = \omega + \Delta\omega_l(t)$, and recalling the second equation in the system of equations 2.27, we can write, after a few algebraic steps:

$$\begin{aligned} &\sum_{n=1}^{N} \Phi_{o,n}(t)\,\hbar\Delta\omega_n^{'}(t) \quad + \tfrac{d[N(t)\hbar\omega_{in}(t)]}{dt} + \\ &-\Phi_g\hbar\Delta\omega_g(t) + \Phi_l\hbar\Delta\omega_l(t) - \tfrac{dN}{dt}\hbar\omega = \tfrac{dW}{dt}. \end{aligned} \qquad (2.29)$$

To simplify the notation, we will include the loss and gain terms in the summation in the following way:

$$\sum_{n=1}^{N+2} \Phi_{o,n}(t)\,\hbar\Delta\omega_n^{'}(t) \quad = \sum_{n=1}^{N} \Phi_{o,n}(t)\,\hbar\Delta\omega_n^{'}(t) - \Phi_g\hbar\Delta\omega_g(t) + \Phi_l\hbar\Delta\omega_l(t)\,, \qquad (2.30)$$

with $\Phi_{o,N+1} = \Phi_l$, $\Delta\omega_{N+1}'(t) = \Delta\omega_l(t)$ and $\Phi_{o,N+2} - \Phi_g, \Delta\omega_{N+2}'(t) = \Delta\omega_g(t)$. Such a result can be interpreted as a generalization of the loss and gain photon fluxes as optical ports, with the convention that the flux of photons due to gain are taken with the negative sign. By this way, a simplified expression can be obtained as:

$$\sum_{n=1}^{N+2} \Phi_{o,n}(t)\,\hbar\Delta\omega_n^{'}(t) \quad + \frac{d\left[N(t)\,\hbar\left(\omega_{in}(t) - \omega\right)\right]}{dt} = \frac{dW}{dt}. \qquad (2.31)$$

As in [45], we will consider the work done by a small continuous change of the spatial coordinate q, Δq, over an interval of time Δt. The coordinate q can be expressed as $q(t) = qi + f(t)\Delta q$, where $f(t)$ is defined as $f(t) = 0$ for $t \in (-\infty, 0]$, $f(t) \in [0, 1]$, for $t \in (0, \Delta t)$ and $f(t) = 1$ for $t \in [\Delta t, +\infty)$. Integrating Eq. 2.31 over a time interval $[0, \Delta t + T]$, we can find:

$$\Delta W = \int_0^{\Delta t+T} \sum_{n=1}^{N+2} \Phi_{o,n}(t)\, \hbar \Delta\omega_n^{'}(t)\; dt + \left[N(t)\, \hbar\left(\omega_{in}(t) - \omega\right)\right]_0^{\Delta t+T}, \tag{2.32}$$

with T much higher than the photon-lifetime (steady-state hypothesis). We define $\Delta\omega_n'(t) := d\psi_n/dt$. The expression of Ψ_n, representing the time-varying phase of the transmitted wave at the n-th port, is not known. However, after a time $\Delta t + T$, in the steady state hypothesis, it can be replaced by Φ_n, that is the steady-state phase at the n-th output port. Moreover, the steady-state hypothesis requires that, after a time $\Delta t + T$, $\omega_{in}(t)$ must be equal to ω. So, we obtain:

$$\Delta W = \sum_{n=1}^{N+2} \int_0^{\Delta t+T} \Phi_{o,n}(t)\, \hbar \Delta\omega_n^{'}(t)\, dt. \tag{2.33}$$

With a procedure similar to that followed in [45], by expressing the photon flux as $\Phi_{o,n}(q, t) = \Phi_{o,n}^q(q, t) + \Delta\Phi_{o,n}(t)$, with $\Delta\Phi_{o,n}(t)$ a small correction of order Δq in smallness, we can obtain:

$$\begin{aligned} \Delta W &= \sum_{n=1}^{N+2} \int_0^{\Delta t+T} \left[\Phi_{o,n}^q + \Delta\Phi_{o,n}(t)\right] \hbar\Delta\omega_n'(t)\, dt = \\ &= \sum_{n=1}^{N+2} \int_0^{\Delta t+T} \Phi_{o,n}^q \hbar\Delta\omega_n'(t)\, dt + \sum_{n=1}^{N+2} \int_0^{\Delta t+T} \Delta\Phi_{o,n}(t)\, \hbar\Delta\omega_n'(t)\, dt, \end{aligned} \tag{2.34}$$

and considering that also $\Delta\omega_n'(t)$ is of the order of Δq [45]:

$$\Delta W = \sum_{n=1}^{N+2} \Phi_{o,n}^q(q)\, \hbar\left(\phi_{n,f} - \phi_{n,i}\right) + k\Delta q^2, \tag{2.35}$$

with k a constant independent from q. Dividing both terms by Δq and taking the limit as $\Delta q \to 0$, we can derive the expression of the force:

$$F = \lim_{\Delta \mathrm{q}\to 0} -\frac{\Delta W}{\Delta q} = -\sum_{n=1}^{N+2} \Phi_{o,n}^q(q)\, \hbar \frac{d\phi_n}{dq}. \tag{2.36}$$

Then, the final expression for the evaluation of the force (in the adiabatic hypothesis) is:

$$F = -\hbar \sum_{n=1}^{N+2} \Phi_{o,n}^{q} \frac{d\phi_n}{dq}, \tag{2.37}$$

with $\Phi_{o,N+1} = \Phi_l$, $\Delta\omega'_{N+1}(t) = \Delta\omega_l(t)$ and $\Phi_{o,N+2} = -\Phi_g$,$\Delta\omega'_{N+2}(t) = \Delta\omega_g(t)$.

2.2.2 Optomechanical forces in coupled resonant cavities

We have obtained an easy generalized way to evaluate optical forces, simply using the information about the amplitude and the phase of the light at the output ports. The idea of this paragraph is to use the concept of parity-time symmetry to enhance optical forces. A common way to enhance optical forces is the use of resonant cavities with a high quality-factor. In this paragraph we evaluate the influence of the PT symmetry condition in optical forces between coupled cavities, using the generalized RTOF method, taking into account all the sources of loss or gain. So, let's consider two coupled resonant cavities as in Figure 2.4.

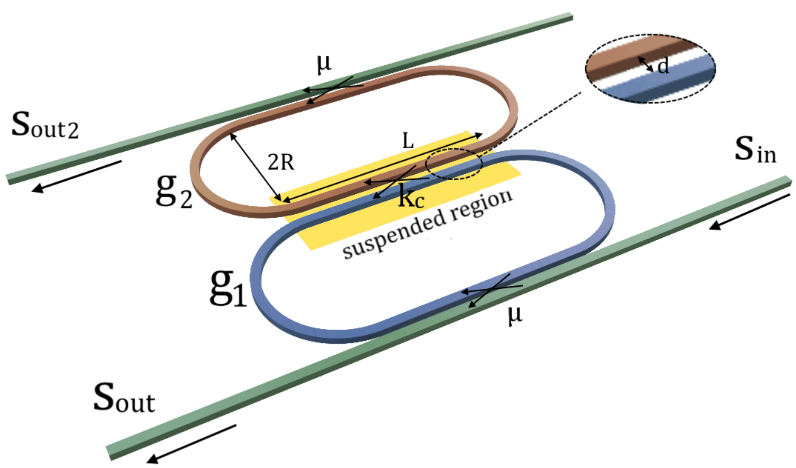

Figure 2.4: General scheme of the racetrack coupled cavities under analysis [46].

As noticeable in [30], attractive and repulsive optical forces between two optical resonators correspond to a symmetric and an antisymmetric optical resonance, respectively. So, in order to excite attractive and repulsive optical forces, we will keep the system away from the exceptional point condition. The equations describing these two coupled resonant cavities [82] are:

$$\frac{d}{dt}a_1 = j\omega_0 a_1 + \gamma_1 a_1 - jk_c a_2 - j\mu s_{in}, \tag{2.38}$$

$$\frac{d}{dt}a_2 = j\omega_0 a_2 + \gamma_2 a_2 - jk_c a_1, \tag{2.39}$$

with the usual notation: a_1 and a_2 are the energy amplitudes in the first and second cavities, respectively (they are normalized such that $|a_{1/2}|2$ is equal to the total energy stored in the first/second cavity); s_{in} represents the amplitude of the electromagnetic field travelling in the input bus (it is normalized so that $|s_{in}|^2$ is equal to the total power evaluated at any cross-section); ω_0 is the resonant angular frequency of each uncoupled cavity, μ is the mutual coupling coefficient between each cavity and the adjacent bus, k_c represents the coupling strength between the resonators [12]. The coefficient $\gamma_{1,2}$ represents the gain (or loss if negative) of the first/second cavity. It should be considered that $\gamma_{1,2}$ could be expressed as:

$$\gamma_{1,2} = -\left(\frac{1}{\tau_k} + \frac{1}{\tau_e} + \frac{1}{\tau_s}\right) + \gamma_{n1,2}, \tag{2.40}$$

where $1/(\tau_\kappa)$ represents the photon decay rate due to the coupling between the cavities ($\tau_\kappa = 2v_g/(2\pi R k_c^2)$); $1/\tau_e$ is the photon decay rate due to the coupling between the racetracks and the external buses ($\tau_e = 2/\mu^2$); $1/\tau_s$ is the photon decay rate related to other sources of loss, as the sidewall roughness scattering; γ_{n1} and γ_{n2} represent the net gain (or loss, if negative) of the first and the second cavities, respectively [12]. We should notice that only the net gains γ_{n1} and γ_{n2} contribute to the $(N+1)$-th and $(N+2)$-th terms in the expression 2.37. The other terms in 2.40 only handle the photon flux inside the control volume V. To evaluate the optical forces, we use the following relations [82]:

$$s_{out} = s_{in} - j\mu a_1, \tag{2.41}$$

$$s_{out2} = -j\mu a_2. \tag{2.42}$$

In particular, we can evaluate the optical forces between the resonant cavities by considering that the arms of the racetracks in the coupling region between the resonators are suspended. So, the spatial coordinate q is represented by the mean distance d between the edges of the suspended racetracks of resonant cavities. By considering d as an average distance, we have neglected the effect of the deflection of the arms of the racetracks on the force. From 2.37 it results that:

$$F = -\hbar \sum_{n=1}^{N+2} \Phi_{o,n}^{q} \frac{d\phi_n}{dk_c} \frac{dk_c}{dq} = -\frac{dk_c}{dq} \hbar \sum_{n=1}^{N+2} \Phi_{o,n}^{q} \frac{d\phi_n}{dk_c}, \tag{2.43}$$

with N=2, where:

$$\Phi_{o,1}^{q}(q) = |s_{out}|^2 \frac{1}{\omega\hbar}; \quad \phi_1 = \angle \frac{s_{out}}{s_{in}} \tag{2.44}$$

$$\Phi_{o,2}^{q}(q) = |s_{out2}|^2 \frac{1}{\omega\hbar}; \quad \phi_2 = \angle \frac{s_{out2}}{s_{in}} \tag{2.45}$$

$$\Phi_{o,3}^{q}(q) = -2\gamma_{n2}|a_2|^2 \frac{1}{\omega\hbar}; \quad \phi_{g2} = \angle a_2 \tag{2.46}$$

$$\Phi_{o,4}^{q}(q) = -2\gamma_{n1}|a_1|^2 \frac{1}{\omega\hbar}; \quad \phi_{g1} = \angle a_1, \tag{2.47}$$

where the symbol "$\angle$" represents the phase angle of its argument. Evaluating the relevant forces through a numerical method provides an efficient way to design an optimized resonant optomechanical device.

2.2.3 Numerical results

In the previous, we derived the analytical expression for the evaluation of the force between two suspended arms of coupled racetrack resonators, in the presence of gain and loss (Figure 2.4). In order to demonstrate the application of the shown modelling, the aim of this section is to find the behaviour of attractive and repulsive forces between the suspended arms, through parametric analysis (using Eq. 2.43). In addition, we will show the condition for which the system exhibits an equilibrium point with zero force, necessary for a self-adaptative behaviour similar to that shown in [32]. The theoretical modelling of the previous section and the parametric simulations of this Section can provide a good starting point for optomechanical applica-

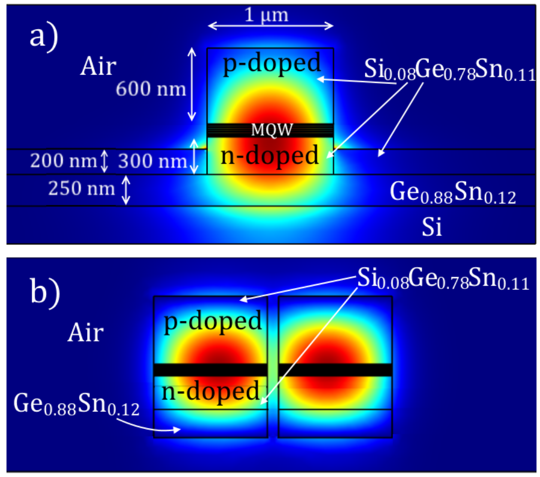

Figure 2.5: Field E_y in the cross section of the fixed part of each racetrack resonator [46] (a). Field E_y of the symmetrical mode in the cross section of the movable part of each racetrack resonator [46] (b).

tions with resonant structures, under the PT symmetry-induced force enhancement. Although the approach shown in the previous demonstration is general, we have chosen to perform our simulations using Multi-Quantum-Well SiGeSn heterostructures, excited by an external laser at 3 µm wavelength. The overall resonant system consists of two coupled resonant racetrack cavities and two external bus waveguides (Figure 2.4). One of the arms of each racetrack resonator is suspended in air, representing the movable parts of the optomechanical device. The cross-section of the non-suspended part of the racetrack is designed to be similar to that proposed in [12], using the results shown in [86]. Materials and dimensions of the structure are shown in Figure 2.5.a. Five pairs of $Ge_{0.84}Sn_{0.16}/Si_{0.09}Ge_{0.8}Sn_{0.11}$ quantum-wells (five 10 nm-$Ge_{0.84}Sn_{0.16}$ wells and six 9 nm-$Si_{0.09}Ge_{0.8}Sn_{0.11}$ barriers) can realize the gain. The cross-section of the fixed part of the racetrack is shown in Figure 2.5.a. The suspended part of the system, including the suspended arms of both the resonators, has the cross-section shown in Figure 2.5.b.

As a first step we designed the coupling strength k_c between the racetracks. The dimensionless power coupling factor K_{rr} between the two rings has been calculated as $K_{rr} = sin^2(\Delta\beta dL/2)$ [105] (with $\Delta\beta$ the difference between the propagation constant of the symmetric and antisymmetric modes and L the straight part of the racetrack)

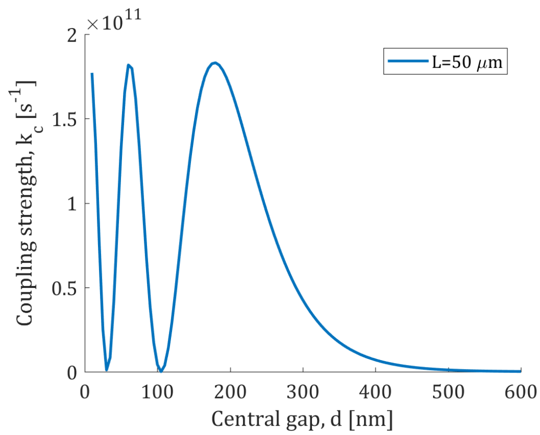

Figure 2.6: Coupling strength k_c as a function of the gap d between the edges of the suspended part of the racetracks [46].

and then k_c has been evaluated as $k_c = K_{rr} vg/L_{tot}$ [82], where L_{tot} is the total length of each racetrack.

The value of k_c as a function of the distance d is shown in Figure 2.6, for a value of $L = 50$ μm, $R = 50$ μm. As known, the coupling strength is not a monotone function of the distance d. So, recalling Eq. 2.43, for a chosen wavelength, the sign of the optical force will depend on the distance d. This could lead to the possibility of realizing a self-positioning optical device, exploiting the presence of a potential well as in [32]. From Figure 2.7 it is possible to appreciate that when the system approaches the PT symmetry condition, the peak of the spectral response $S_{out}/S_{in} = |s_{out}|^2/|s_{in}|^2$ increases. In perfect PT-symmetric condition, optical forces would be theoretically infinite (see Eq. 2.43). However, since the PT symmetry represents an ideal condition that cannot be perfectly met (due to non-linearities and technological limitations) [74], we have analysed the effect of an average loss $\Delta PT = -(\gamma_1 + \gamma_2)/2$, that takes into account that system cannot be perfectly at the PT symmetry condition ((γ_1+γ_2)=0). Figure 2.7 shows the difference between the output spectrum and the optical force in a lossy case (with propagation losses equal to 2 dB/cm). It is evident that the approaching PT symmetry allows the force per input power to be increased from less than 10 pN/mW to more than 300 pN/mW, for $\Delta PT = 26.4$ Grad/s. In order to show the effect of approaching the PT symmetry condition, the peak of the optical forces as a function of ΔPT for different

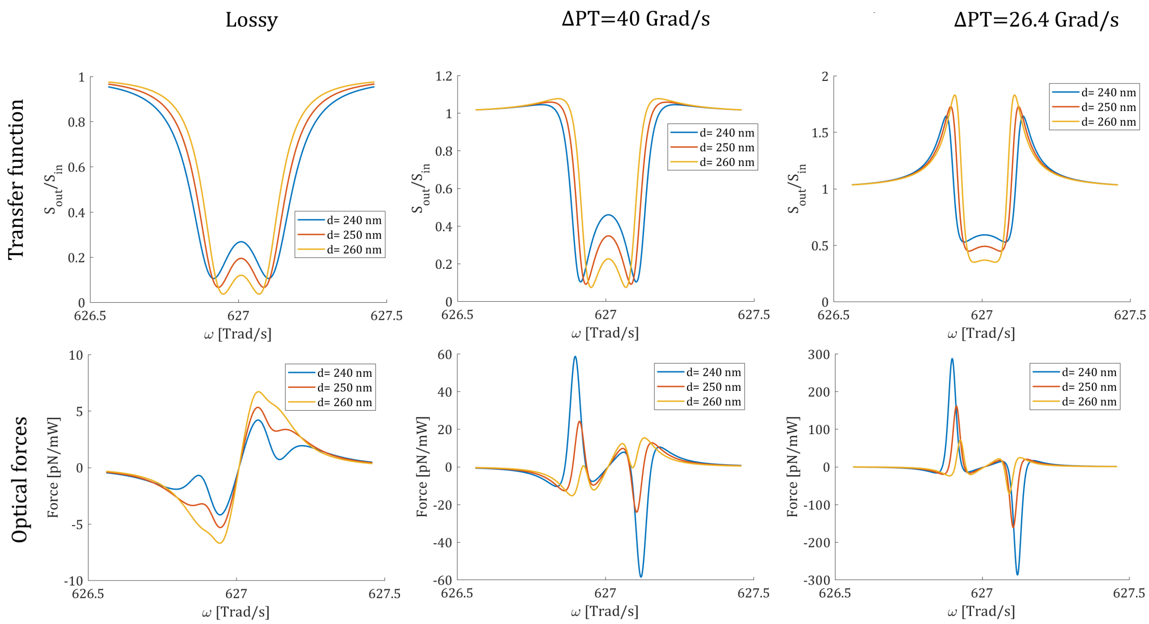

Figure 2.7: Transfer function and optical forces (normalized to the input optical power) as a function of the angular frequency for different gap d between the straight arms of the racetracks, in case of lossy resonators (left) and in case of ΔPT equal to 40 Grad/s (center) and 26.4 Grad/s (right) ($\gamma_1 - \gamma_2$ equal to 2 Grad/s). Approaching the Parity-Time condition, the forces change their sign with respect to the lossy case [46].

values of distance d is plotted in 2.8. While changing the value of ΔPT, we kept the difference $\gamma_1 - \gamma_2$ equal to 2 Grad/s. As expected, the force tends to infinity as the system approaches the PT symmetry condition. This feature is very important to enhance the effect of the force and represents an important improvement with respect to resonant systems, that have been already proposed in literature [30, 32] to enhance optical gradient forces. We have demonstrated that combining resonant optical cavities with the PT symmetry condition can increase the force of several orders of magnitude even for an input signal of the order of a few milliwatts.

In order to appreciate the trend of optical forces in quasi-PT symmetric optical cavities with respect to those obtained in lossy coupled resonant cavities, Figure 2.9 shows the color map of the optical force as a function of ω and distance d. The map has been plotted both for a condition of a lossy cavity (propagation loss equal to 2

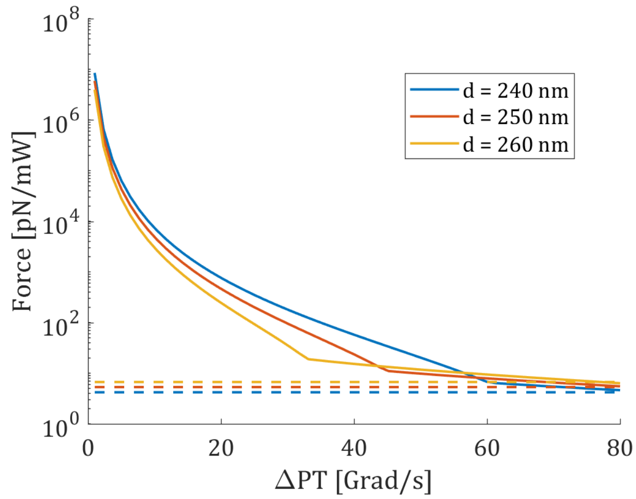

Figure 2.8: Optical maximum force as a function of the parameter ΔPT for different values of the distance d. Dashed lines represent the peak of the optical forces in the case of lossy cavities. The discontinuity in the first derivative of the function is due to the changing of the sign of the force [46].

dB/cm) and for a condition with $\Delta PT = 40$ Grad/s and $\Delta PT = 26.4$ Grad/s, with $\gamma_1 - \gamma_2 = 2$ Grad/s.

It is evident that when the system approaches PT symmetry, the optical force is significantly enhanced and its value over a distance d of 200 nm is comparable with that under 200 nm. Instead, in a lossy case the intensity of the force rapidly decays with distance d.

The enhancement of the forces due to the quasi-PT symmetry condition can be interpreted as the extension of the concept shown by Povinelli et al in [30]. Based on this concept, the optical forces between two optical resonant cavities are proportional to the quality-factor of the resonators. Large quality-factors mean large energies stored in the cavities and, consequentially, large forces. In this sense, approaching the Parity-Time Symmetry means to enhance the effect of the energy storing in the cavities, leading to larger optical forces. In fact, away from the PT symmetry condition, the imaginary part of the eigenfrequencies ($\omega_{1,2}$) is directly linked to the decay rate of the optical energy stored in the cavities ($1/\tau = Im(\omega_1) = Im(\omega_2)$, being τ the photon lifetime in the cavities) [12]. A higher photon lifetime means a higher

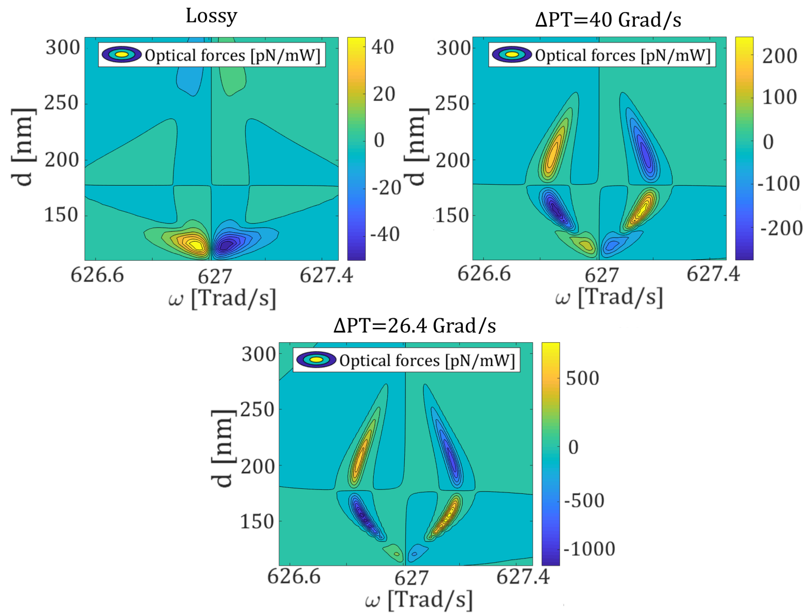

Figure 2.9: Optical forces as a function of the angular frequency for different gaps d between the straight arms of the racetracks [46].

quality-factor [82]. In this context, while approaching PT symmetry ($\Delta PT \rightarrow 0$), the imaginary part of the eigenfrequencies is reduced [12] and the enhancement of the overall quality-factor is achieved.

In Figure 2.10, the optical force as a function of the distance d is plotted at two fixed wavelengths. It is evident that in quasi-PT symmetric condition the force changes its sign for a distance lower or higher than 175 nm. This phenomenon is due to the change in sign of dk_c/dq in Eq. 2.43. The change of the sign of the force from positive to negative, for an increasing value of distance, can be interesting to be used for self-positioning optical circuits. In fact, as in [32], this condition provides a good solution for all-optical self-adaptative behaviour and cavity-trapping. As for the experimental side, once the distance between the suspended arms has been chosen and designed for the required operating point (depending on the device application), the coupling strength is fixed by the distance between the arms. Fabrication tolerances would affect the theoretical prediction, but the actual value of the coupling strength could be experimentally evaluated. Once the losses of the racetrack resonators have been characterized in a passive configuration, the carrier

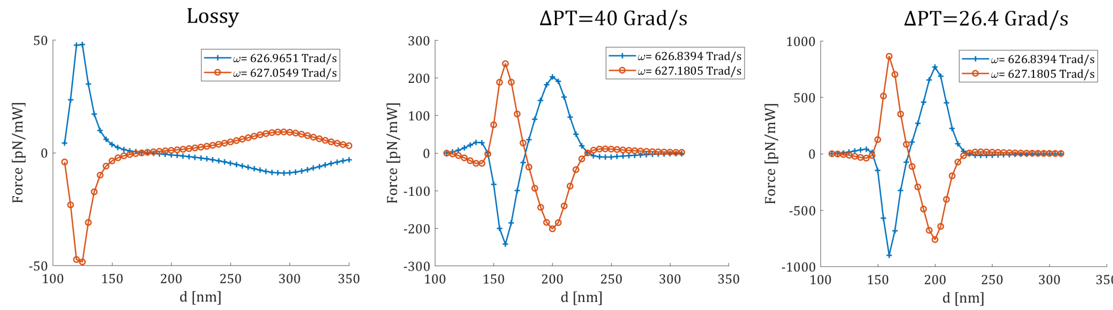

Figure 2.10: Optical forces as a function of the gap d between the internal arms of the racetracks for two different wavelengths. Optical forces have been evaluated for ω=626.9561 Trad/s and ω=627.0549 Trad/s in the lossy case and for ω=626.8394 Trad/s and ω=627.1805 Trad/s in the case of ΔPT=40 Grad/s and ΔPT=26.4 Grad/s [46].

injection in the MQW structure shown in Figure 2.5 can be used to control the gain in each resonator to reach the required value of γ_1 and γ_2 [86].

2.2.4 Final considerations

In this section a generalized RTOF method has been demonstrated. It can calculate optical forces in open systems, using only information about the amplitude and the phase of optical signals at the output ports. The model can be used for generic open systems where applying Maxwell Stress Tensor can be computationally too expensive.

The model has then been used to model the optical forces between two suspended waveguides of two coupled resonators approaching the parity-time symmetry condition. It has been demonstrated that the optical forces can be enhanced of several orders of magnitude, with this configuration.

2.3 Dynamics of optomechanically coupled suspended silicon waveguides

In the previous section a generalized model of the RTOF method by Rakich has been shown. In this section the dynamical behaviour of one of the simplest optomechanical component will be developed. In particular, after an analytical modelling of the elastic response of the waveguides and of the different sources of damping, a numerical algorithm able to predict the time evolution of the motion of the suspended waveguides will be shown.

2.3.1 Analytical modelling

The device we want to model is shown in Fig. 2.11. By exciting a symmetric supermode into the structure, it is possible to exert an attractive force between the waveguides; conversely, an antisymmetric supermode would excite a repulsive force [35]. The static behaviour of two suspended beams has been widely solved by using the Euler-Bernoulli equation. However, the dynamic behaviour in transient phase of suspended waveguide-based optomechanical devices has not been completely modelled.

In order to evaluate the dynamics of the optomechanical device, we will need to estimate :

- the optical gradient forces between the silicon waveguides;
- the elastic response of the silicon waveguides, thus treated as deformable objects;
- the different sources of energy damping emerging during motion.

In the following paragraphs, we will try to give a model for the dynamic response of the structure. We know that a precise estimation would need a numerical simulation (including CFD analysis for fluid domain and/or fluid-structure interaction analysis), however the objective of this study is to give a general idea of the main parameters involved in the system and indicate some basic design rules of an optomechanical actuator based upon the previously described configuration.

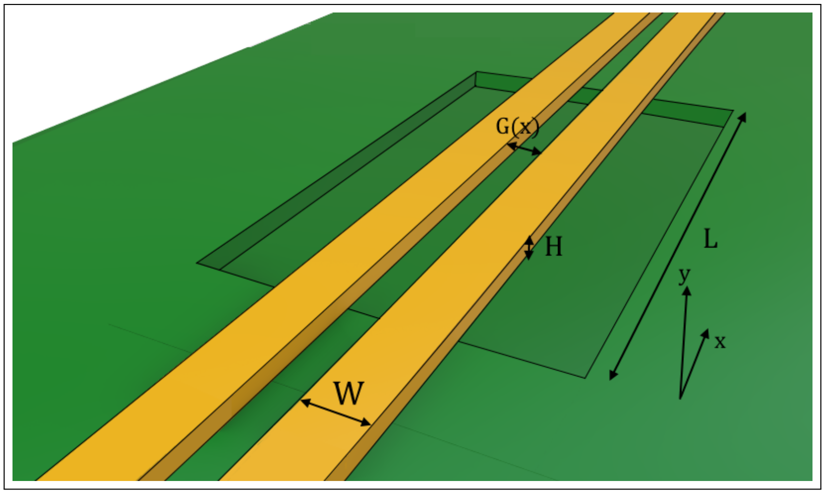

Figure 2.11: Structure of the optomechanical device [47].

2.3.2 Elastic response

The silicon waveguides can be considered as Bernoulli beams (the main hypothesis is that all cross-sections remain persistently straight and perpendicular to the neutral axis when deformation occurs). For the evaluation of the dynamics of the optomechanical device, we chose to use a Finite Element Method (FEM) modelling. After 1-D spatial discretization of each waveguide, the behaviour of the deformable waveguides, thus treated as a series of connected flexural beam elements, can be described by the general expression (in dynamic regime):

$$-[M]\ddot{\mathbf{f}} - [C]\dot{\mathbf{f}} - [K]\mathbf{f} + \mathbf{F_e} = 0, \tag{2.48}$$

where $[M]$ is the lumped mass matrix, $[C]$ is the lumped damping matrix, $[K]$ is the stiffness matrix and $\mathbf{F_e}$ is the array of the generalized external forces (both forces and momenta) applied to each node of the beam, while $\mathbf{f}$ represents the array of the generalized displacements (both translations and rotations) [106].

2.3.3 Optical forces

The optical gradient forces acting between the two suspended waveguides, due to a symmetric supermode, could be calculated through the well-known equation [107]:

$$F_{opt} = -\frac{P}{c_0}\frac{dn_{eff}}{dG(x)}L, \tag{2.49}$$

where P is the input power of the symmetric supermode, c_0 is the speed of light in vacuum, n_{eff} is the effective index of the optical symmetric supermode propagating in the deformable region, L is the length of the deformable region of the waveguides and $G(x)$ is the gap between the waveguides at the generic position x (Fig. 2.11).

2.3.4 Damping

Damping represents one of the elements influencing the dynamics of the device. In order to estimate it, we neglected any form of internal material damping (e.g. viscoelasticity). We considered the air drag and the air squeezing effect between facing surfaces of the coupled waveguides as the contributions to the total damping.

Knudsen correction for viscosity

In order to evaluate the damping due to the air surrounding nano-scaled objects such as the two deformable waveguides, it is necessary to evaluate the Knudsen number to verify whether the fluid could be still considered as a continuum:

$$K_n = \frac{\bar{\lambda}}{d}, \tag{2.50}$$

where $\bar{\lambda}$ represents the free mean path of air molecules and d is a characteristic dimension of the structure [108]. Considering d as the hydraulic diameter for our structure ($D_H = 4GL/(2G+2L)$), it is possible to show that, for the structure in Fig 2.11 (G variable in the order of 10^2 nm and $L = 50$ μm), Knudsen number is in the range $0.01 < K_n < 1$; it means that the fluid cannot be considered as a continuum and a correction should be applied to viscosity.

In particular, as in [108], we can model the effect of rarefaction of air in a Knudsen flow as a modification of the viscosity into:

$$\mu_{eff} = \frac{\mu}{1 + f(K_n)}. \tag{2.51}$$

There are several empirical models to evaluate $f(K_n)$ in Eq. 2.51 [108]. We used the one proposed by Knudsen:

$$f(K_n) = \frac{K_n + 2.507}{K_n + 3.095} \frac{K_n}{0.1474}. \tag{2.52}$$

Because of the attraction of the suspended waveguides, a local pressure raising is induced into the gap between them (squeeze flow), so the dependence of the mean free path on pressure should be taken into account [108]:

$$\bar{\lambda}(x) = \frac{p_0}{p_{gap}(x)} \bar{\lambda}_0, \tag{2.53}$$

where p_0 is the pressure of unperturbed air, whereas $p(x)$ is the actual local pressure between the suspended waveguides. The pressure $p_{gap}(x)$ can be evaluated by averaging the relative pressure $p(x, y)$ [109] along the height H and adding the unperturbed pressure p_0:

$$p(x, y) = \frac{6\mu_{eff}}{G^3(x)} \dot{G}(x) \left[\left(\frac{H}{2} \right)^2 - y^2 \right], \tag{2.54}$$

$$p_{gap}(x) = p_0 + \frac{1}{H} \int_{-H/2}^{H/2} p(x, y)\, dy. \tag{2.55}$$

Using the set of equations above, we obtain a nonlinear implicit expression that should be solved numerically:

$$\mu_{eff} = \frac{\mu}{1 + f(K_n(\mu_{eff}))}. \tag{2.56}$$

It is not immediate to check if this iterative procedure is really necessary or if an initial approximation of the viscosity could be sufficiently accurate throughout the whole analysis.

Laminar drag

Reynolds number ($Re = \rho \bar{v} L / \mu_{eff}$, with ρ the density of the air, and $\bar{v}$ the average velocity of each suspended beam in an undamped case) has been calculated to be 1.66 (for P =10 mW), ensuring that we can consider the air flow as laminar. The air drag on a single beam moving in a fluid could be calculated starting from the generalized Stokes force [110]:

$$F_S = 3\pi\mu_{eff}\left(\frac{1}{3}d_n + \frac{2}{3}d_s\right)v, \tag{2.57}$$

where d_n is the diameter of a surface of an equivalent sphere with the same normal surface and d_s is the diameter of a surface of an equivalent sphere with the same total surface. The effect of the laminar drag can be modelled through the damping coefficient on the whole beam, considering:

$$C_{St} = 3\pi\mu_{eff}\left(\frac{1}{3}d_n + \frac{2}{3}d_s\right). \tag{2.58}$$

Squeeze-film damping

To estimate the squeeze-film damping force (F_{sq}) caused by the effect of the increasing air pressure (see Eqs. 2.54 and 2.55) in between the facing surfaces when getting closer, we used the model shown in [111]:

$$F_{sq} = \frac{\mu_{eff} H^3 l}{G^3(x)}\dot{G}(x), \tag{2.59}$$

where l is the length we are considering for the lumped parameters treatment, regarding the squeeze-film damping.

In this case the damping coefficient of each translational degree of freedom of a single waveguide could be evaluated as:

$$c_{Sq} = 2\frac{\mu_{eff} H^3 l}{G^3(x)}. \tag{2.60}$$

2.3.5 Numerical Implementation

Time discretization

We implemented Eq. 2.48 on *Matlab®* to evaluate the dynamic behaviour of the beams. We chose a central difference scheme for time discretization:

$$\dot{\mathbf{f}} = \frac{d\mathbf{f}}{dt} = \frac{\mathbf{f}(t+\Delta t) - \mathbf{f}(t-\Delta t)}{2\Delta t}, \tag{2.61}$$

$$\ddot{\mathbf{f}} = \frac{d^2\mathbf{f}}{dt^2} = \frac{\mathbf{f}(t+\Delta t/2) - \mathbf{f}(t-\Delta t/2)}{\Delta t^2}, \tag{2.62}$$

being Δt the interval for time discretization. By substituting Eqs. 2.61 and 2.62 into 2.48, it is possible to calculate displacements at every time t.

2.3.6 Damping matrix assembly

The matrix [C] can be assembled considering the contribution of the laminar drag and the squeezing effect. In particular a diagonal matrix can be built, where the elements related to the translational degrees of freedom are evaluated as a sum of c_{sq} and $c_{St} = C_{St}/n$ (with n the number of the finite elements in each deformable waveguide).

We neglected the terms related to the rotational degrees of freedom, because they are orders of magnitude lower than the ones related to the translational degrees of freedom.

The $[C]$ matrix is updated at each time step, in order to capture the dynamic evolution of the squeezing and laminar drag forces over time.

2.3.7 Algorithm implementation

Algorithm 1 shows the entire procedure to evaluate the displacements of the finite elements. At each time step, the external forces $\mathbf{F_e}(t)$ and the damping coefficients are evaluated in order to extrapolate the displacements at the next time step. The cycle is repeated until the stop condition is satisfied.

Algorithm 1 Numeric algorithm for the evaluation of the displacement.

procedure DISPLACEMENT($\mathbf{F_e}, \mu_{eff}, [C]$)
  $t \leftarrow 0$
  while $|\ddot{f}(t)| > \epsilon_1$ or $|\dot{f}(t)| > \epsilon_2$ **do** ▷ Stop condition (with ϵ_1 and ϵ_2 residual errors on acceleration and speed)
    Evaluate $\mathbf{F_e}(t)$ (Eq. 2.49)
    Evaluate $\mu_{eff}(t)$ (Eq. 2.56)
    Update $[C]$ matrix (Eqs. 2.58 and 2.60)
    Evaluate $\mathbf{f}(t + \Delta t)$ (Eqs.2.61 and 2.62 in Eq. 2.48)
    $t \leftarrow t + \Delta t$
  return $\mathbf{f}(t)$

2.3.8 Numerical results

In this section the main results of the simulation (performed for a temperature of 300 K) are shown. As a first step the optical force between the suspended waveguides has been calculated as a function of the gap between them, through the Eq. 2.49: the effective index of the symmetric supermode has been calculated for different values of the initial gap G_0 and the force per unit power and unit length has been calculated for a cross-section with $H = 220$ nm and $W = 310$ nm (Fig. 2.12). The effective index has been numerically calculated under the hypothesis of translational invariance using the commercial software *COMSOL Multiphysics®*. In particular, with a maximum grid spacing of 10 nm over a total computational domain of 3100 nm x 2200 nm, a relative error lower than $2 \cdot 10^{-7}$ was obtained.

Figure 2.13 shows the effective mode index of the symmetric supermode and the related optical force for an initial gap G_0 ranging from 50 nm (reasonably achievable with e-beam lithography) to 220 nm. We chose a cross section of 220 nm x 310 nm, since it has been chosen in experimental works, guaranteeing a lower stiffness with respect to the standard 220nm x 500nm cross-section [112].

Fig. 2.14 shows the maximum displacement δ ($\delta = \frac{G_0 - G(L/2)}{2}$)of the central point of each waveguide as a function of time for different values of the input power (with $L = 50$ μm and $G_0 = 100$ nm). For 10 mW of input power, the final displacement is around 18 nm, decreasing for lower values of input power. The maximum δ is 27.5 nm for 10 mW of input power. It means that the maximum range of $G(x)$ is from

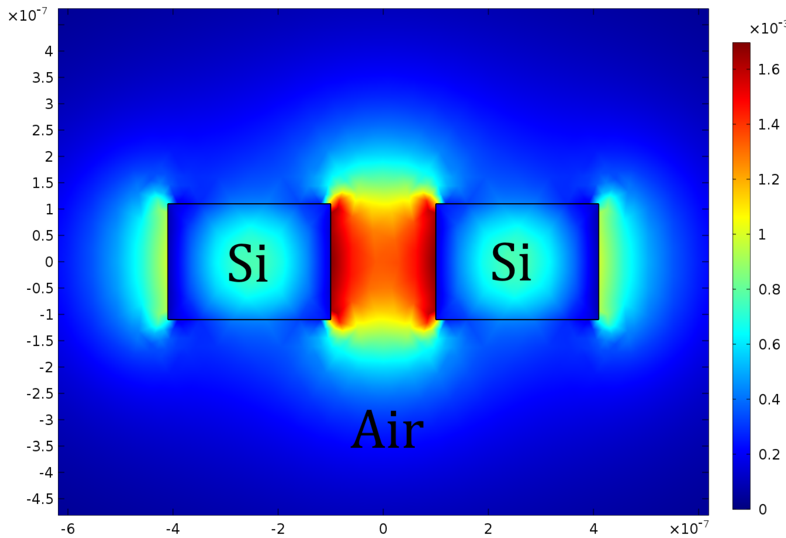

Figure 2.12: Squared norm of electric field of the symmetric mode in the coupled waveguides [47].

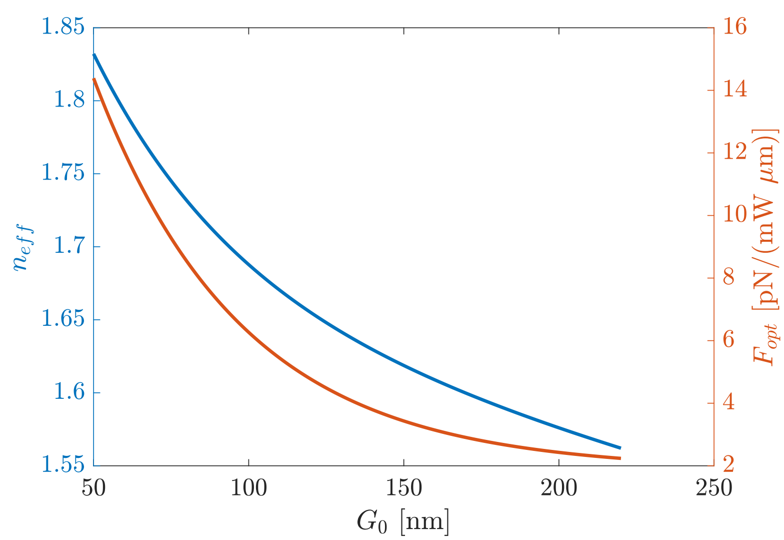

Figure 2.13: Effective index of the symmetric supermode (left y-axis) and optical attractive force (right y-axis) as a function of the initial gap G_0 [47].

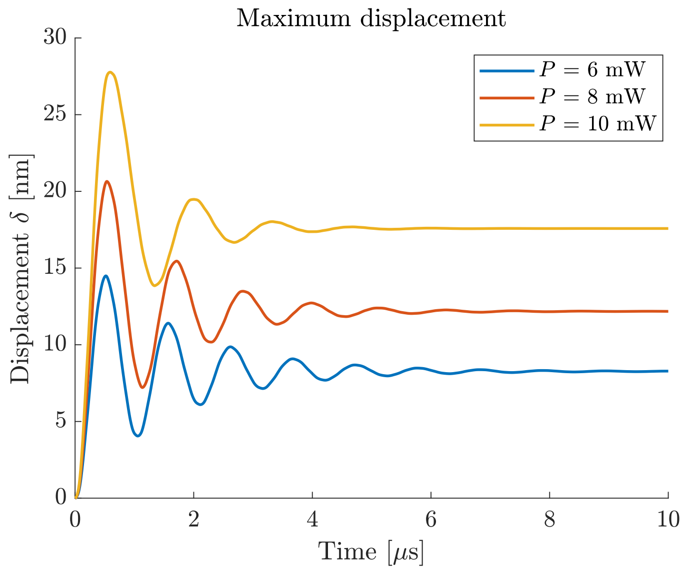

Figure 2.14: Maximum displacement as a function of time, for three different values of input power [47].

100 nm to 45 nm during the transient phase of motion. The dynamic response is underdamped in all of the cases and the settling time is of the order of microseconds. For low input powers, the forces and the maximum displacements decrease and so the damping; the latter is justified by the dependence of μ_{eff} on the velocities $\dot{\mathbf{f}}(t)$ and the dependence of the squeezing effect on the cube of the distance $G(x)$. This is the reason why for higher values of input power the system settles in a lower time.

It is not easy to compare these results to the ones experimentally obtained in literature, because, to our knowledge, in those works only one of the waveguides is excited, leading to a resulting beating mode (superposition of a symmetric and antisymmetric supermodes). This brings to a totally different behaviour of the optical forces [113].

In Figure 2.15, the time evolution of μ_{eff} (with $L = 50$ μm and $G_0 = 100$ nm and different values of input power) is shown. Such a result could be used to estimate the error that the model would imply, by considering the initial effective viscosity as a constant value for the entire analysis. In the presented cases, a maximum relative error of around 29% over the effective viscosity would have been accepted, if the initial viscosity had been used for the entire analysis.

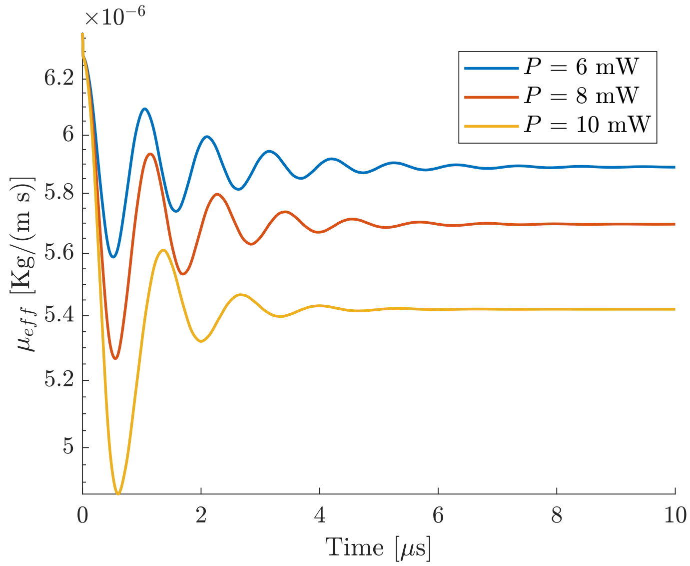

Figure 2.15: The value of μ_{eff} as a function of time, during the settling of the silicon waveguides [47].

In Figure 2.16, the time evolution of the damping coefficients is shown. The laminar drag is always lower than the squeezing effect, that results to be the dominant contribution, during all the settling phases.

Fig. 2.17 shows the settling time as a function of the initial gap G_0 (with L = 50 μm). It can be seen that the lower the initial gap, the lower the settling time. This could be interpreted as a result of the squeezing damping force, that is proportional to $G^{-3}(x)$. By increasing the damping, the system moves from a condition of underdamping to the condition of critical damping (corresponding to the minimum settling time).

Fig. 2.18 shows the settling time as a function of a correction factor (C_F) multiplying the overall damping coefficient formulated in the previous sections (with $L =$ 50 μm and $G_0 = 100$ nm and different values of input power). The settling time has been considered as the time necessary for the displacement of the central point (δ) to enter in an error range included between $+10\%$ and -10% of the regime value. The minimum settling time is reached for a damping correction factor C_F of 3.9 (corresponding to the condition of critical damping), evaluated for an input power of 10 mW.

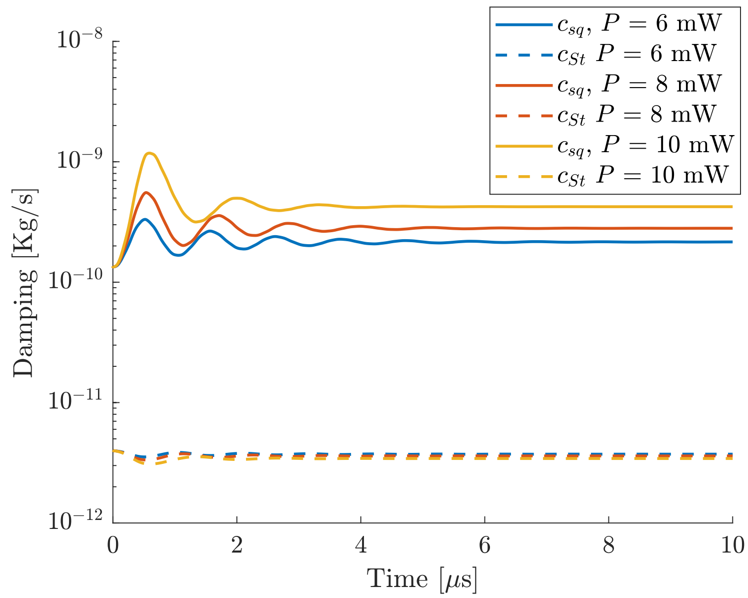

Figure 2.16: Damping coefficients (due to laminar drag and squeezing effect): time evolution.

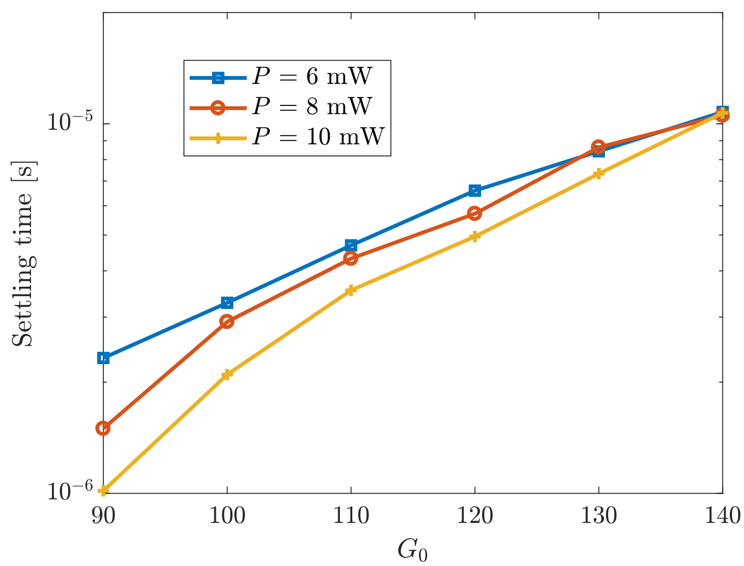

Figure 2.17: Settling time t_s as a function of initial gap G_0.

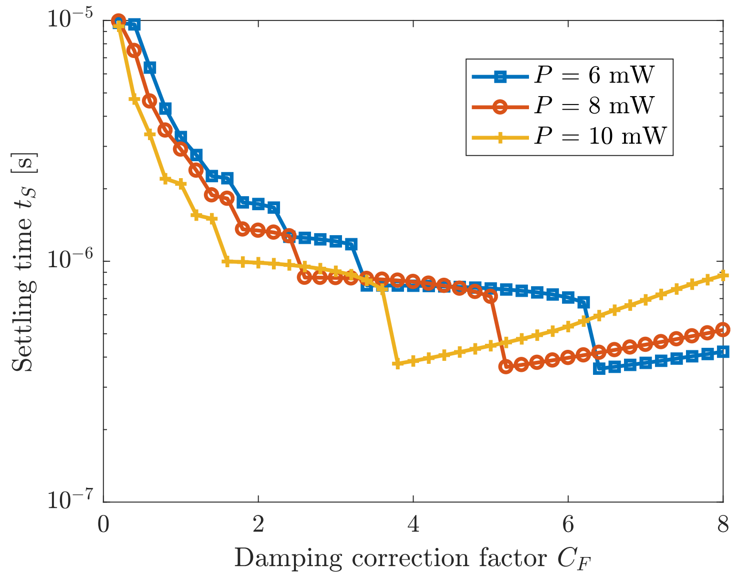

Figure 2.18: Settling time t_s as a function of the damping coefficient [47].

2.3.9 Final consideration

An algorithm to evaluate the dynamic mechanical response of a deformable suspended waveguide-based optomechanical device has been presented. It has been demonstrated that the settling time of the proposed configuration is of the order of microseconds. Acting on damping, the minimum achievable value of the settling time would be of the order of hundreds of nanoseconds. Moreover, we demonstrated that the settling time of the device is influenced by the input power of light, because the higher the power, the more the damping due to the squeezing effect.

2.4 Optomechanical switch

In this final section of the chapter, an experimental work about an optomechanical switch will be shown. The work has been performed at the Optoelectronics Research Centre of the University Southampton. The idea of this work is to show the possibility of controlling the light behaviour through the exploitation of optical forces.

2.4.1 Idea of an optomechanical switch

The central idea is to create an optomechanical switch. By setting up a directional coupler with two suspended waveguides and by applying an optical force between the two suspended arms it is possible to change the distance between the suspended waveguides and, consequently, the fraction of the power of a signal input coupled from one arm to the other one of the directional coupler. When a signal of power (P_0) is injected in one waveguide of a directional coupler, the fraction of power coupled from the first to the second waveguide of the coupler will be given by the formula [114]:

$$P_c = P_0 \sin^2\left(\frac{\pi L \Delta n_s}{\lambda}\right), \tag{2.63}$$

with Δn_s the difference between the effective indices of the even and the odd supermodes, L the length of the coupler and λ the wavelength of the signal. The term Δn_s is function of the distance between the optical waveguides. So, by tuning that distance using optical forces, it is possible to redirect light to one output or the other.

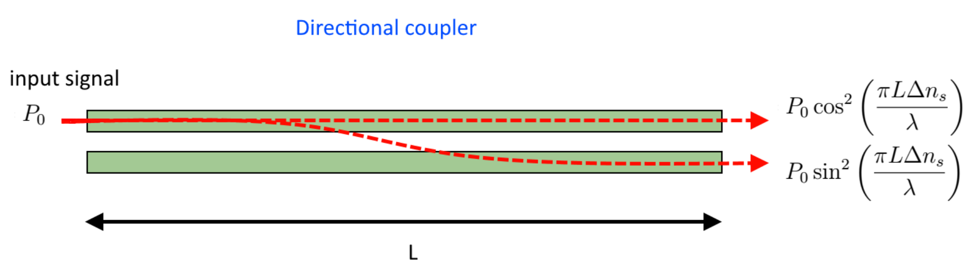

Figure 2.19: Working principle of the directional coupler.

In order to exert an attractive optical force between the two suspended arms it is necessary to excite the coupled suspended waveguides with an even optical supermode (Figure 2.20), using a pump source (the pump source will be counter-propagating to avoid interference) as in Figure 2.21. The optical force will decrease the gap between the suspended waveguides and change Δn_s. So the coupled optical force, will vary according to Eq. 2.63.

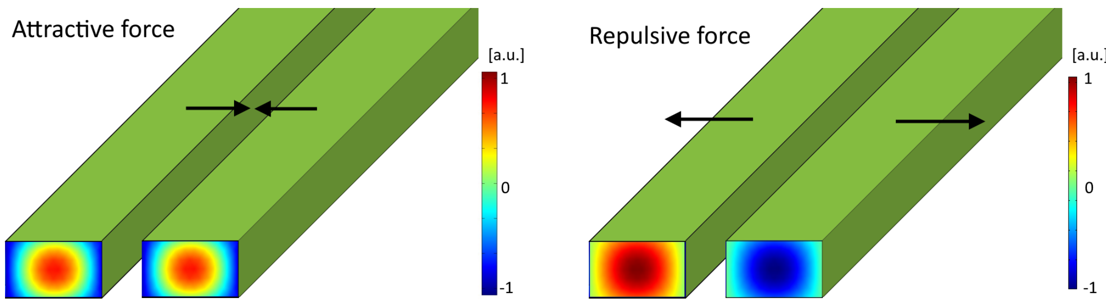

(a) (b)

Figure 2.20: Electric field of an even (a) supermode and an odd supermode (b)

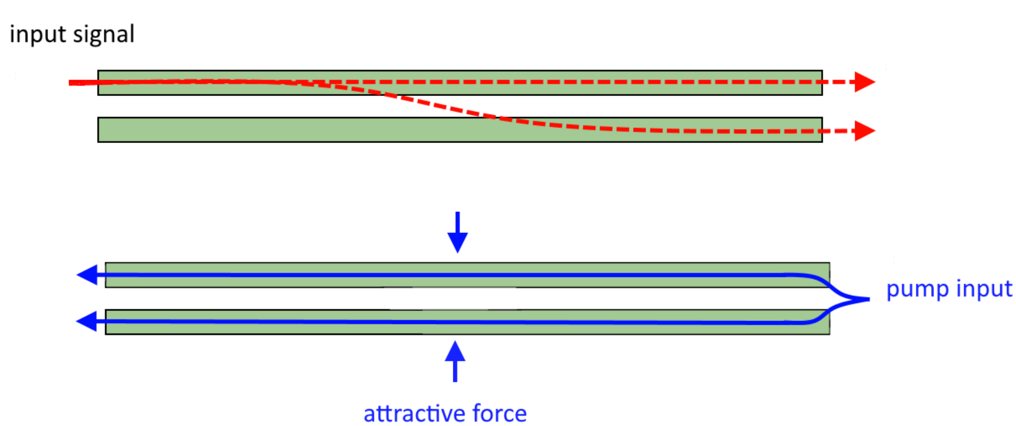

Figure 2.21: Working principle of the switch. The pump input excites an attractive force and the input signal is directed to one of the output ports.

2.4.2 Design

The complete device was designed as in Figure 2.22. The inset of Figure 2.22 corresponds to the directional coupler of Figure 2.21. In order to excite the symmetric supermode from the pump source, three MMIs (Multi Mode Interferometers) have been used, acting as power splitters. The pump input power is divided in two waveguides, thus reaching the suspended region and exciting a supermode on the suspended waveguides after two different optical paths (Figure 2.23a)(the optical path difference is $\Delta L n_{eff}$, with n_{eff} the effective index of all the waveguides and ΔL is the geometrical path difference between the two paths shown in 2.22). In this way, by controlling the wavelength of the pump input, it is possible to control the phase difference between the two pump signals reaching the suspended region in P_1 and P_2 after two different optical paths (Figure 2.23a). If the optical path difference ($\Delta L n_{eff}$) is an even multiple of the pump wavelength, a symmetric supermode will be excited in the suspended waveguides (attractive force), whereas, if the phase difference is an odd multiple of the pump wavelength, an antisymmetric supermode will be excited (repulsive force). Moreover, by controlling the power of the pump input, we can control the intensity of the optical force between the suspended waveguides,

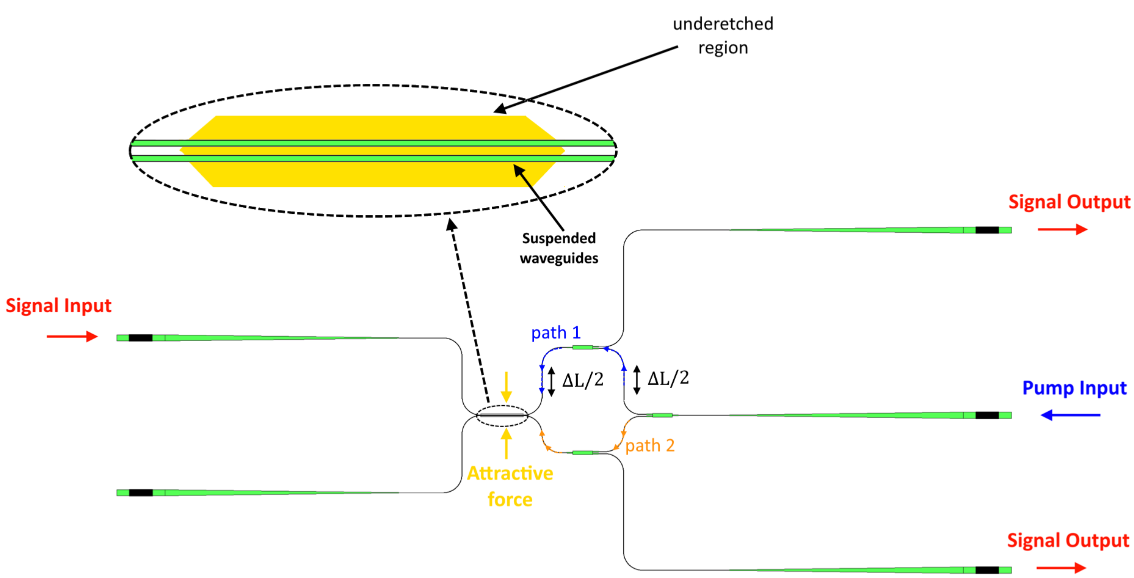

Figure 2.22: Design of the optomechanical switch

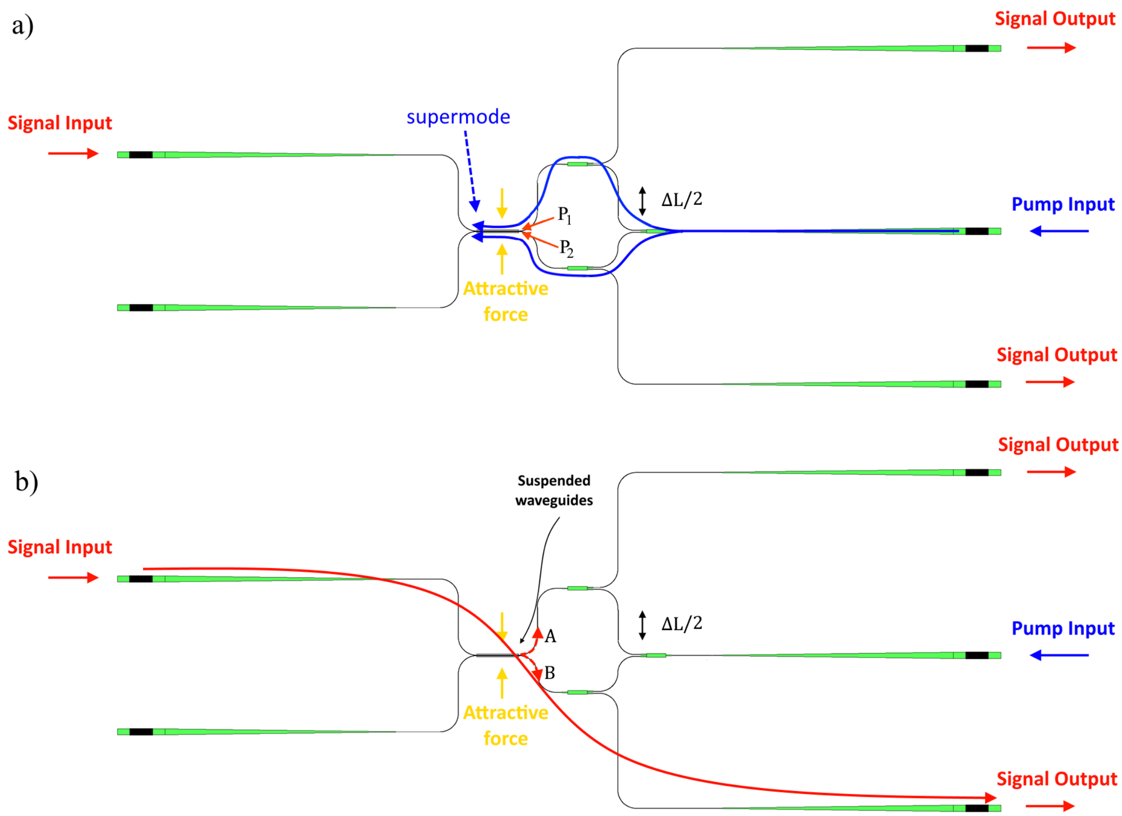

Figure 2.23: Working principle of the optomechanical switch. The pump input power in (a) is divided in two paths with an optical path difference $\Delta L n_{eff}$. Depending on the wavelength of the pump input, a symmetric or antisymmetric supermode (or a combination of both) can be excited in A and B, thus exciting optical forces. So, the input signal power coupled fraction can be controlled (b).

thus adjusting the input signal power coupled fraction (Figure 2.23b), according to Eq. 2.63. The power of the pump is supposed to be much higher than the signal.

Two different designs have been tried to fabricate the device, because the process of underetching the suspended region is crucial and was not completely standardized in the facilities of the Optoelectronics Research Centre. In particular a design with strip waveguides and one with rib waveguides have been tried. The waveguides have been designed to have a width of 500 nm in the strip design, and a width of 450 nm in the rib design (with a rib of 70 nm). A standard 2 μm-SiO_2/220nm-Si wafer has been used for both the designs.

2.4.3 Fabrication process - first design: strip waveguides

The first design uses strip waveguides. In order to fabricate a chip with suspended waveguides, the process has been divided into three steps:

- Waveguides etching
- Grating couplers etching
- Suspended waveguide underetching

Grating couplers are Bragg gratings useful to couple light from an external optical fibre to the chip. Due to the reciprocity of light the same grating couplers can be used to couple light from the chip to the optical fibres. In the first two steps, a wet HF etching approach has been used. Whereas, in the third step the wet HF etching would cause the suspended waveguides to get stuck during the drying process. So, a different approach has been chosen. In particular a Vapor HF etching process has been used. It needed to be characterized on some dummy chips, to know the etching rate of the process. After 30 minutes of vapor HF etching, dummy waveguides (220nm high and 500 nm wide) were completely suspended. Figure 2.28 shows the SEM image of the suspended waveguides in cross section, after a Focused Ion Beam (FIB) Milling in the dummy chip. It could be seen that the underetch was complete. The suspended waveguides are touching the SiO_2 substrate because of the electrostatic discharge

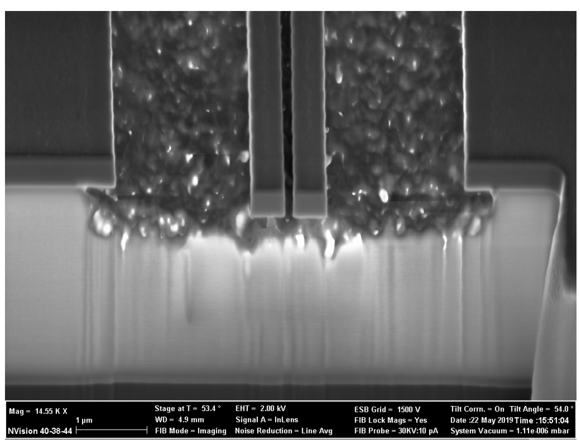

Figure 2.24: Test suspended waveguides after vapor HF

happened during the FIB milling. The complete fabrication steps are listed below. Figure 2.26 shows the process flow.

Waveguides etching

- Mask design for waveguides
- ZEP spin coating
- E-beam lithography
- ZEP Development
- Silicon etching
- Ashing (to remove the ZEP)

Grating couplers etching

- Mask design for grating couplers
- ZEP spin coating
- E-beam lithography
- ZEP Development
- Silicon etching
- Ashing (to remove the ZEP)

SiO_2 underetching

- Mask design for windows of suspended regions
- ZEP spin coating
- E-beam lithography
- ZEP Development

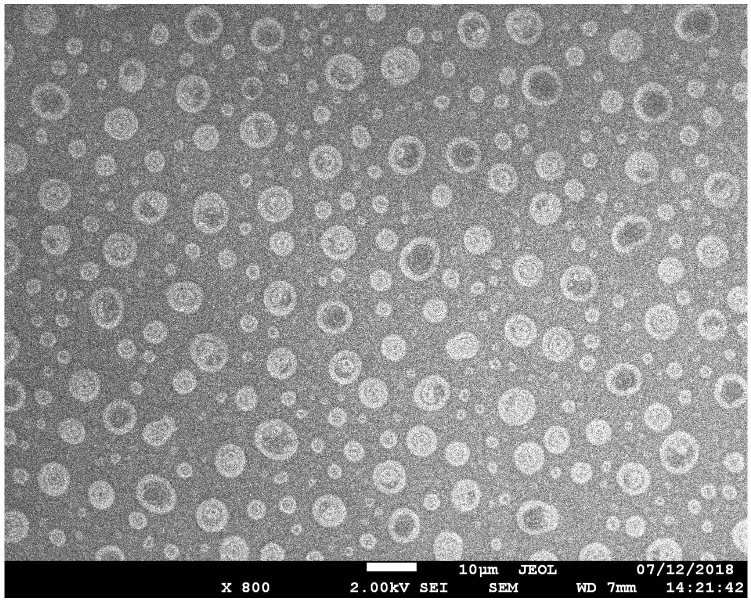

Figure 2.25: HF bubbles under ZEP after Vapor HF

- Vapor HF - Etching
- Ashing (to remove the ZEP)

The attempt of using vapor HF with a ZEP mask to underetch the waveguides has been shown to be not a good solution. In fact, some bubbles appeared on the top of ZEP after the vapor HF etching, causing vapor HF to be trapped under the ZEP mask. This solution is too dangerous for health and cannot be used for underetching.

Partial WET - HF and Vapor HF

An attempt to solve this problem has been tried. In particular the idea was to replace the Vapor HF - Etching step with a different procedure: a partial underetching of the suspended waveguides with wet etching using a ZEP mask and, then, a vapor HF etching. This solution is illustrated in the last two steps of Figure 2.26. The SEM image after the FIB milling of the suspended region after the wet HF etching and before the vapor HF etching is shown in 2.27b

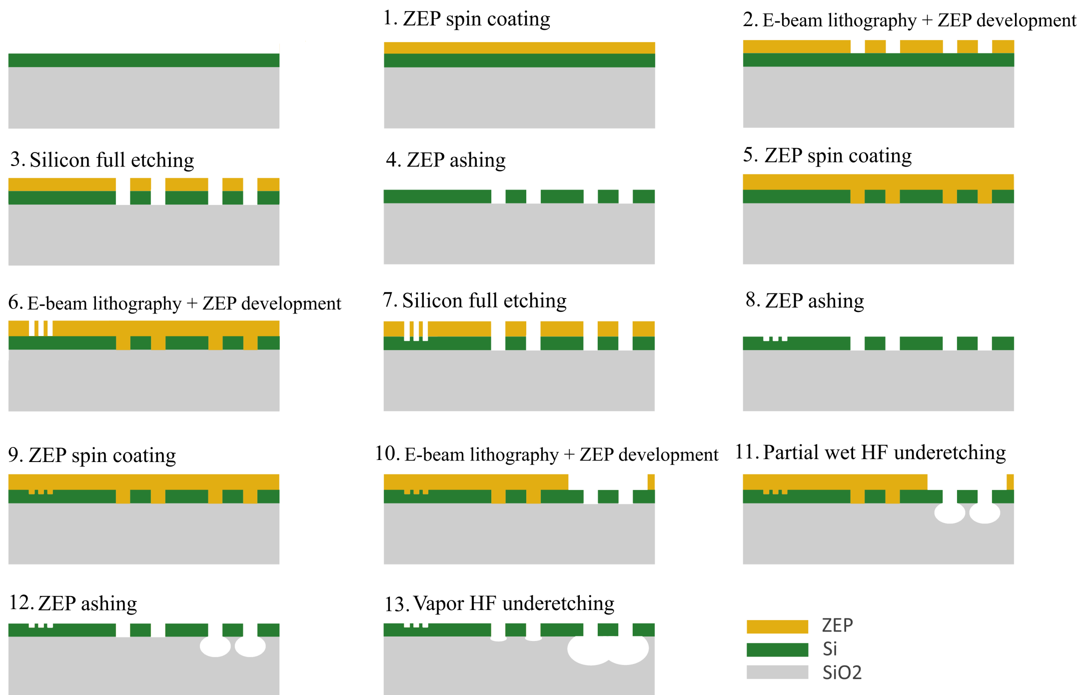

Figure 2.26: Process flow with strip design

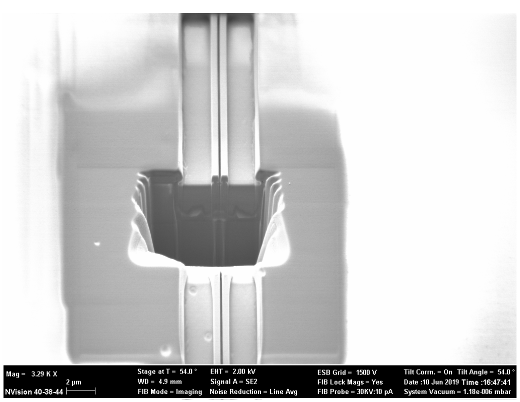

(a)

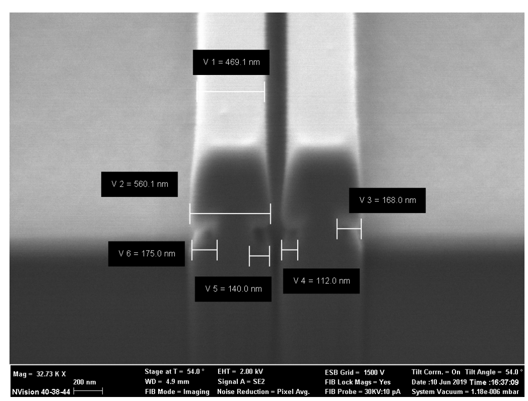

(b)

Figure 2.27: SEM pictures: cross section of suspended waveguides after wet etching (a) and zoom of the same picture with dimensions (b)

2.4.4 Fabrication process - second design: rib waveguides

In this second approach rib waveguides are used for the unsuspended waveguides. Whereas, the suspended waveguides have been designed to be strip. The idea is to use vapor HF in the last step of fabrication without the ZEP mask. The process flow is the following:

SiO_2 Hard Mask

- SiO_2 Hard Mask Deposition PECVD - 50 nm

Waveguides etching

- Waveguides Mask design
- ZEP spin coating
- E-beam lithography
- ZEP Development
- SiO_2 full etch and intermediate silicon etch (170 nm)
- Ashing (to remove the ZEP)

Windows

- Mask design for windows of suspended regions
- ZEP spin coating
- E-beam lithography
- ZEP Development
- Silicon full etching - residual
- Ashing (to remove the ZEP)

Grating couplers etching

- Grating Mask design
- ZEP spin coating
- E-beam lithography
- ZEP Development
- SiO_2 full etching and silicon - partial etching (70 nm)
- Ashing (to remove the ZEP)

Vapor HF

- Vapor HF to underetch SiO_2

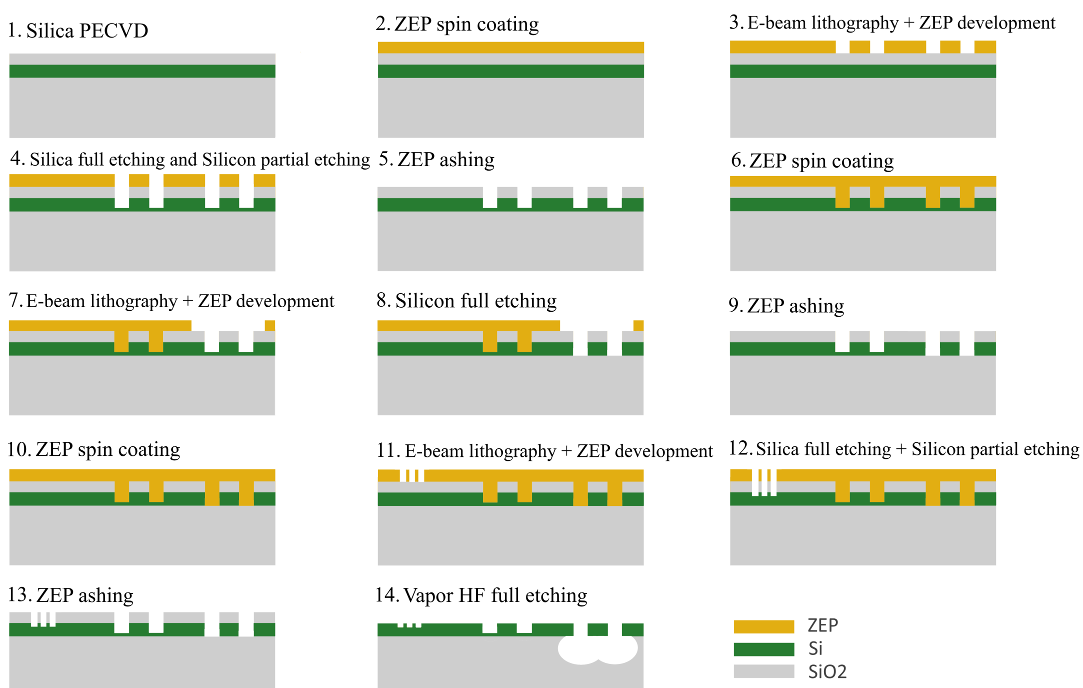

Figure 2.28: Process flow with rib design and hard mask

Figure 2.29 shows SEM pictures of the fabricated device before the last step (Vapor HF). Figure 2.30 shows microscope images of the final fabricated device with three different zooms on the suspended part.

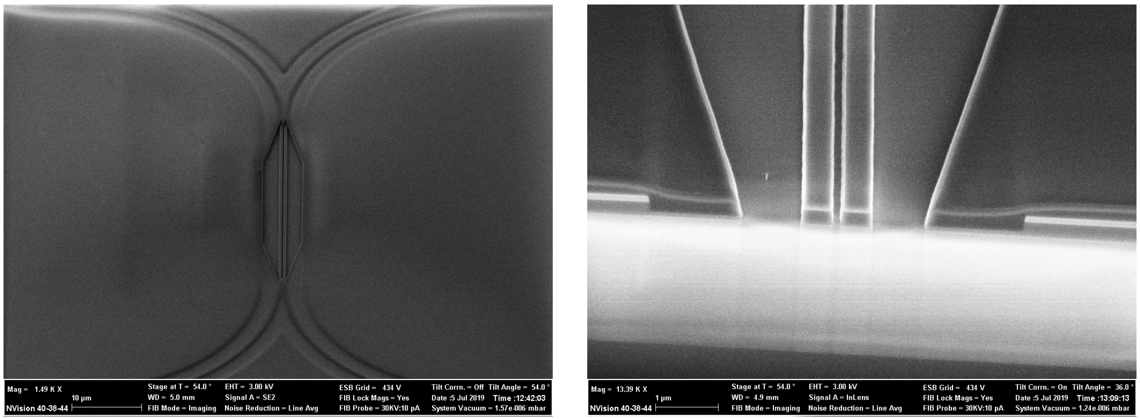

(a) (b)

Figure 2.29: SEM pictures: cross section of suspended waveguides before the last step (Vapor HF), before (a) and after (b) FIB

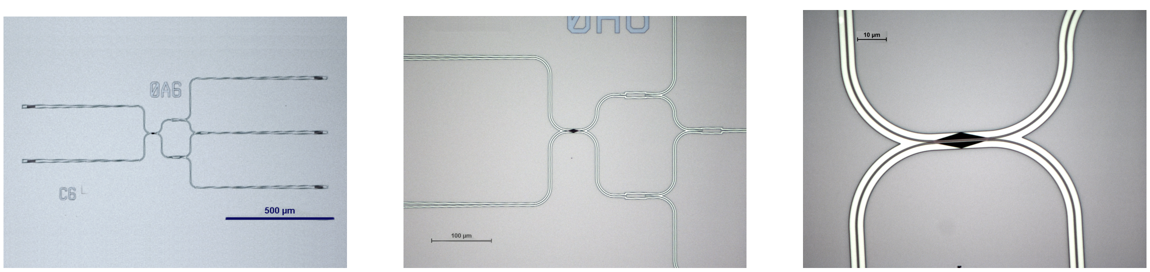

(a) (b) (c)

Figure 2.30: Microscope image of the fabricated device with three different zooms on the suspended part.

2.4.5 Experimental Results

The experimental results that will be shown in this section have been obtained on the rib design. The measurement system has been set up with the use of:

- 1 Erbium Doped Fibre Amplifier (EDFA)
- 1 Optical Circulator
- 1 Optical Isolator
- 2 Optical tunable Lasers
- 2 Optical Polarizers

The input signal, after passing through a polarizer (manually adjusted to maximize the output transfer function) goes into an isolator and then is coupled to the chip thanks to the input grating coupler. The pump signal passes through a polarized and then through an Erbium Doped Fibre Amplifier (EDFA) to reach the power of hundreds of milliwatts. Then, it goes from port 1 to port 2 of a circulator and then is injected into port 3 of the chip. In order to avoid any influence of the pump signal on the output, a lock-in amplifier has been connected between the signal input and the photodetector.

In order to check if the optomechanical switch is working, we redirected the output signal at port 3 of the device to the port 2 of the circulator and, then, the port 3 of the circulator to a photodetector (PD).

In fact, considering the amplitudes A and B of the optical signals exiting the two suspended waveguides, we will find (according to Eq. 2.63):

$$\begin{aligned} A &= \left|\cos\left(\tfrac{\pi L \Delta n_s}{\lambda}\right)\right|, \\ B &= \left|\sin\left(\tfrac{\pi L \Delta n_s}{\lambda}\right)\right|. \end{aligned} \tag{2.64}$$

The power exiting from port 3 of the device can be described as the square of the interference between two optical signals of amplitudes A and B, with a difference in their optical path of $\Delta L n_{eff}$

$$P_o = \frac{1}{2}\left[A\sin(\omega t) + B\sin\left(\omega t + \frac{2\pi \Delta L n_{eff}}{\lambda}\right)\right]^2. \tag{2.65}$$

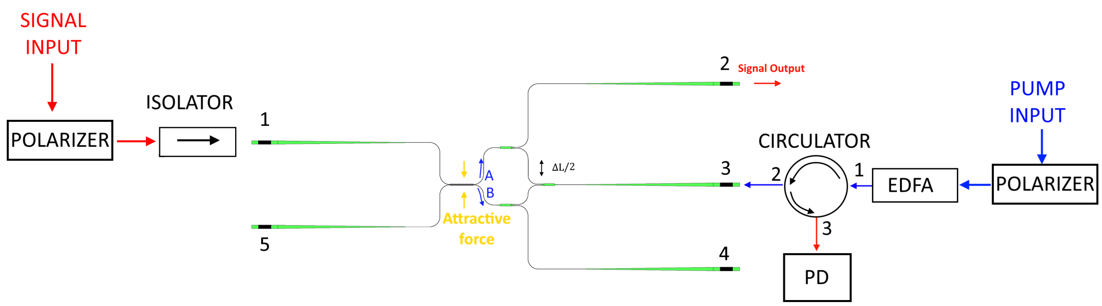

Figure 2.31: Conceptual setup for experimental measurement.

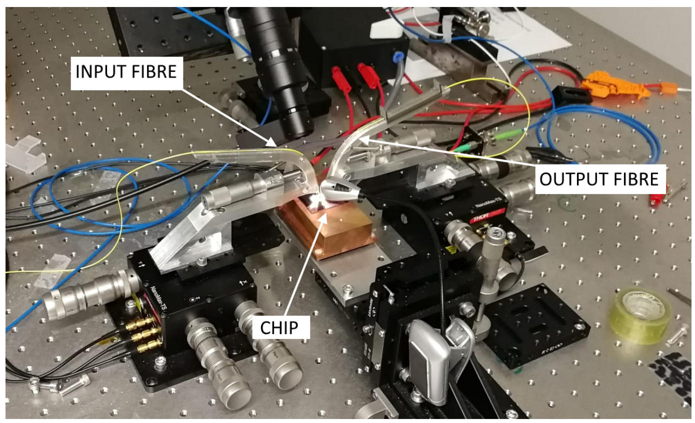

Figure 2.32: Photo of the experimental setup for the measurement. In the picture the two fibres are visible, together with a moveable stage where the integrated chip is fixed.

So, we obtain an average measurable power of:

$$P_{o,avg} = \frac{1}{2}\left[1 + \sin\left(\frac{2\pi L \Delta n_s}{\lambda}\right)\sin\left(\frac{2\pi \Delta L n_{eff}}{\lambda}\right)\right]. \tag{2.66}$$

In conclusion we expect the power read at port 3 of the circulator to vary with Δn_s, that depends on the optical force between the suspended arms, and so on the pump input power.

Figure 2.32 shows a part of the measurement setup. Figure 2.33 shows the normalized output power measured at the photodetector, for different signal wavelengths and for a fixed pump wavelength of 1570.5 nm (that excites the attractive force ac-

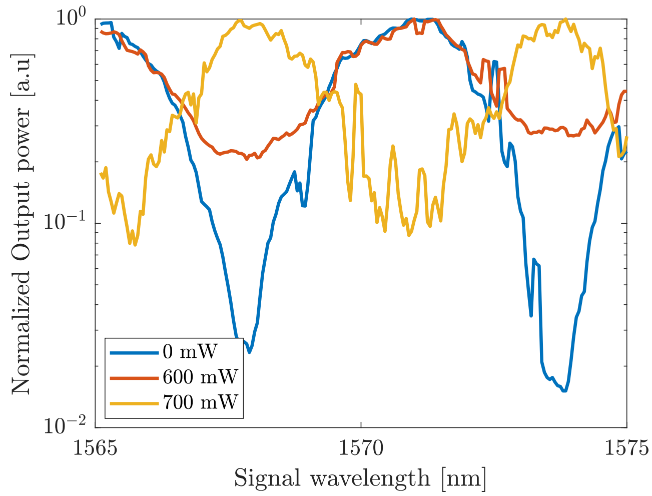

Figure 2.33: Normalized output power as a function of the wavelength of the input signal, for different amount of optical power at the pump input. The power of the mode exerting the optical force is estimated to be 20-30 times lower than than laser injected power, due to the grating couplers and the MMIs losses.

cording to our experiments). It is possible to appreciate that a change in the signal output spectrum for different values of the power of the pump input. This shows the expected behaviour of the device. Actually, the results in Figure 2.33 can be interpreted as follows: the attractive optical force generated by the pump input varies the term Δn_s; consequently, the output power measured at port 3 of the circulator is varied according to Eq. 2.66. Unfortunately, the device stopped working after the pump power was increased up to 800 mW. We imagine that the attractive force between the suspended waveguides could have stuck them. If verified, this behaviour could be exploited for non-volatile memories.

2.4.6 Final considerations

In this section it has been experimentally demonstrated that optical forces can enable the possibility of designing new devices, as optomechanical switches and other useful components for optical networks and other applications. Optomechanical solutions could pave the way to a new generation of all optical chips and provide completely new functionalities.

Chapter 3

Quartz-Enhanced PhotoAcoustic Spectroscopy

3.1 Introduction to Quartz-Enhanced PhotoAcoustic Spectroscopy

Photoacoustic spectroscopy (PAS) is an indirect absorption spectroscopy based on the photoacoustic effect and typically using lasers as excitation sources [48]. When light at a specific wavelength is absorbed by the gas sample, the excited molecules will subsequently relax to the ground state either through emission of photons or by means of non-radiative processes. These processes produce localized heating in the gas, which in turn results in an increase of the local pressure. If the incident light intensity is modulated, the generation of thermal energy in the sample will also be periodic and a pressure wave, i.e. a sound wave, will be produced at the same frequency of the light modulation. The PAS signal can be amplified by tuning the modulation frequency to one of the acoustic resonances of the gas sample cell [115]. The key advantage of this technique is that optical detector is not required, and the resulting sound waves can be detected by a commercial hearing aid microphone. The latest evolution of the PAS technique is Quartz Enhanced Photoacoustic Spectroscopy (QEPAS), which employs quartz tuning forks (QTF) as core sensitive element [49]. The QTF acts as a sharp resonator and piezoelectric transducer at the same time. The use of QTFs has elevated the QEPAS technique to the best candidate for in-situ and real-time trace gas detection, because of an unmatchable level of compactness, extremely high sensitivity (down to ppt), immunity to environmental noise and numerous possibilities of development and upgrade of this technique [116]. QTFs are employed in different applications fields and in most of the case are used for timing and sensing aims. Their main features are: i) resonance frequencies typically falling in the kHz-MHz range, depending on prongs dimensions and quartz crystal properties; ii) high frequency stability of these resonances, with frequency shifts approximately of 0.04 ppm/(°C)^2 over a wide temperature range, from -40 °C to 90 °C; iii) high quality factors, of few tens of thousands in air at the atmospheric pressure; iv) QTFs have a low cost and small size, thus enabling mass-production [117]. Until 2013, all QEPAS sensors reported in literature made use of QTFs designed for timing applications to vibrate at a resonance frequency of 32,768 Hz. The two prongs of these QTFs are typically 3 mm long, 0.35 mm wide and 0.34 mm thick and are separated by a gap of 0.3 mm. They have a quality factor as high as 30,000 in air, increasing up to 100,000 in vacuum [49]. In QEPAS, to increase the effective interaction length between the radiation-generated sound and the QTF, an acoustic resonator is also usually installed. The acoustic system composed of the QTF and the acoustic resonator is referred as QEPAS spectrophone. The resonators used so far consist of two metallic tubes aligned perpendicular to the QTF plane (on beam-QEPAS) [118], parallel to the QTF plane (off-beam QEPAS) [119] or one single tube placed between the QTF prongs with a pair of small slits in correspondence of the pressure maximum [120]. One of the main issues with QEPAS based sensor systems is the required focusing of the laser excitation beam between the QTF prongs. The laser beam must not hit the prongs since otherwise a large undesirable non-zero background arises due to the laser contribution, hence limiting the sensor detection sensitivity [53]. This problem triggered several solutions, for instance the use of the Hollow Core Waveguides (HCW) to be coupled with the laser sources for guiding the light and clean up the laser beam mode profile [54, 55, 56]. The short optical pathlength, the capability to reach high detection sensitivity, high compactness and robustness represent the main distinct advantages which made QEPAS the leading-edge technique mature for out-of-laboratory operation, targeting in-situ applications such as environmental monitoring and leak detection [57, 58]. Nevertheless, for those applications in which sensors must work in challenging environments like downhole analysis of natural gas or early fire detection empowered by the drone technology, the further miniaturization step requires a different level of integration of the opto-acoustic components [59, 60, 61]. The approach we propose in this work is meant to exploit the enhancement of light provided by resonant cavities together with a mechanical microresonator to make the performances of a semi-integrated QEPAS sensor comparable with those obtained in free space. The integration of a laser source on silicon chips is today possible thanks to bonding processes [121]. Therefore, the possibility of integrating all the optical components of a QEPAS system on a silicon chip, apart from the QTF, could represent a promising alternative. Due to some limitations of integrated waveguides, such as a small confinement factor on cladding [122], it is not easy to achieve performances comparable to the state-of-art QEPAS. Thus, a feasibility study on semi-integrated versions of QEPAS setups will be here presented and supported by numerical simulation in COMSOL Multiphysics. In this study five different configurations, schematically depicted in Figure 3.1, will be investigated and compared:

- FS-QEPAS (Free Space QEPAS): standard configuration without mechanical resonators
- MR-QEPAS (Mechanical Resonator QEPAS): a free space configuration using a mechanical microresonator to enhance the pressure signal (state-of-art)
- SI-QEPAS (Semi-Integrated QEPAS): semi-integrated version without mechanical resonators
- MRSI-QEPAS: (Mechanical Resonator, Semi-Integrated QEPAS): semi integrated version with a mechanical resonator
- OMRSI-QEPAS: (Optical and Mechanical Resonators, Semi-Integrated QEPAS): semi-integrated version with a mechanical resonator and an optical resonator

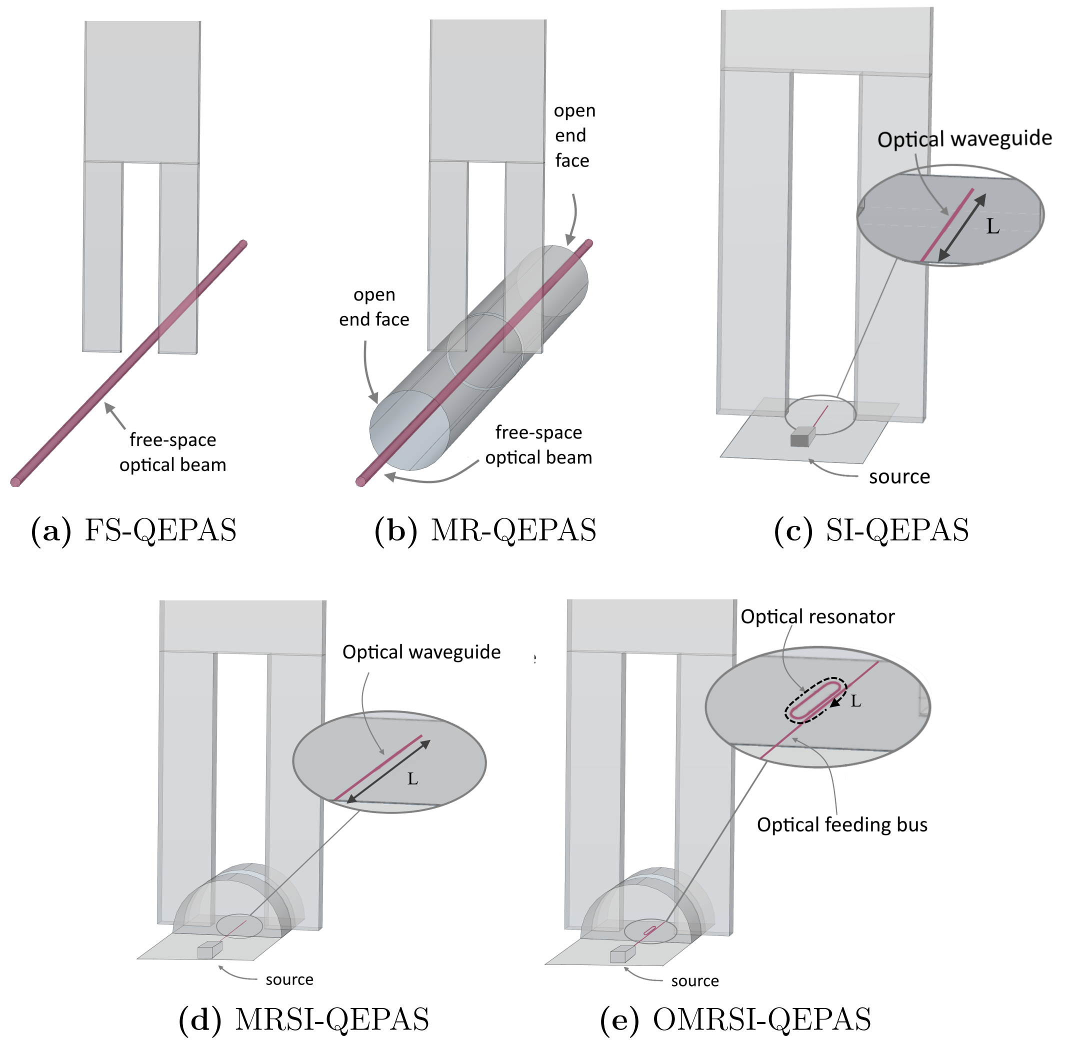

Figure 3.1: Different configurations of QEPAS setups analysed in this work. FS-QEPAS (a) is a simple QEPAS configuration without any mechanical resonator. MR-QEPAS (b) is a free space configuration with a mechanical resonator. SI-QEPAS (c) is a semi-integrated version of QEPAS without mechanical resonators. MRSI-QEPAS (d) is a semi-integrated version of QEPAS with a mechanical resonator. OMRSI-QEPAS (e) is a semi integrated version of QEPAS with a mechanical resonator and an optical resonator (fed by an optical bus). [62]

3.2 A semi-integrated QEPAS sensor

3.2.1 Macroscopic modelling of QEPAS

In photoacoustic spectroscopy, as well as in QEPAS, the signal S obtained from the acoustic-electrical transducer, i.e. the microphone or the tuning fork, is proportional to the absorption coefficient α of the gas sample, the radiation-to-sound conversion efficiency ϵ, the QTF quality factor and the optical power P available from the laser source [116]:

$$S \propto \alpha Q P \epsilon. \tag{3.1}$$

In order to design a semi-integrated version of the QEPAS sensor with performances comparable with the standard QEPAS systems, we initially try to model the soundwave generated by photoacoustic effect starting from the fraction of optical power interacting with the target gas. The light absorbed by the gas is converted into a heat source (H) proportional to the absorbed optical intensity I [123]:

$$H(\overline{r}, t) = \alpha I(\overline{r}, t), \tag{3.2}$$

where α is the power absorption coefficient per unit length. The generated heat H and the consequent energy relaxation gives rise to acoustic waves. The Helmholtz equation in the harmonic regime can be written as follows [48]:

$$\left(\nabla^2 + \frac{\omega^2}{v^2}\right) p(\overline{r}, \omega) = -\frac{\gamma - 1}{v^2} j\omega H(\overline{r}, \omega), \tag{3.3}$$

where p is the local pressure, v is the local speed of sound, γ is the ratio between the specific heat at constant volume (C_V) and the specific heat at constant pressure (C_P) and ω is the angular frequency of the laser excitation.

The solutions of the wave equations are determined by the boundary conditions. In particular, the solution p can be expressed as an expansion over the modes p_j with amplitudes A_j [48]:

$$p(\overline{r}, \omega) = \sum p_j(\overline{r}) A_j(\omega). \tag{3.4}$$

It can be found that under rigid-walls boundary conditions (good approximation for the boundary condition of microresonators) [48]:

$$A_j(\omega) = \frac{-j\omega^2}{\omega_j} \frac{[(\gamma - 1)/V_C] \int p_j^* H dV}{1 - \frac{\omega^2}{\omega_j^2} - j\frac{\omega}{\omega_j Q_j}}, \tag{3.5}$$

where ω_j is the resonance angular frequency of the j-th mechanical resonant mode, Q_j is the quality factor of the j-th mode, V_c is the volume defined by the boundary conditions.

By approximating H as a two-dimensional Dirac-delta input for the Helmholtz equation (possible if the linear dimensions of the cross-section of the beam are much smaller than the acoustic wavelength) and by considering z the direction of propagation of the light beam:

$$H(\overline{r}, t) = \alpha P_{gas} \delta(x, y), \tag{3.6}$$

with P_{gas} the fraction of the optical power interacting with the target gas. Thus, Eq. 3.6 becomes:

$$A_j(\omega) = \frac{-j\omega^2}{\omega_j} \frac{[(\gamma - 1)/S_C] p_j^*(0, 0, z) \alpha P_{gas}}{1 - \frac{\omega^2}{\omega_j^2} - j\frac{\omega}{\omega_j Q_j}}, \tag{3.7}$$

with S_C the area of the cross section delimited by the boundary conditions. Using Eq. 3.4:

$$p = \sum p_j A_j = \alpha P_{gas} \sum \frac{-j\omega^2}{\omega_j} \frac{[(\gamma - 1)/S_C] p_j^*(0, 0, z)}{1 - \frac{\omega^2}{\omega_j^2} - j\frac{\omega}{\omega_j Q_j}} p_j(\overline{r}). \tag{3.8}$$

So, we obtained that the amplitude of the pressure, and thus the QTF signal is proportional to the optical power interacting with the target gas (P_{gas}).

In free space, all the power of the laser interacts with air, whereas in integrated optical devices, the light is guided into a medium, thus, only a small fraction of the power propagates outside the guide as an evanescent wave and interacts with the gas. The air confinement factor (Γ_{gas}) is defined as the fraction of the power propagating in air divided by the total power propagating through the waveguide (P_P):

$$\Gamma_{gas} = \frac{\int_{gas} S_z d\overline{S}}{\int_{total} S_z d\overline{S}} = \frac{P_{gas}}{P_P}, \tag{3.9}$$

with S_z the Poynting vector along the direction of propagation z.

It means that with the same amount of power consumption and under the same boundary conditions, the pressure amplitude p of the sound wave, photoacoustically generated by the evanescent wave in waveguide-based structure Γ_{gas} times lower in a waveguide-based structure than in free space.

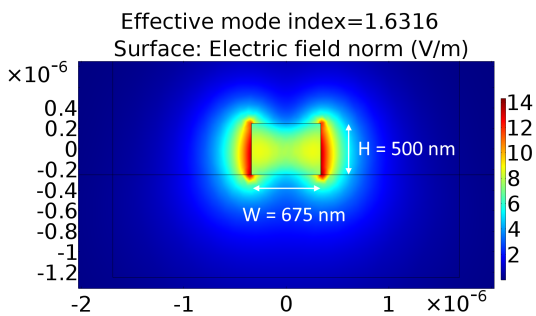

(a)

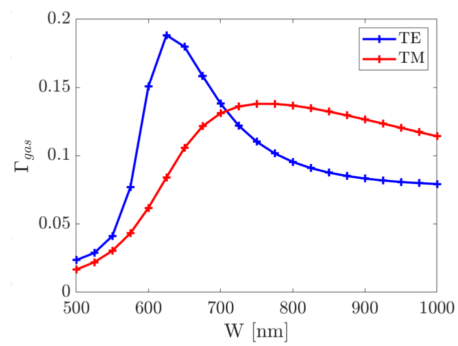

(b)

Figure 3.2: Light mode in waveguide-based structure for a waveguide width $W = 600nm$ and height $H = 500nm$ (a) and Confinement Factor Γ_{gas} for different values of the widths of the waveguide (with $H = 500nm$) for TE and TM modes (b) [62].

Figure 3.2b shows the Γ_{gas} as a function of the width W of a silicon waveguide (for a standard waveguide height of 500 nm) or a propagating radiation with a wavelength $\lambda = 3345$ nm, useful for detecting methane and ethane in the infrared region. As it can be seen, the maximum achievable confinement factor is around 18% for this kind of strip waveguides (Fig. 3.2b).

We considered that the dominant source of loss for this waveguide is due to the bulk loss in SiO_2 (10 dB/cm at a wavelength of 3.345 μm [124]). Consequently, the optimal waveguide design for this application is a trade-off between the fraction of evanescent power in air (Γ_{gas}) and the total loss of the waveguide. We chose a width of 675 nm, for which the fraction of power in SiO_2 is 27%, meaning a total propagation loss of 2.7 dB/cm (propagation loss in silicon is negligible). Figure 3.2

shows the designed waveguide (500 nm x 675 nm) and the chosen mode (TE) that will be used for all the integrated configurations in the next sections.

3.2.2 Perfomances comparison without microresonators: FS-QEPAS vs SI-QEPAS

The key idea of this study is to demonstrate that a semi-integrated configuration of a QEPAS setup can potentially replace the standard free-space configuration making the space occupation much lower and eliminating any optical alignment issue. As a first step, we simulated the photoacoustic generation when a free-space laser beam propagates between the prongs of a bare QTF (FS-QEPAS, Fig. 3.1.a) which represents a non-interactive element in the following analysis.

Then, the FS-QEPAS model has been compared with a similar structure exploiting an integrated waveguide on a silicon chip (SI-QEPAS, Fig. 3.1.c)

The fully mechanical simulations have been performed by implementing the Helmholtz equation (Eq. 3.3) on the "Pressure Acoustic, Frequency Domain" module of COMSOL Multiphysics, with the heat source H obtained by combining eq. 3.2, using Eq. 3.9. The wavelength selected is resonant with an optical transition related to the C-H bond stretching of methane at wavenumber $\sim$ 2989 cm^{-1} (wavelength $\sim$ 3345 nm) and having an absorption coefficient of $\alpha \sim$ 12cm^{-1} at a pressure of 1 atm and a temperature of 296 K [125].

The QTF selected as a reference to model the non-interacting probe in our design is a tuning fork having a resonance frequency of 15.8 kHz, a prong thickness of 250 µm, a prong spacing of 800 µm and thus slightly different from the one investigated in ref [126], which has an enlarged prong spacing of 1.5 mm. The other dimensions of the QTF have no influence on the simulations, because the prong internal surfaces were treated as hard wall boundary conditions. An implementation of Helmholtz equation was used in COMSOL Multiphysics to simulate the pressure signal generated from a heat source located between the free ends of the QTF. In fact, the QTF is aligned so that the light beam propagates perpendicular to the QTF plane and exactly centred between the top of the prongs, where the vibrational antinode is theoretically expected [49]. In the FS-QEPAS case, the light beam has been simulated with an equivalent 100 µm radius uniform power beam, whereas in the SI-QEPAS case, the light propagates into a waveguide on the surface of an integrated chip (TE mode of a 675 nm x 500 nm silicon strip waveguide in Figure 3.2a) and has been simulated with an equivalent 0.5 µm-radius uniform beam with equivalent power equal to $P_P\Gamma_{gas}$. The length of the waveguide has been varied between 400 µm and 1 mm. For these lengths, the propagation losses due to SiO_2 have not been accounted into simulation, because negligible. In both cases a total input power $P_P = 1$mW was considered. Figure 3.3a shows the pressure signal in static conditions (for non-vibrating prongs) for a waveguide length L of 1 mm. It is easy to appreciate that for the SI-QEPAS configuration, the pressure signal in the proximity of the prongs is almost one order of magnitude lower than in FS-QEPAS case.

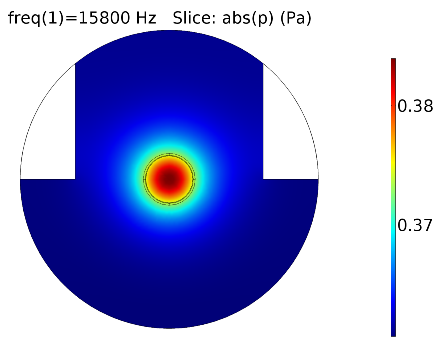

(a)

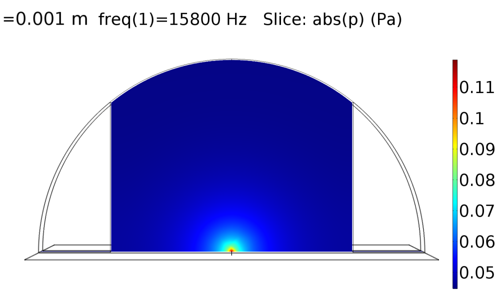

(b)

Figure 3.3: Acoustic pressure field (Pa), with optical power of 1mW without resonators in FS-QEPAS configuration (a) and SI-QEPAS configuration (b) [62].

3.2.3 Perfomances comparison with microresonators: MR-QEPAS vs MRSI-QEPAS

The employment of acoustic resonator tubes has been widely exploited in literature and in sensor prototypes to increase the SNR of the piezoelectric signal. In the on-beam configuration, a pair of tubes are aligned perpendicular to the QTF plane, with the tube axes at the same height of the fundamental vibration mode antinode and at a distance from the QTF typically of several tens of micron [118]. Thus, when the modulated laser radiation propagates through the dual tube system, a standing soundwave is photoacoustically generated, with its pressure peak occurring at the vibrational antinode between the prongs. The schematic of the dual tube on-beam configuration, here referred as MR-QEPAS, is shown in Fig. 3.1.b. acting as a micromechanical resonator enhancing the pressure of the photoacoustic soundwave. This is the most used QEPAS configuration [118]. The MR-QEPAS simulated for this investigation is composed of a cylindrical microresonator open at its end faces. The distance between the internal edges of the tubes was set to 310 µm to accommodate a QTF for sensing the pressure variations. Each tube is 10.3 mm long, with an inner diameter of 1.27 mm. These tube dimensions demonstrated to provide the highest SNR when acoustically coupled with a 15 kHz custom QTF [126]. The MR-QEPAS was then compared to a SI-QEPAS configuration in which a closed micromechanical resonator was added in order to obtain a further enhancement of the pressure in the proximity of the QTF prongs. The micromechanical resonator is made up of a closed semicylinder with a central gap where the QTF is located. If the laser radiation is delivered through the micro mechanical resonator by means of a feeding bus, the light can be coupled again to the waveguide so that the Γ_{gas} portion of the input power can interact with the target gas over a length L (Figure 3.1d, MRSI-QEPAS). The size of the gap at the center of the microresonator is the same as in the MR-QEPAS). The inner diameter of the semicylindrical resonator is 1.27 mm and the total microresonator length is 2 mm. The pressure signal per input power obtained at the base of the QTF prongs was simulated and compared in the MR-QEPAS and in the semi-integrated version MRSI-QEPAS. The light beams were simulated as indicated in the previous paragraph. The colormaps in Figures 3.4a and 3.4b show the pressure signal per input power on the central cross-section for both the configurations (with $L = 1$mm in the MRSI-QEPAS case).

In the case of MRSI-QEPAS, since the system is closed, all the optical power absorbed should be converted into a pressure signal. Through an energetic approach it is possible to find the dependence of the pressure signal on the length of the absorption path in the MRSI-QEPAS (approximation of closed system). In particular, when considering an optical mode propagating in an integrated waveguide, the fraction ($P_{abs,int}$) of the total power propagating in the waveguide (P_P) that has been absorbed by the target gas over a length L (in the hypothesis of small absorption) is [127]:

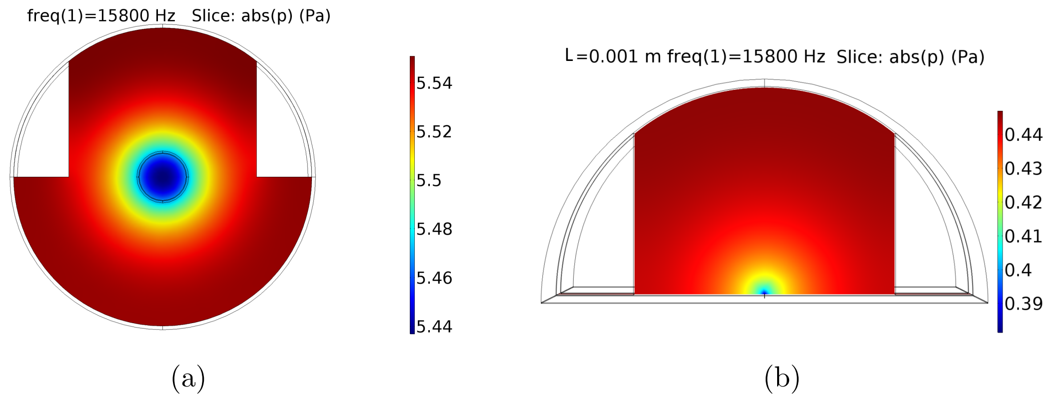

Figure 3.4: Acoustic pressure field (Pa), with optical power of 1mW without resonators in the MR-QEPAS configuration (a) and MRSI-QEPAS configuration (b) [62].

$$P_{abs,int} = P_P \Gamma_{gas} \alpha L. \tag{3.10}$$

Consequently, in MRSI-QEPAS we expect p to be proportional to the length of absorption L. The simulation results confirm that the pressure amplitude per input power varies linearly with the absorption length.

As it is possible to see in Figure 3.5, the pressure signal obtained in MRSI-QEPAS is one order of magnitude lower than in the MR-QEPAS. However, the guidance of the laser light can be further and more effectively exploited by implementing an optical resonant cavity to be directly coupled with the waveguide modeled and simulated in SI-QEPAS and MRSI-QEPAS configurations.

3.2.4 Optical resonant enhancement: OMRSI-QEPAS

The results of the previous paragraphs showed that the integrated solutions (SI-QEPAS and MRSI-QEPAS) produce a pressure signal one order of magnitude lower than the corresponding free space configurations (QEPAS and MR-QEPAS). In order to achieve better performances in terms of signal amplitude with a semi-integrated setup, an optical-resonant-cavity architecture in the MRSI-QEPAS is here proposed, with the aim of increasing the optical power interacting with the target gas starting from the same input power simulated in the previous configurations. The modifica-

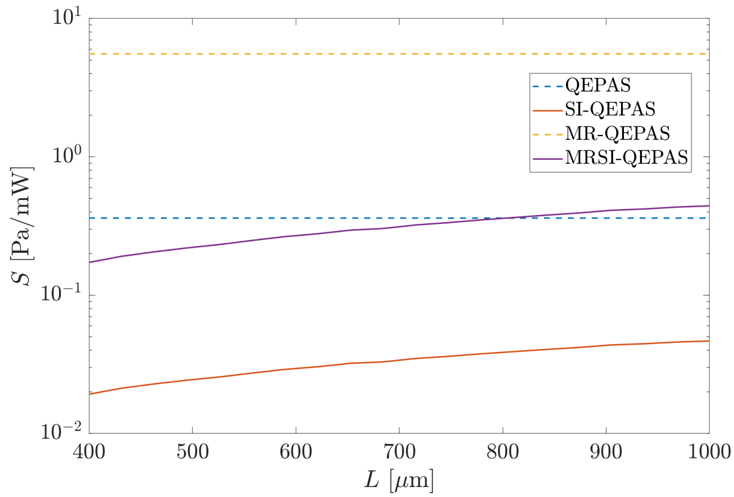

Figure 3.5: Pressure signal per input power (S) as a function of the length of the waveguide in the SI-QEPAS and MRSI-QEPAS compared to the pressure signal per input power in QEPAS and MR-QEPAS [62].

tion to the MRSI-QEPAS setup is shown in figure 3.1.e. It is possible to see that an optical resonator is fed by an optical bus. The racetrack resonator is designed to have a total length L and a gap between the two long-side waveguide of 80 µm (bend radius of 40 µm) It is easy to demonstrate that the enhancement factor EF, calculated as the ratio between the power circulating into a section of the cavity (P_{cav}) (modulated at the resonance frequency of the tuning fork) and the input power within the feeding bus (P_P) is [128]:

$$E_F = \frac{P_{cav}}{P_P} = \frac{e^{-\alpha_{wg}L}\kappa^2}{(1 - e^{-\frac{\alpha_{wg}}{2}L}\sqrt{1-\kappa^2})^2} \approx \frac{4\kappa^2}{(\alpha_{wg}L + \kappa^2)^2}, \tag{3.11}$$

with κ^2 the nondimensional power coupling efficiency between a feeding waveguide and the resonator and with α_{wg} the propagation loss of the waveguide (in the absence of target gas).

In order to estimate the enhancement factor, we considered the propagation loss already estimated (2.7 dB/cm) and bend losses. The bend losses were estimated by evaluating the superposition of the optical mode in the straight waveguide and in the bent waveguide (equal to 99.6%, with a curvature radius of 40 µm).

Parameter	Symbol	Value
Cavity length	L	1000.63 μm
Order of resonance	m	488
Resonance wavelength	λ_0	3.34555 μm
Q-factor	Q	19749
Finesse	F	40.5
Free spectral range	FSR	6.86 nm

Table 3.1: Parameters of the optical resonator.

A bend loss of around 0.013 dB per roundtrip (0.013dB/L, with L the length of the resonator) was obtained. So, α_{wg} = 2.7 dB/cm + 0.013dB/L. The parameters of the final designed resonator are summarized in Table 3.1.

Figure 3.6 shows the enhancement factor as a function of the coupling efficiency and the length of the resonator. By properly designing the distance d_{gap} between the feeding bus and the resonator, the power coupling efficiency κ^2 can be calculated end engineered through the following expression (valid for straight couplers) [114]:

$$\kappa^2 = sin^2\left(\frac{\pi L_{cp}\Delta n(d_{gap})}{\lambda}\right). \tag{3.12}$$

Once the κ has been designed for the necessary pressure amplitude, the distance d_{gap} between the feeding bus and the resonator can be designed through the following expression (valid for straight couplers) [114]:

$$\kappa^2 = sin^2\left(\frac{\pi L_{cp}\Delta n(d_{gap})}{\lambda}\right). \tag{3.13}$$

Here $\Delta n(d_{gap})$ is the difference between the effective indices of the even and the odd modes in the coupling region, where the evanescent coupling between feeding bus and resonator takes place. L_{cp} is the length of the coupling region and λ is the wavelength of input light. Figure 3.7a shows the pressure amplitude at a central cross section obtained for an optical resonator with a length of L = 1mm in an OMRSI-QEPAS configuration. Figure 3.7b shows the performance of the OMRSI-QEPAS as a function of L at different values of κ, compared with the pressure value obtained with MR-QEPAS. As it can be easily argued from the figure, in an OMRSI-QEPAS

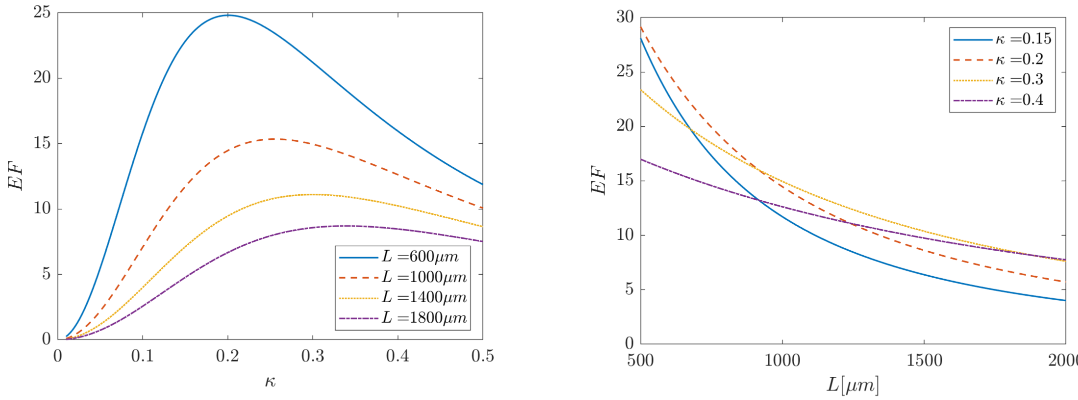

(a) (b)

Figure 3.6: Enhancement factor as a function of κ for different values of L (a) and enhancement factor as a function of L for different values of κ, with estimated loss $\alpha_{wg} = 0.69dB/cm$ (b) [62].

configuration comparable or higher-pressure values for the sound wavefront can be achieved with respect to a standard MR-QEPAS approach. Table 3.2 summarizes the peak pressure signals obtained for each simulated configuration. The obtained results demonstrate that an integrated configuration of QEPAS (in particular the OMRSI-QEPAS) can exceed the performances of the state-of-art QEPAS configurations. The use of optical enhancement can overcome the problem of a low air confinement factor thanks to the use of optical resonators. Figure 3.8 shows the final configuration of the OMRSI-QEPAS setup. Thanks to the possibility of bonding an external laser to a SOI chip, it is possible to feed the optical resonator through a feeding optical bus entering the mechanical resonator. The laser source should be placed sufficiently distant from the mechanical resonator and the QTF to guarantee an effective heat dissipation/cooling and avoid that temperature gradients in the gas affect the photoacoustic generation and response. As for the fabrication process, the initial step would be to etch the waveguides and the resonator on a standard Si/SiO_2 chip (500 nm of silicon layer). Then, the external laser would be bonded upon the SOI chip, which can be mounted inside an HHL-like package. As for the mechanical resonator, the simplest approach would be to mechanically bond it to the SOI chip. Finally, the QTF would be connected from the base to the upper enclosure of the

Configuration	Signal amplitude
SI-QEPAS (1-mm source)	0.047 Pa
FS-QEPAS	0.361 Pa
MRSI-QEPAS (1-mm source)	0.443 Pa
MR-QEPAS	5.550 Pa
OMRSI-QEPAS (1-mm source, $\kappa = 0.3$)	**6.396 Pa**

Table 3.2: Comparison of signal amplitude for different configurations.

packaging and then coupled with the ring resonator upside down.

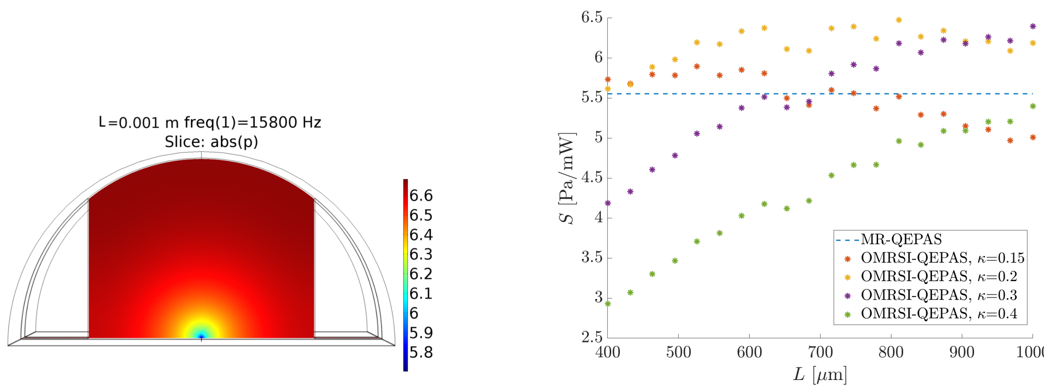

(a) (b)

Figure 3.7: Pressure signal (Pa) per input power of 1 mW over a central cross section in OMRSI-QEPAS (a) and Pressure signal per input power (S) as a function of the length of the waveguide in OMRSI-QEPAS, compared with MR-QEPAS (b) [62].

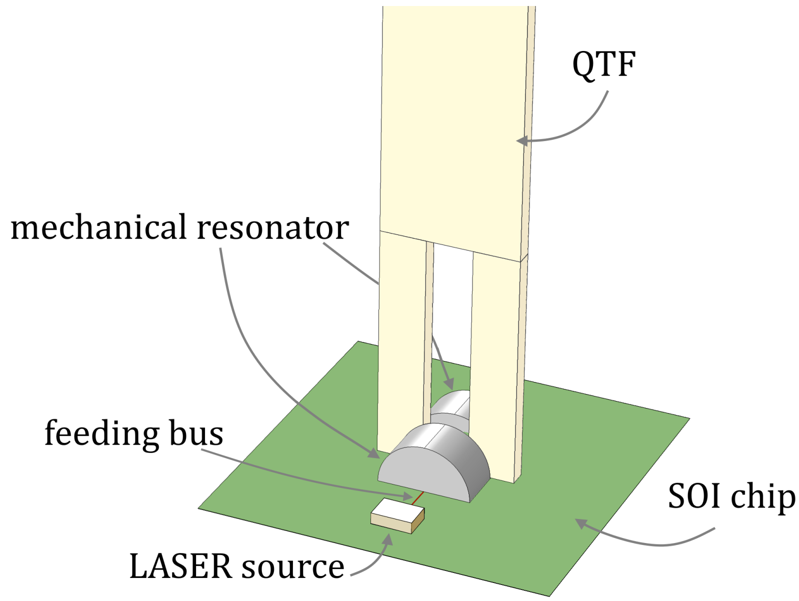

Figure 3.8: Final configuration of the OMRSI-QEPAS setup [62].

3.2.5 Final considerations

In this work it has been demonstrated that using an integrated chip for QEPAS sensing could represent a valid alternative to standard QEPAS that will make the sensor smaller and more stable, avoiding the necessity of optical alignment and allowing comparable performances to be achieved. Despite a limited confinement factor of integrated silicon waveguides for a wavelength of 3.345 μm, the use of a mechanical microresonator and optical resonant enhancement allows a significant pressure signal to be achieved with the same power consumption of standard QEPAS setups. The proposed device could represent a promising solution for miniaturizing the dimensions of a QEPAS sensor, since all the optical parts could be integrated on a chip, except for the quartz tuning fork, still necessary to guarantee a high mechanical quality factor.

Conclusion

In this thesis, the concept of Optomechanics has been investigated in its broad meaning. The interaction between the light and mechanics enables several possibilities both for sensing and for actuation. Optical gyroscopes are one of the most famous examples where mechanical motion affects light behaviour. According to the relativistic effect called Sagnac effect, the resonance frequencies of two counterpropagating modes in a ring resonator are separated by a quantity proportional to the angular velocity of the frame. However, the possibility of miniaturizing the optical gyroscope is limited by the fact that the resonance splitting is proportional to the radius of the ring resonator. In the first chapter we introduced the concept of parity-time symmetry as a solution for the integration of angular velocity sensors. By setting up two coupled optical resonators designed to be at the so called "exceptional point", it could be demonstrated that the eigenfrequency splitting is proportional to the angular velocity of the device, with a sensitivity several orders of magnitude higher than the classical Sagnac gyroscope. In this thesis it was demonstrated that one problem of the parity-time symmetric gyroscope is the instability of the optical eigenmodes when the system is in rotation. That's why the idea of the anti-parity-pime-symmetric gyroscope was proposed, using a U-shaped auxiliary waveguide to indirectly couple two optical resonators. The proposed solution has been shown to be an interesting alternative for angular velocity sensing, thanks to the easy readout scheme and the absence of modes instability. A simple broadband source, together with a photodetector could be used to read the output of the sensor. Finally, a new configuration for an anti-parity-time-symmetric gyroscope has been proposed. It is different from the U-shaped configuration and uses only an auxiliary straight waveguide to indirectly couple two optical resonators. This architecture has been shown to be much more robust, insensitive to some fabrication errors, with respect to the

U-shaped one.

In the second chapter optomechanical forces have been investigated. In particular a generalized model able to calculate the mechanical displacement of only one degree of freedom of the optomechanical setup. In particular the model, initially proposed by Rakich, has been extended to systems where gain or loss are considered. Then, the model has been used to evaluate the effect of optical forces in parity-time symmetric system with suspended waveguides in the coupling region. It has been demonstrated that it is possible to enhance the optical forces thanks to condition of parity-time symmetry. Secondly, an analytical modelling of the dynamics of optomechanically coupled suspended optical waveguides has been proposed, including a modelling of the damping, with the squeezing effect. Such an analytical model, together with the numerical proposed algorithm can be used to find the evolution of the system in the time domain even for complex optomechanical structures, such as optomechanical switches. Also, an experimental work on an optomechanical switch has been shown. In particular all the fabrication steps to fabricate the integrated optomechanical device has been explained. The most critical part during the fabrication has been the underetching of suspended waveguides. In fact, using a wet HF etching process caused the suspended waveguides to get stuck. Using a ZEP mask and a vapor HF etching, unexpected HF bubbles appeared on the surface. So, a hard mask has been used to guarantee the successful underetching of the device. Finally the experimental measurement on the chip showed the expected behaviour of the device.

In the last chapter the state-of-art QEPAS sensor has been investigated and a completely new semi-integrated sensor has been proposed. One problem of the state-of-art QEPAS sensors is the necessity of alignment for optical components. Moreover, the dimension of all the devices involved in the setup makes it difficult to realize portable and compact sensors. The idea proposed in this thesis is to integrate all the optical components needed to guide the light in the proximity of the Quartz Tuning Fork to drastically reduce the dimension of the overall setup and to avoid the problem of optical alignement. The possibility of using integrated optical waveguides to guide light makes it possible to use optical resonators to enhance the photoacoustic signal that is read through a Quartz Tuning Fork. The proposed setup is meant to use an integrated laser bonded to a silicon chip, where all the waveguides are realized. In this case a very small mechanical resonator can be bonded over the silicon chip, in order to enhance the amplitude of the pressure signal. In such a way, performance comparable with the state-of-art QEPAS sensor can been achieved. Such a result could pave the way to a new generation of compact QEPAS sensor, that could overcome the problem of the size of the setups and of the alignment of optical components.

Appendix A

Appendix

In this appendix another important result of my PhD course is presented, which doesn't belong to the field of Optomechanics. This study is about a proposal for an electric vehicle with two motors combined via planetary gear train. The idea is to maximize the energy efficiency of an electric vehicle by combining two electric motors. The results of this study have been published in [129].

A.1 Introduction

Electric motors represent one of the prominent actuation technologies, offering very high efficiency at their nominal working point. However, their efficiency varies strongly with speed and torque [130, 131]. This is an issue as in robotics as in electric urban vehicles, where motors are required to work at a wide range of working points, thus implying low average efficiency. [132] The electrical vehicle is an interesting and efficient solution for transportation, especially for environmental reasons [133, 134, 135]. However, since motor efficiency rapidly changes with speed and torque [136], the average efficiency in frequently varying operating conditions can be very low [137, 138, 139]. In electric vehicles nominal power of a motor is calculated in the condition of maximum requirement of user power, necessary when the vehicle is running at its highest speed. However, in the majority of its use, the motor runs in very low efficiency condition, since it is required to work at values of speed and torque rapidly changing in time. In particular, in urban condition the speed of the vehicle (in case of single motor one-speed transmission) is very low, thus leading to very low energy efficiency and it becomes necessary to use efficiency maps [131, 140] to evaluate the average efficiency during time in standard urban cycles. Drive electronics for electric motor have been improving with powerful processors, much smaller and cheaper than in the past. Such a condition allows designers to implement more complex control algorithms to achieve a better energy efficiency of electric vehicles. In literature several references dealt with the optimization of the efficiency of electrical motors: in [141, 142, 143, 144] the cycle is reduced to some points where the consumption is the highest, to evaluate and then maximize the energy consumption of the machine over the cycle. In [145] and [146], the torque-speed plane is divided into several uniform areas, replaced by their barycentre. The performance of the motor is evaluated weighting the consumptions of these points with the ratio between the number of points in each area and the total number of points on the cycle. These methods usually combine finite element analysis and analytical model. In [147] the technology of a series of gearless electrical continuously variable transmission propulsion system is developed (E-CVT). In that work, a differential evolution algorithm coupled with finite element method is adopted to optimize torque, energy efficiency and torque ripples of the E-CVT system. In [148] the design of an efficiency-optimized induction motor is considered, where genetic algorithm is chosen as the tool for optimization. In [149] an evolutionary optimization procedure for the design of permanent-magnet motors for electric vehicle applications is proposed, considering a specific drive cycle, with multiple operating points. The optimization technique is performed through an adaptive differential evolution algorithm using a dynamic variation of the mutation factor, combined with finite-element and circuit models. Several alternatives have also been proposed in literature to use an electric motor in the point of its best efficiency [150], such as the combination of variable transmissions with a series spring [151]. In [140] a system with an Infinitely Variable Transmission has been proposed to maximize the efficiency of an electric motor. In [152] a planetary gear has been studied to maximize the energy stored by a wind system. In such a configuration, the analytical optimization has been made possible by the analytical relation between the torque and the speed of the wind turbines. The use of a planetary gear also allows the combination of the power of two motors to avoid transmission nonlinearities [153]. In [154] a high-level algorithm is developed to adaptively split the load between two sources for an electric vehicle adopting a hybrid energy storage system that can effectively reduce power stress applied to batteries. Currently, the motor of electric vehicles is directly connected to the wheels with a gear-train, with fixed ratio. Consequently, this architecture makes the motor speed directly dependent on the speed of the vehicle. So, for example when the vehicle is traveling at low speed, the motor often runs at low efficiency-working conditions. In this work, we propose the use of two electrical motor drives combined through a planetary gear train. The aim of the work is to increase the energy efficiency of the vehicle, by optimizing the combined speeds of two motors. Such a solution is possible thanks to the degree of freedom provided by the planetary differential. With respect to the work in [136] we propose the application of such a system to electric vehicles, to demonstrate that using that approach for an electric vehicle could be more efficient from an energetic point of view than a single motor with one speed transmission. In particular, we will optimize the speed of each motor in order to achieve the maximum efficiency of the system. The obtained driving curves of each motor will be used as the driver for the control unit of the electrical vehicle. Moreover, we propose the optimal choices for the power ratings of the motors and the gear ratio ρ to maximize the energy efficiency during a standard ECE-15 urban cycle. The main aim of the work is: a) Evaluating the improvement in the energy efficiency during an urban cycle, using the proposed architecture for an electric vehicle; b) Determine the nominal specifications of the planetary gear and of the electric motors maximizing the efficiency; c) Evaluating the speed and the torques of each motor in order to maximize the efficiency of the vehicle in every working condition of the vehicle

A.2 Model of a two motors-electric vehicle with a planetary gear

The electric vehicle that is here considered is provided of two induction motors, supplied by an inverter, and a planetary gear. The idea we propose is that the global efficiency of the system can be optimized by exploiting the degree of freedom provided by the planetary gear. Indeed, the planetary gear has a degree of freedom we can exploit in the choice of the speeds of the combined motors, for each value of the speed required by the vehicle. We modeled the efficiency of each electrical motor through a standard efficiency map. It is known that the efficiency of the motor is high for high speed and low torque. However, the efficiency drops for high torques and low speeds. This is a typical condition for induction motors. A motor drive directly connected to the wheels with a gear train would work in a low efficiency condition when the vehicle is running at low speed, especially during a standard urban cycle. Since the electrical vehicle is mainly designed for urban cycles, it often runs in a low-efficiency working condition. A further improvement of the proposed architecture is that it requires two motor drives with a half nominal power with respect to a single motor used in the standard electrical motor. As a result, when low power is required by the vehicle, only one motor will work, leading to a great improvement, due to the much higher proximity to its nominal power.

A.2.1 Velocities Analysis

A usual planetary gearbox consists of a sun gear, a ring gear, planetary gears and a carrier. Usually the ring is grounded, whereas the sun is used as input and the carrier as the output. In the following model we will consider a dual-motor actuation, where also the ring is used as input in order to achieve a maximization of the efficiency of the planetary gear system. We will consider the system in Figure A.1, where the sun, the ring and the carrier rotate with velocities ω_S, ω_R, ω_0, respectively.

In order to design our system, we need the relations between the velocities of the sun (ω_S), the ring (ω_R) and the carrier (ω_o). In particular, if we consider an observer on the carrier, he will see the sun rotating with a velocity $\omega_S - \omega_o$ and the ring with a velocity $\omega_R - \omega_o$. It is possible to evaluate the Willis ratio as:

$$\tau_w = \frac{\omega_R - \omega_0}{\omega_S - \omega_0} = \left(-\frac{r_S}{r_P}\right)\left(\frac{r_P}{r_R}\right) = -\frac{r_S}{r_R}\tau_w = \frac{\omega_R - \omega_0}{\omega_S - \omega_0} = -\frac{1}{\rho}, \tag{A.1}$$

with $\rho = r_R/r_S$, it is possible to obtain the relation between the velocities of the carrier, the ring and the sun:

$$\omega_o = \frac{1}{1+\rho}\omega_S + \frac{\rho}{1+\rho}\omega_R. \tag{A.2}$$

From this relation it is evident that, once fixed ρ on the basis of geometrical

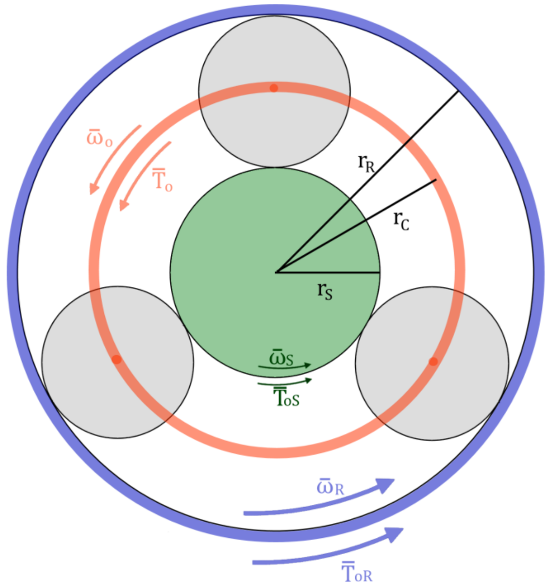

Figure A.1: Schematic of a classical planetary gear [129].

constraints, the speed of carrier ω_o results to be a weighted sum of the speeds of the sun and the ring. Equation A.2 represents the only kinematic equation describing the system, while ω_S and ω_R are the two variables (for each operative condition). Once defined the working point, there is one remaining degree of freedom in the choice of the sun and the ring speeds. Once defined the speed ratio i=ω_R/ω_S, it is possible to obtain the expressions of ω_S and ω_S:

$$\omega_S = \frac{1+\rho}{1+\rho i}\omega_o, \tag{A.3}$$

$$\omega_R = \frac{(1+\rho)\,i}{1+\rho i}\omega_o. \tag{A.4}$$

The ratio i represents the variable we used for the parametric optimization process.

A.3 Torques analysis

Let's consider the reference system in Figure A.1. The rotation equilibrium equation is:

$$T_R + T_S + T_o = 0, \tag{A.5}$$

where T_S and T_R are the torques on the sun and on the ring, respectively. The power balance is represented by (Figure A.2):

$$\eta_{pd}\left(T_R\omega_R + T_S\omega_S\right) + T_o\omega_o = 0, \tag{A.6}$$

with η_{pg} the efficiency of the planetary gear. Eq. A.6 is correct for steady state conditions, but it is also a good approximation in dynamic conditions. In fact, it is possible to show that the inertia of the planetary gear is negligible with respect to the one of the vehicle.

A.3.1 Efficiency definition

In order to determine the efficiency of the planetary gear system, we used the model shown in Figure A.2.

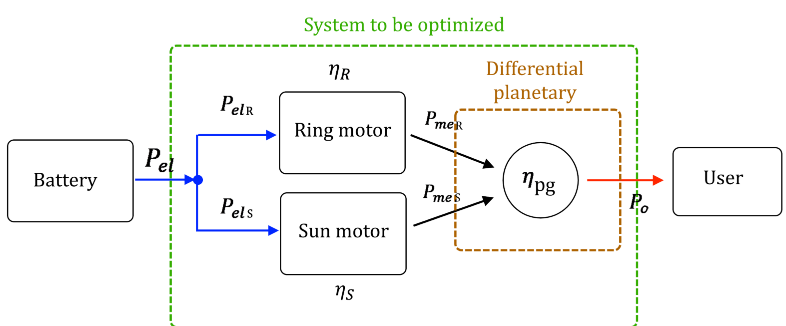

Figure A.2: Schematic of the system to be optimized: power flow with both motors supplying power [129].

In particular, by considering the same orientation for the speed and the torque, both the motors of the ring and the sun are supplying power, so the power at the carrier (P_o) is:

$$P_o = -\eta_{pg}\left(\eta_R P_{elR} + \eta_S P_{elS}\right) = -\eta_{tot} P_{el} = -\eta_{tot}\left(P_{elR} + P_{elS}\right), \tag{A.7}$$

where $P_{elR/S}$ is the electric power supplied by the ring/sun motor and $\eta_{R/S}$ is the efficiency of the ring/sun motor, defined as:

$$\eta_{R/S} = -\frac{P_{meR/S}}{P_{elR/S}}, \tag{A.8}$$

with $P_{meR/S}$ the mechanical power supplied by the first/second motor and $P_{elR/S}$ the electrical power supplied by the first/second motor. We can now express a general expression for the efficiency using equations A.7 and A.8.

$$\eta_{tot} = \eta_{pg}\frac{P_{meR} + P_{meS}}{\frac{P_{meR}}{\eta_R} + \frac{P_{meS}}{\eta_S}}. \tag{A.9}$$

In regenerative working condition, the regenerative efficiency would be written as:

$$\eta_{tot,reg} = \eta_{pg,reg}\frac{P_{meR}\eta_{R,reg} + P_{meS}\eta_{S,reg}}{P_{meR} + P_{meS}}, \tag{A.10}$$

with $\eta_{reg,R}$ and $\eta_{reg,S}$ the regenerative efficiencies of the ring and the sun motor, respectively.

A.4 Optimization and results

A.4.1 Optimization setup

Here we develop the idea of improving the efficiency performance of an electric vehicle that is meant to run in urban conditions. We want to show that, by using a planetary gear, we can achieve better performances in terms of efficiency with respect to a single motor drive directly connected to the wheels through a gear train. In order to do that, we want to optimize the speeds of the two motors connected to a planetary gear with the aim of maximizing the efficiency over each operative point (first step of the optimization). On a second step, we want to optimize the geometrical constraints on the planetary gear and the power constraints on the two motors connected to it with the aim of maximizing the average efficiency over an ECE-15 urban cycle (second step) like the one shown in Figure A.3a. The urban cycle contains information about the speed (proportional to the angular speed of the wheels, ω_o) and the power (P_o) required by the user.

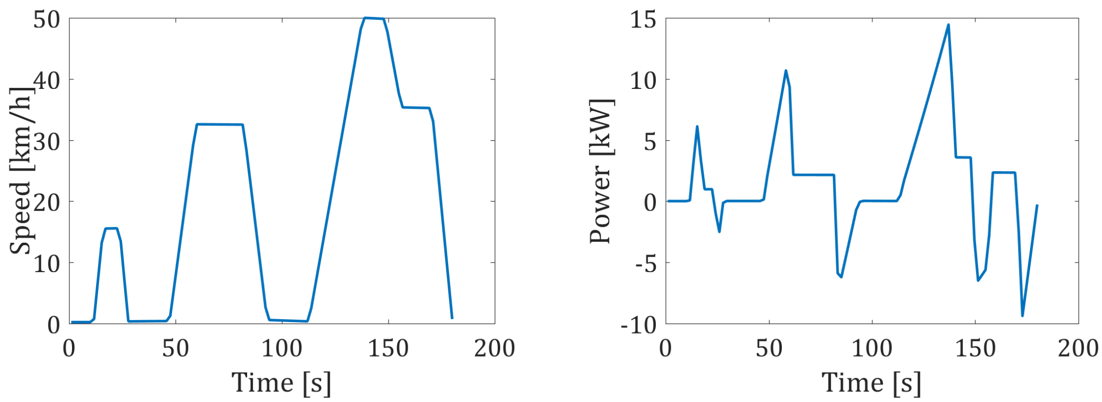

(a) (b)

Figure A.3: Speeds (a) and power (b) of a vehicle during a ECE-15 urban cycle [129].

In order to perform our optimization algorithm, we calculated the torque (T_o) to assure that the vehicle is running on the horizontal plane, by using the following equation [140] (Figure A.3b):

$$P_o = T_o\omega_o = \frac{1}{2}d_{air}C_xS\omega_0^3R^3 + M\dot{\omega}_o\omega_oR^2 + f_vMg\omega_oR, \tag{A.11}$$

with all the parameters defined in Table A.1. It is possible to demonstrate that the inertia of the motor could be neglected. For the optimization method, in this work the value of η_{pg} is evaluated as in [155, 156]. The proposed planetary gear has been optimized with the aim of maximizing the overall efficiency. In order to perform the optimization algorithm, we referred to the efficiency map shown in Figure A.4 for each of the electrical induction motors.

In particular, starting from data in Figure A.4, after a second order polynomial regression, we obtained the efficiency map shown in the colormap in Figure A.5. We

Parameter	Definition	Value
d_{air}	Air density	1.225 kg/m3
C_x	Aerodynamic drag coefficient	0.32
S	Frontal area	1.2 m^2
M	Vehicle mass	1500 kg
f_v	Rolling friction coefficient	0.01
R	Radius of the wheel	0.35 m
$T_{o,max}$	Maximum torque required by the user during urban cycle	585.2 Nm
$\omega_{o,max}$	Maximum angular velocity required by the user during urban cycle	39.68 rad/s
$P_{o,max}$	Maximum power required by the user during urban cycle	14.45 kW

Table A.1: Parameters of the vehicle and of the user requirements.

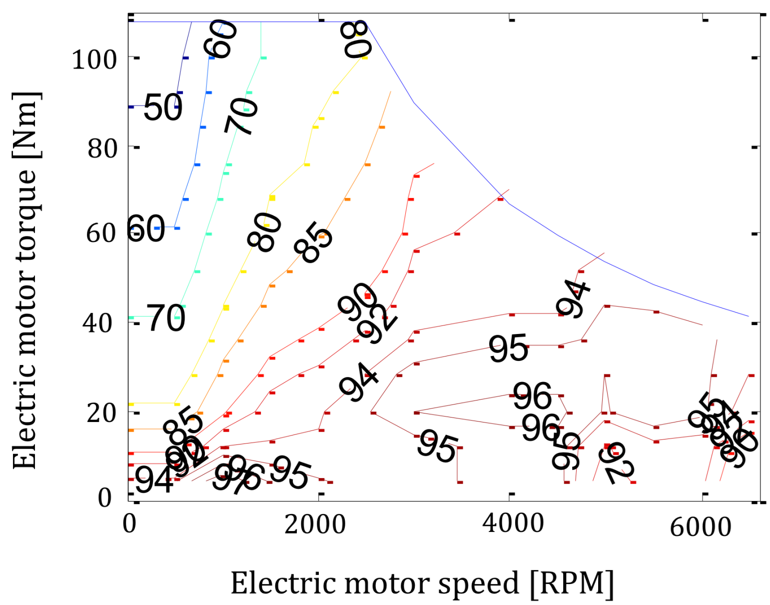

Figure A.4: Efficiency map of an electrical motor [140].

Coefficient	**Value**
a	1017
b	770
p00	94.01
p10	0.02059
p01	-0.08092
p20	-0.00002967
p11	0.0001241
p02	0.00001428

Table A.2: Coefficients of the efficiency map in Figure A.5.

can model such efficiency map using the following expression:

$$\eta_{R/S}\left(\omega_o, T_o\right) = \eta_0\left(\omega_o, T_o\right) =$$

$$\left[\begin{array}{l} p00 \; + \; p10\left(\frac{\omega_0}{\omega_{max}} \cdot a\right) + p01\left(\frac{T_o}{T_{omax}} \cdot b\right) + \\ +p20\left(\frac{\omega_0}{\omega_{max}} \cdot a\right)^2 \; + \; p11\left(\frac{\omega_0}{\omega_{max}} \cdot a\right)\left(\frac{T_o}{T_{omax}} \cdot b\right) \; + \; p02\left(\frac{T_o}{T_{omax}} \cdot b\right)^2 \end{array}\right] /100, \tag{A.12}$$

where the values of a, b and pij are defined in Table A.2.

The same efficiency map has been considered for the motors during power regeneration of power. We guess that the choice of the efficiency map will not affect the generality of the work, because the algorithm could be easily reused for different efficiency maps.

Without loss of generality, we will consider a 1500 kg electrical vehicle, modeled with the parameters shown in Table A.1. In order to make a fair comparison, we considered: case (A) of a single motor directly connected (after a gear train) to the wheels that can supply exactly the maximum torque and maximum power (and also satisfies the requirement on the maximum speed) required by the vehicle; case (B) of two motors connected to a planetary gear, able to supply the same total power of the single motor of the case A.

In Figure A.6a and A.6b, the working points (T_o, ω_o) of a user during the urban cycle proposed in Figure A.3a and A.3b are shown over the efficiency map.

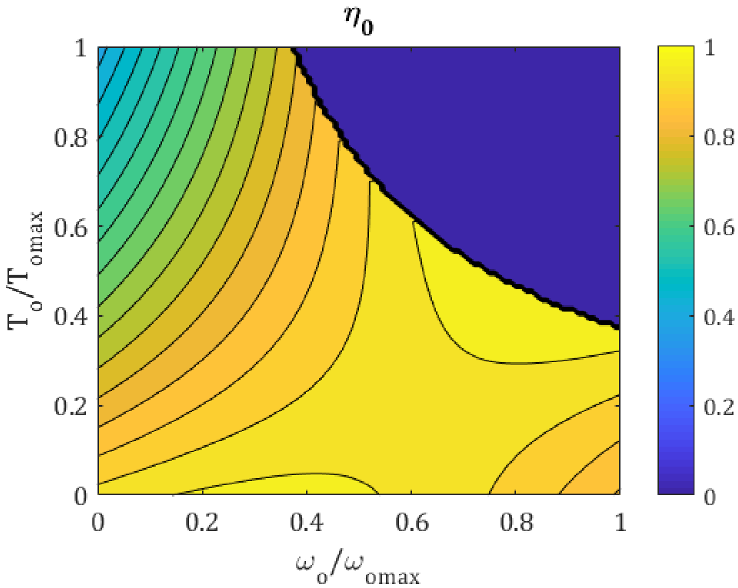

Figure A.5: Efficiency map of a standard electric motor [129].

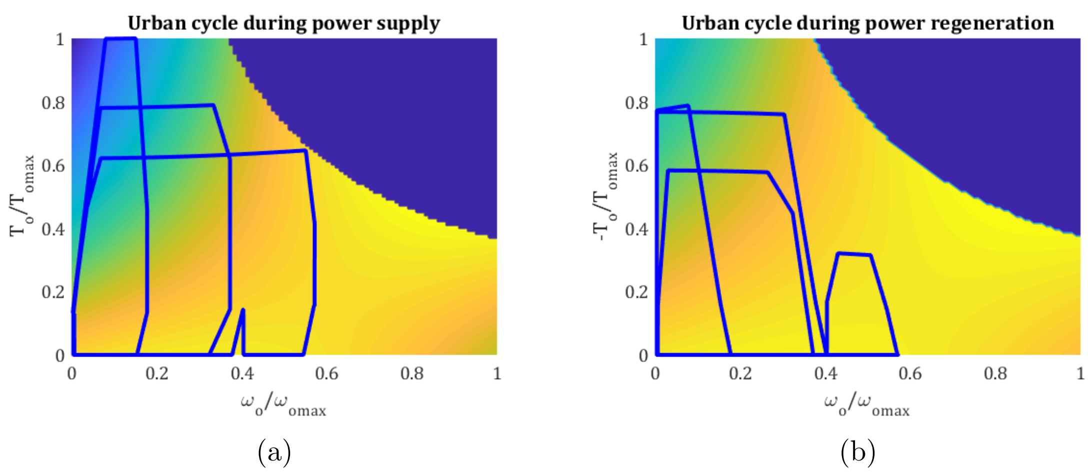

Figure A.6: Working points during an urban cycle over the efficiency map during supplying (a) and regeneration (b) of power [129].

A.5 Optimization algorithm and results

The optimization process has been performed in two steps: 1) Optimizing the ratio i to maximize the efficiency η_{tot} in every operating point (ω_o,T_o) for given values of ρ and ω_{maxR}. 2) Optimizing ρ and ω_{maxR} to maximize the average efficiency over an urban cycle (η_{cyc}).

A.5.1 First step

The first step of the optimization process has been performed by choosing, for each operative point (torque and speed of the user), the combination of speeds (in particular the ratio i between them) of the two motors in the planetary gear, which guarantees the best efficiency, for a fixed value of the planetary gear ratio ρ and for a fixed value of the maximum speed of the ring motor. The optimization function can be represented as:

$$\eta_{tot,max}\left(\omega_o, T_o\right) = \max\left\{\eta_{tot}\left(\omega_o, T_o, i\right)\right\}, \tag{A.13}$$

under the constraint in Equation A.2. For the regenerative part, it becomes:

$$\eta_{tot,reg,max}\left(\omega_o, T_o\right) = \max\left\{\eta_{tot,reg}\left(\omega_o, T_o, i\right)\right\}, \tag{A.14}$$

under the same constraint in Equation A.2. Algorithm 2 shows the pseudo-code for calculating $\eta_{tot,max}$.

Algorithm 2 Pseudo-code for calculating $\eta_{tot,max}$.

```
procedure RATIOOPT(ρ, ω_maxR, ω_maxS)
    for cycle on ω_0 do
        for cycle on T_o do
            for cycle on i do
                store η_tot(ω_o, T_o, i)
    return η_tot,max(ω_o, T_o) = max{η_tot(ω_o, T_o, i)}
```

Figure A.7a and A.7b show the difference between the efficiency map of the optimized system (η_{tot}) and the efficiency map of a single motor ensuring the same power supply (η_0). They are shown both in case of supply and regeneration of power. It is easy to see that the highest difference between the efficiency of the optimized planetary gear system and a single motor is obtained for low values of speeds and high values of torques. The maximum of the difference is around 0.25 and is reached for a torque form 80% and 100% and speeds around 15% and 20% of the maximum user speed.

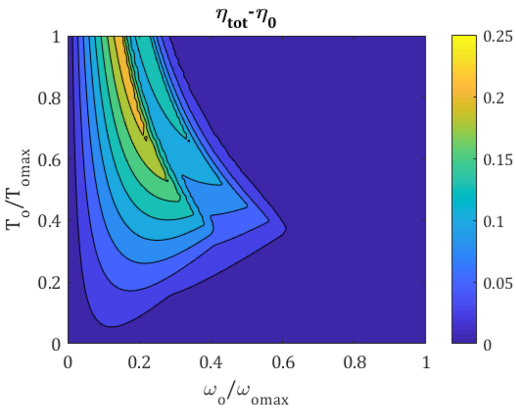

(a)

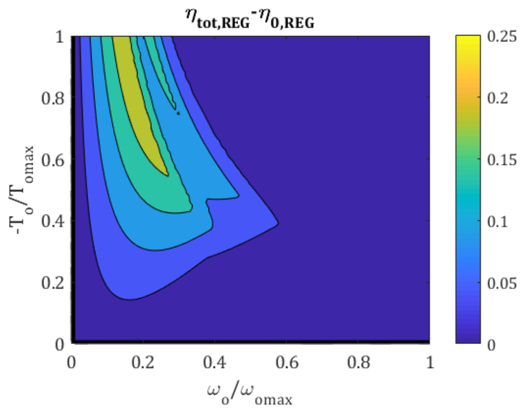

(b)

Figure A.7: Difference between the efficiency map of the optimized system and that of a single motor during power supply (a) and power regeneration (b) for ρ=3, ω_{maxR}=0.8$\omega_{o,max}$ and ω_{maxS}=1.6$\omega_{o,max}$ [129].

A.5.2 Second step

The maximization in Eqs. A.13 and A.14 can be repeated for different values of the planetary gear ratio ρ, combined with different values of the maximum speed of the ring motor to optimize the overall efficiency during an urban cycle. In particular, the values of the planetary gear ratio ρ and of the maximum speed of the ring motor (ω_{maxR}) have been chosen to maximize the energy efficiency over the urban cycle (η_{cyc}). The energy efficiency is defined as the ratio between the mechanical energy available for the user and the electrical energy request by the motors during the period of time defined by an urban cycle (u.c.):

$$\eta_{cyc} = \frac{\int_{u.c.} \omega_o(t) \cdot T_o(t)\ dt}{\int_{u.c.} \frac{\omega_o(t) \cdot T_o(t)}{\eta_{tot,max}(\omega_o(t), T_o(t))} dt}. \tag{A.15}$$

In particular, the planetary gear ratio ρ has been varied between 2 and 5 at step of 0.2. For the maximum speed of the ring motor (ω_{maxR}), five equidistant values have been chosen between $\omega_0/2$ and $\omega_0 \cdot \rho/(\rho+1)$ (which represents the maximum speed of the ring motor, corresponding to a null power of the sun motor) for every different value of ρ. It should be noticed that, once the maximum speed of the ring has been fixed (ω_{maxR}), the maximum speed of the sun (ω_{maxS}) is determined by the requirement of having the sum of the powers of the sun and the ring motors equal to the maximum power required by the user. The optimization algorithm is so defined by the following expression:

$$\eta_{cyc,max} = \max \{\eta_{cyc}(\rho, \omega_{maxR})\}. \tag{A.16}$$

Algorithm 3 shows the pseudo-code for calculating $\eta_{cyc,max}$.

Algorithm 3 Pseudo-code for calculating $\eta_{cyc,max}$.

procedure RHOOMEGAOPT
  for cycle on ρ **do**
    for cycle on ω_{maxR} **do**
      $\eta_{tot,max}(\omega_o, T_o) = \text{ratioOpt}(\rho, \omega_{maxR}, \omega_{maxS})$
      store $\eta_{cyc} = \frac{\int_{u.c.} \omega_o(t) \cdot T_o(t)\ dt}{\int_{u.c.} \frac{\omega_o(t) \cdot T_o(t)}{\eta_{tot,max}(\omega_o(t), T_o(t))} dt}$
  return $\eta_{cyc,max} = \max \{\eta_{cyc}(\rho, \omega_{maxR})\}$

Figure A.8 shows some of the values of ρ and ω_{maxR} that have been analysed during the second step of the optimization. It is evident that even varying ρ and ω_{maxR} over a wide range has a small effect over the average efficiency during the urban cycle. This guarantees a high robustness and flexibility over the nominal powers of motors and the planetary gear. The values of ω_{maxR}, ω_{maxS}, T_{maxR}, T_{maxS} and ρ which maximizes the average efficiency over the urban cycle are summarized in Table A.3. The results show that using two motors with the same efficiency map guarantees an overall efficiency over the urban cycle ($\eta_{cyc,max}$) of 90.13 %, with respect to an efficiency $\eta_{0,avg}$ of 82.43 % obtained in the case of a single motor with

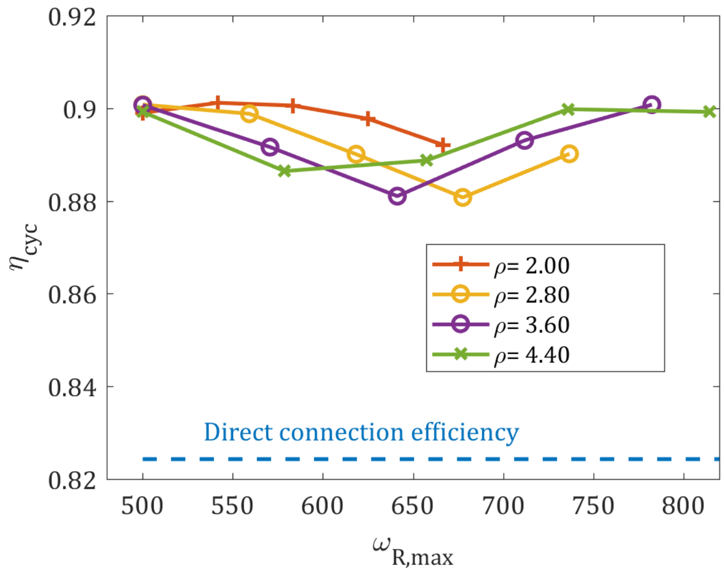

Figure A.8: η_{cyc} for different combinations of ρ and ω_{maxR} [129].

the same efficiency map of that in Figure A.5. A regeneration efficiency $\eta_{cyc,max,reg}$ of 89.76 % over the regenerative part of the urban cycle has been achieved with the proposed planetary gear system with respect to an efficiency $\eta_{0,avg,reg}$ of a single motor during the same urban cycle of 80.24 %. As shown, the best improvement of the proposed configuration is given for high values of torques and low values of speed, typical working conditions of a city vehicle. This is the reason why the average efficiency $\eta_{cyc,max}$, evaluated over an urban cycle (classically characterized by low speeds and high torques), is increased by 9.34 % with respect to a single motor of the same overall performances. The best improvement is obtained for the two motors with two nominal powers equal to 36 % (sun motor) and 64 % (ring motor) of the maximum power required by the vehicle.

A.6 Driving curves and power distribution

Figure A.9a and A.9b show the value of the speed of the sun and the ring motors allowing the maximization of the overall efficiency of the rotatory system, for the optimal values of $\rho = 4$, $\omega_{maxS} = 1.8$, $\omega_{o,max}$, $\omega_{maxR} = 0.8\ \omega_{o,max}$.

Parameter	Optimization Value
ρ	4
$\eta_{0,avg}$	0.8243
$\eta_{cyc,max}$	0.9013
$\eta_{0,avg,reg}$	0.8024
$\eta_{cyc,max,reg}$	0.8976
ω_{maxS}	1.8 $\omega_{o,max}$
T_{maxS}	0.2 $T_{o,max}$
P_{maxS}	0.36 $P_{o,max}$
ω_{maxR}	0.8 $\omega_{o,max}$
T_{maxR}	0.8 $T_{o,max}$
P_{maxR}	0.64 $T_{o,max}$

Table A.3: Parameters optimizing the overall averaged efficiency.

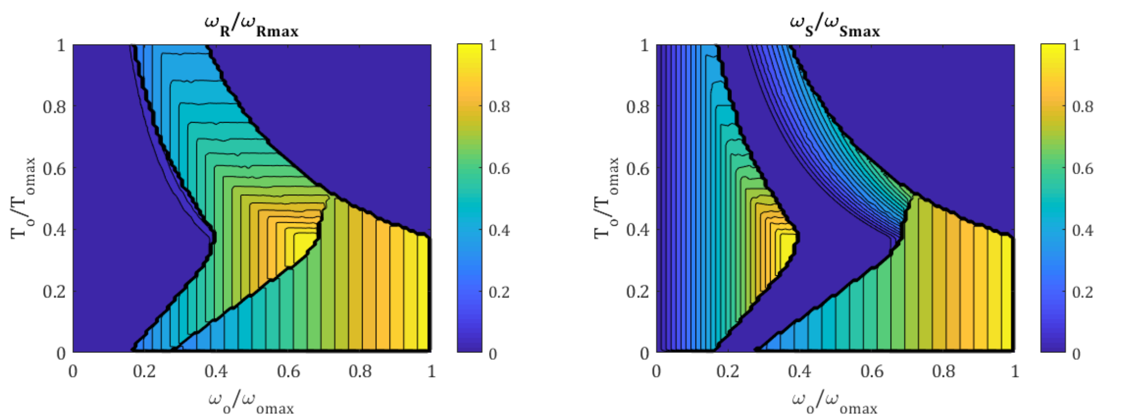

(a) (b)

Figure A.9: Speed of the motor of the ring (a) and the sun (b) maximizing the overall efficiency during power supply [129].

The angular speeds (ω_R, ω_S) for each working point (T_o, ω_o) represent the values of the optimized system. It is evident that for low values of speed of the vehicle, the ring motor is the only one that is rotating, whereas there is a region for intermediate values of speed, where the sun motor supplies the majority of the required power. For the maximum values of the speed of the vehicle, both motors work simultaneously.

This is due to the fact that, as designed, the sum of the power of the two motors is equal to the maximum power required by the user. In Figure A.10 it is possible to see the distribution of the power during the urban cycle between the sun and the ring motors.

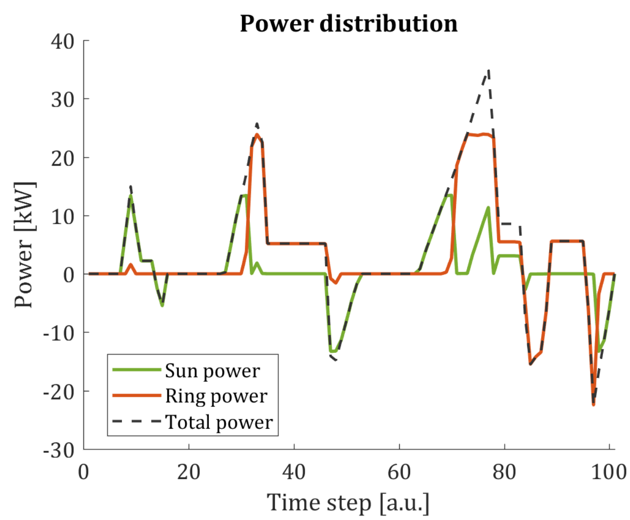

Figure A.10: Power distribution of the optimized system over the sun and the ring motors [129].

The power distribution during the urban cycle shows that during power supplying of power the sun motor is the only working for low values of required power and high torque. For high values of speed and low values of torque (constant high speed) the ring motor is the only motor supplying power. As the required power reaches the 80 % - 90 % of the maximum power, both the motors work together.

A.6.1 Final considerations

In this study a planetary gear which combines the torques and the velocities of two electrical motors in electric vehicles has been proposed. This kind of system, through an optimization algorithm, can obtain an average efficiency during the supply of power of 90.13 %, with respect to that of 82.43 % of a single motor guaranteeing the same total power, same maximum torque and maximum velocity. During regeneration, a regeneration efficiency of 89.76 % has been obtained with respect to one of

80.24 % of a single motor. The efficiency maps of the optimized system show that the best improvement is achieved for high values of the torques and low values of the speeds. This means that this kind of configuration represents a perfect solution for a city electric vehicle or every kind of motor usually working with high values of torques and low levels of speed. The solution we proposed is aimed at improving the energetic efficiency of electrical motors when rapidly changing operating conditions are required by the vehicle. However, the optimized values for the gear ratio of the planetary gear and the maximum speeds and torques of the motors can be easily found for any type of cycle with the optimization algorithm here proposed. In this sense this study could represent a relevant framework for improving the efficiency performance of electric vehicle.

Bibliography

[1] M. Armenise, C. Ciminelli, F. Dell'Olio, and V. M. N. Passaro, *Advances in gyroscope technologies*. Berlin Heidelberg: Springer, 2011.

[2] V. M. N. Passaro, A. Cuccovillo, L. Vaiani, M. D. Carlo, and C. E. Campanella, "Gyroscope technology and applications: A review in the industrial perspective," *Sensors*, vol. 17, p. 2284, Oct. 2017.

[3] W. M. Macek and D. T. M. Davis, "Rotation rate sensing with traveling-wave ring lasers," *Applied Physics Letters*, vol. 2, pp. 67–68, Feb. 1963.

[4] S. Ezekiel and H. J. Arditty, "Fiber-optic rotation sensors. tutorial review," in *Springer Series in Optical Sciences*, pp. 2–26, Springer Berlin Heidelberg, 1982.

[5] H. Zhang, J. Chen, J. Jin, J. Lin, L. Zhao, Z. Bi, A. Huang, and Z. Xiao, "On-chip modulation for rotating sensing of gyroscope based on ring resonator coupled with mach-zehnder interferometer," *Scientific Reports*, vol. 6, Jan. 2016.

[6] T. Zhang, G. Qian, Y.-Y. Wang, X.-J. Xue, F. Shan, R.-Z. Li, J.-Y. Wu, and X.-Y. Zhang, "Integrated optical gyroscope using active long-range surface plasmon-polariton waveguide resonator," *Scientific Reports*, vol. 4, Jan. 2014.

[7] J. Li, M.-G. Suh, and K. Vahala, "Microresonator brillouin gyroscope," *Optica*, vol. 4, p. 346, Mar. 2017.

[8] S. Srinivasan, R. Moreira, D. Blumenthal, and J. E. Bowers, "Design of integrated hybrid silicon waveguide optical gyroscope," *Optics Express*, vol. 22, p. 24988, Oct. 2014.

[9] J. Chen, H. Zhang, J. Jin, J. Lin, L. Zhao, Z. Bi, A. Huang, and Z. Xiao, "Miniaturized optical gyroscope using active three-dimensional vertically coupled resonators," *Optical Engineering*, vol. 54, p. 107106, Oct. 2015.

[10] H. Zhang, J. Liu, J. Lin, W. Li, X. Xue, A. Huang, and Z. Xiao, "On-chip tunable dispersion in a ring laser gyroscope for enhanced rotation sensing," *Applied Physics A*, vol. 122, Apr. 2016.

[11] J. Ren, H. Hodaei, G. Harari, A. U. Hassan, W. Chow, M. Soltani, D. Christodoulides, and M. Khajavikhan, "Ultrasensitive micro-scale parity-time-symmetric ring laser gyroscope," *Optics Letters*, vol. 42, p. 1556, Apr. 2017.

[12] M. De Carlo, F. De Leonardis, and V. M. N. Passaro, "Design rules of a microscale PT-symmetric optical gyroscope using group IV platform," *Journal of Lightwave Technology*, vol. 36, pp. 3261–3268, Aug. 2018.

[13] M. De Carlo, F. D. Leonardis, L. Lamberti, and V. M. N. Passaro, "High-sensitivity real-splitting anti-PT-symmetric microscale optical gyroscope," *Optics Letters*, vol. 44, p. 3956, Aug. 2019.

[14] F. Marquardt and S. Girvin, "Optomechanics," *Physics*, vol. 2, p. 40, May 2009.

[15] J. C. Maxwell, *A Treatise on electricity and magnetism.* Oxford: Clarendon Press, 1873.

[16] P. Lebedew, "Untersuchungen über die druckkräfte des lichtes," *Annalen der Physik*, vol. 311, no. 11, pp. 433–458, 1901.

[17] V. B. Braginskiǐ and A. B. Manukin, "Ponderomotive Effects of Electromagnetic Radiation," *Soviet Journal of Experimental and Theoretical Physics*, vol. 25, p. 653, Oct. 1967.

[18] A. Ashkin, “Trapping of atoms by resonance radiation pressure,” *Physical Review Letters*, vol. 40, pp. 729–732, Mar. 1978.

[19] T. Hänsch and A. Schawlow, “Cooling of gases by laser radiation,” *Optics Communications*, vol. 13, pp. 68–69, Jan. 1975.

[20] D. J. Wineland and W. M. Itano, “Laser cooling,” *Physics Today*, vol. 40, pp. 34–40, June 1987.

[21] S. Stenholm, “The semiclassical theory of laser cooling,” *Reviews of Modern Physics*, vol. 58, pp. 699–739, July 1986.

[22] T. Corbitt, Y. Chen, E. Innerhofer, H. Müller-Ebhardt, D. Ottaway, H. Rehbein, D. Sigg, S. Whitcomb, C. Wipf, and N. Mavalvala, “An all-optical trap for a gram-scale mirror,” *Physical Review Letters*, vol. 98, p. 150802, Apr. 2007.

[23] C. H. Metzger and K. Karrai, “Cavity cooling of a microlever,” *Nature*, vol. 432, pp. 1002–1005, Dec. 2004.

[24] S. Gigan, H. R. Böhm, M. Paternostro, F. Blaser, G. Langer, J. B. Hertzberg, K. C. Schwab, D. Bäuerle, M. Aspelmeyer, and A. Zeilinger, “Self-cooling of a micromirror by radiation pressure,” *Nature*, vol. 444, pp. 67–70, Nov. 2006.

[25] O. Arcizet, P.-F. Cohadon, T. Briant, M. Pinard, and A. Heidmann, “Radiation-pressure cooling and optomechanical instability of a micromirror,” *Nature*, vol. 444, pp. 71–74, Nov. 2006.

[26] T. Carmon, H. Rokhsari, L. Yang, T. J. Kippenberg, and K. J. Vahala, “Temporal behavior of radiation-pressure-induced vibrations of an optical microcavity phonon mode,” *Physical Review Letters*, vol. 94, p. 223902, June 2005.

[27] A. Schliesser, P. Del’Haye, N. Nooshi, K. J. Vahala, and T. J. Kippenberg, “Radiation pressure cooling of a micromechanical oscillator using dynamical backaction,” *Physical Review Letters*, vol. 97, p. 243905, Dec. 2006.

[28] J. D. Thompson, B. M. Zwickl, A. M. Jayich, F. Marquardt, S. M. Girvin, and J. G. E. Harris, “Strong dispersive coupling of a high-finesse cavity to a micromechanical membrane,” *Nature*, vol. 452, pp. 72–75, Mar. 2008.

[29] C. Metzger, M. Ludwig, C. Neuenhahn, A. Ortlieb, I. Favero, K. Karrai, and F. Marquardt, "Self-induced oscillations in an optomechanical system driven by bolometric backaction," *Physical Review Letters*, vol. 101, p. 133903, Sept. 2008.

[30] M. L. Povinelli, S. G. Johnson, M. Loncar, M. Ibanescu, E. J. Smythe, F. Capasso, and J. D. Joannopoulos, "High-Q enhancement of attractive and repulsive optical forces between coupled whispering-gallery-mode resonators," *Optics Express*, vol. 13, no. 20, p. 8286, 2005.

[31] M. Eichenfield, C. P. Michael, R. Perahia, and O. Painter, "Actuation of micro-optomechanical systems via cavity-enhanced optical dipole forces," *Nature Photonics*, vol. 1, pp. 416–422, July 2007.

[32] P. T. Rakich, M. A. Popović, M. Soljačić, and E. P. Ippen, "Trapping, corralling and spectral bonding of optical resonances through optically induced potentials," *Nature Photonics*, vol. 1, pp. 658–665, Nov. 2007.

[33] A. Mizrahi and L. Schächter, "Two-slab all-optical spring," *Optics Letters*, vol. 32, p. 692, Feb. 2007.

[34] M. Notomi, H. Taniyama, S. Mitsugi, and E. Kuramochi, "Optomechanical wavelength and energy conversion in high-Q Double-layer cavities of photonic crystal slabs," *Physical Review Letters*, vol. 97, p. 023903, July 2006.

[35] M. L. Povinelli, M. Lončar, M. Ibanescu, E. J. Smythe, S. G. Johnson, F. Capasso, and J. D. Joannopoulos, "Evanescent-wave bonding between optical waveguides," *Optics Letters*, vol. 30, p. 3042, Nov. 2005.

[36] T. J. Kippenberg, H. Rokhsari, T. Carmon, A. Scherer, and K. J. Vahala, "Analysis of radiation-pressure induced mechanical oscillation of an optical microcavity," *Physical Review Letters*, vol. 95, p. 033901, July 2005.

[37] M. A. Popovic and P. T. Rakich, "Optonanomechanical self-adaptive photonic devices based on light forces: a path to robust high-index-contrast nanophotonic circuits," in *Optoelectronic Integrated Circuits XI* (L. A. Eldada and

E.-H. Lee, eds.), vol. 7219, pp. 74 – 84, International Society for Optics and Photonics, SPIE, 2009.

[38] W. A. Shelton, K. D. Bonin, and T. G. Walker, "Nonlinear motion of optically torqued nanorods," *Physical Review E*, vol. 71, p. 036204, Mar. 2005.

[39] S. H. Simpson and S. Hanna, "Holographic optical trapping of microrods and nanowires," *Journal of the Optical Society of America A*, vol. 27, p. 1255, May 2010.

[40] S. Kuhn, A. Kosloff, B. A. Stickler, F. Patolsky, K. Hornberger, M. Arndt, and J. Millen, "Full rotational control of levitated silicon nanorods," *Optica*, vol. 4, p. 356, Mar. 2017.

[41] M. Liu, T. Zentgraf, Y. Liu, G. Bartal, and X. Zhang, "Light-driven nanoscale plasmonic motors," *Nature Nanotechnology*, vol. 5, pp. 570–573, July 2010.

[42] S. Lin and K. B. Crozier, "Trapping-assisted sensing of particles and proteins using on-chip optical microcavities," *ACS Nano*, vol. 7, pp. 1725–1730, Jan. 2013.

[43] K. Kim, X. Xu, J. Guo, and D. L. Fan, "Ultrahigh-speed rotating nanoelectromechanical system devices assembled from nanoscale building blocks," *Nature Communications*, vol. 5, p. 3632, May 2014.

[44] Y. Geng, J. Tan, Y. Cao, Y. Zhao, Z. Liu, and W. Ding, "Giant and tunable optical torque for micro-motors by increased force arm and resonantly enhanced force," *Scientific Reports*, vol. 8, p. 2819, Dec. 2018.

[45] P. T. Rakich, M. A. Popovic, and Z. Wang, "General treatment of optical forces and potentials in mechanically variable photonic systems," *Optics Express*, vol. 17, p. 18116, Sept. 2009.

[46] M. De Carlo, F. De Leonardis, L. Lamberti, and V. M. N. Passaro, "Generalized modeling of optomechanical forces applied to PT-symmetric optical microscale resonators," *Journal of Lightwave Technology*, vol. 37, pp. 2178–2184, May 2019.

[47] M. D. Carlo, F. D. Leonardis, L. Lamberti, and V. M. Passaro, "Dynamics of optomechanically coupled suspended silicon waveguides," *Sensors and Actuators A: Physical*, vol. 301, p. 111714, Jan. 2020.

[48] L. B. Kreuzer, "The physics of signal generation and detection," in *Optoacoustic Spectroscopy and Detection*, pp. 1–25, Elsevier, 1977.

[49] P. Patimisco, G. Scamarcio, F. Tittel, and V. Spagnolo, "Quartz-enhanced photoacoustic spectroscopy: A review," *Sensors*, vol. 14, pp. 6165–6206, Mar. 2014.

[50] A. A. Kosterev, Y. A. Bakhirkin, R. F. Curl, and F. K. Tittel, "Quartz-enhanced photoacoustic spectroscopy," *Optics Letters*, vol. 27, p. 1902, Nov. 2002.

[51] A. A. Kosterev, F. K. Tittel, D. V. Serebryakov, A. L. Malinovsky, and I. V. Morozov, "Applications of quartz tuning forks in spectroscopic gas sensing," *Review of Scientific Instruments*, vol. 76, p. 043105, Apr. 2005.

[52] Y. Ma, R. Lewicki, M. Razeghi, and F. K. Tittel, "QEPAS based ppb-level detection of CO and N_2O using a high power CW DFB-QCL," *Optics Express*, vol. 21, p. 1008, Jan. 2013.

[53] V. Spagnolo, A. A. Kosterev, L. Dong, R. Lewicki, and F. K. Tittel, "NO trace gas sensor based on quartz-enhanced photoacoustic spectroscopy and external cavity quantum cascade laser," *Applied Physics B*, vol. 100, pp. 125–130, Mar. 2010.

[54] J. A. Harrington, *Infrared Fibers and Their Applications*. SPIE, Jan. 2004.

[55] A. Sampaolo, P. Patimisco, J. M. Kriesel, F. K. Tittel, G. Scamarcio, and V. Spagnolo, "Single mode operation with mid-IR hollow fibers in the range 51-105 μm," *Optics Express*, vol. 23, p. 195, Jan. 2015.

[56] M. Giglio, A. S. Pietro Patimisco, J. M. Kriesel, F. K. Tittel, and V. Spagnolo, "Low-loss and single-mode tapered hollow-core waveguides optically coupled with interband and quantum cascade lasers," *Optical Engineering*, vol. 57, p. 1, Aug. 2017.

[57] A. Sampaolo, P. Patimisco, M. Giglio, L. Chieco, G. Scamarcio, F. K. Tittel, and V. Spagnolo, "Highly sensitive gas leak detector based on a quartz-enhanced photoacoustic SF6 sensor," *Optics Express*, vol. 24, p. 15872, July 2016.

[58] H. Wu, L. Dong, X. Yin, A. Sampaolo, P. Patimisco, W. Ma, L. Zhang, W. Yin, L. Xiao, V. Spagnolo, and S. Jia, "Atmospheric CH4 measurement near a landfill using an ICL-based QEPAS sensor with v-t relaxation self-calibration," *Sensors and Actuators B: Chemical*, vol. 297, p. 126753, Oct. 2019.

[59] Y. Ma, "Review of recent advances in QEPAS-based trace gas sensing," *Applied Sciences*, vol. 8, p. 1822, Oct. 2018.

[60] F. Sgobba, G. Menduni, S. D. Russo, A. Sampaolo, P. Patimisco, M. Giglio, E. Ranieri, V. M. N. Passaro, F. K. Tittel, and V. Spagnolo, "Quartz-enhanced photoacoustic detection of ethane in the near-IR exploiting a highly performant spectrophone," *Applied Sciences*, vol. 10, p. 2447, Apr. 2020.

[61] S. Csutak, W. Li, A. Sampaolo, and G. Ham, "Photoacoustic gas detection," 2019.

[62] M. D. Carlo, G. Menduni, A. Sampaolo, F. D. Leonardis, V. Spagnolo, and V. M. N. Passaro, "Modeling and design of a semi-integrated QEPAS sensor," *Journal of Lightwave Technology*, 2020. Published online on the 13th October 2020.

[63] H. Geng, *Semiconductor manufacturing handbook*. New York: McGraw-Hill, 2005.

[64] C. Mack, *Fundamental principles of optical lithography : the science of microfabrication*. Chichester, West Sussex, England Hoboken, NJ, USA: Wiley, 2007.

[65] G. Brewer, *Electron-beam technology in microelectronic fabrication*. New York: Academic Press, 1980.

[66] H. Rembrandt, *Rembrandt, experimental etcher: exhibition catalogue*. New York: Hacker Art Books, 1988.

[67] N. P. Mahalik, *Micromanufacturing and nanotechnology.* Berlin New York: Springer, 2006.

[68] P. J. French and P. M. Sarro, "Micromachining technology," in *MEMS: A Practical Guide to Design, Analysis, and Applications*, pp. 805–851, Springer Berlin Heidelberg, 2006.

[69] C. A. Volkert and A. M. Minor, "Focused ion beam microscopy and micromachining," *MRS Bulletin*, vol. 32, no. 5, p. 389–399, 2007.

[70] G. Sagnac, "Effet tourbillonnaire optique. la circulation de l'éther lumineux dans un interférographe tournant," *Journal de Physique Théorique et Appliquée*, vol. 4, no. 1, pp. 177–195, 1914.

[71] C. M. Bender and S. Boettcher, "Real spectra in non-hermitian hamiltonians HavingPTSymmetry," *Physical Review Letters*, vol. 80, pp. 5243–5246, June 1998.

[72] C. M. Bender, S. Boettcher, and P. N. Meisinger, "PT-symmetric quantum mechanics," *Journal of Mathematical Physics*, vol. 40, pp. 2201–2229, May 1999.

[73] C. E. Rüter, K. G. Makris, R. El-Ganainy, D. N. Christodoulides, M. Segev, and D. Kip, "Observation of parity–time symmetry in optics," *Nature Physics*, vol. 6, pp. 192–195, Jan. 2010.

[74] B. Peng, Ş. K. Özdemir, F. Lei, F. Monifi, M. Gianfreda, G. L. Long, S. Fan, F. Nori, C. M. Bender, and L. Yang, "Parity–time-symmetric whispering-gallery microcavities," *Nature Physics*, vol. 10, pp. 394–398, Apr. 2014.

[75] S. Zhang, Z. Yong, Y. Zhang, and S. He, "Parity-time symmetry breaking in coupled nanobeam cavities," *Scientific Reports*, vol. 6, Apr. 2016.

[76] S. Klaiman, U. Günther, and N. Moiseyev, "Visualization of branch points inPT-symmetric waveguides," *Physical Review Letters*, vol. 101, Aug. 2008.

[77] A. Guo, G. J. Salamo, D. Duchesne, R. Morandotti, M. Volatier-Ravat, V. Aimez, G. A. Siviloglou, and D. N. Christodoulides, "Observation ofPT-symmetry breaking in complex optical potentials," *Physical Review Letters*, vol. 103, Aug. 2009.

[78] A. Regensburger, C. Bersch, M.-A. Miri, G. Onishchukov, D. N. Christodoulides, and U. Peschel, "Parity–time synthetic photonic lattices," *Nature*, vol. 488, pp. 167–171, Aug. 2012.

[79] H. Benisty, A. Degiron, A. Lupu, A. D. Lustrac, S. Chénais, S. Forget, M. Besbes, G. Barbillon, A. Bruyant, S. Blaize, and G. Lérondel, "Implementation of PT symmetric devices using plasmonics: principle and applications," *Optics Express*, vol. 19, p. 18004, Aug. 2011.

[80] M. Brandstetter, M. Liertzer, C. Deutsch, P. Klang, J. Schöberl, H. E. Türeci, G. Strasser, K. Unterrainer, and S. Rotter, "Reversing the pump dependence of a laser at an exceptional point," *Nature Communications*, vol. 5, June 2014.

[81] V. K. B. Kota, *Embedded random matrix ensembles in quantum physics*. Cham: Springer, 2014.

[82] B. Little, S. Chu, H. Haus, J. Foresi, and J.-P. Laine, "Microring resonator channel dropping filters," *Journal of Lightwave Technology*, vol. 15, pp. 998–1005, June 1997.

[83] C. M. Bender, "PT symmetry in quantum physics: From a mathematical curiosity to optical experiments," *Europhysics News*, vol. 47, pp. 17–20, Mar. 2016.

[84] P. Moontragoon, R. A. Soref, and Z. Ikonic, "The direct and indirect bandgaps of unstrained SixGe1-x-ySnyand their photonic device applications," *Journal of Applied Physics*, vol. 112, p. 073106, Oct. 2012.

[85] R. Soref, "Silicon-based silicon–germanium–tin heterostructure photonics," *Philosophical Transactions of the Royal Society A: Mathematical, Physical and Engineering Sciences*, vol. 372, p. 20130113, Mar. 2014.

[86] G.-E. Chang, S.-W. Chang, and S. L. Chuang, "Strain-balanced Ge(z)Sn(1-z)–Si(x)Ge(y)Sn(1-x-y) multiple-quantum-well lasers," *IEEE Journal of Quantum Electronics*, vol. 46, pp. 1813–1820, Dec. 2010.

[87] B. Troia, F. D. Leonardis, and V. M. N. Passaro, "Generalized modelling for the design of guided-wave optical directional couplers," *Optics Letters*, vol. 39, p. 1161, Feb. 2014.

[88] Y. Choi, C. Hahn, J. W. Yoon, and S. H. Song, "Observation of an anti-PT-symmetric exceptional point and energy-difference conserving dynamics in electrical circuit resonators," *Nature Communications*, vol. 9, jun 2018.

[89] F. Yang, Y.-C. Liu, and L. You, "Anti- PT symmetry in dissipatively coupled optical systems," *Physical Review A*, vol. 96, Nov. 2017.

[90] L. Ge and H. E. Türeci, "AntisymmetricPT-photonic structures with balanced positive- and negative-index materials," *Physical Review A*, vol. 88, Nov. 2013.

[91] L. Ge, "Symmetry-protected zero-mode laser with a tunable spatial profile," *Physical Review A*, vol. 95, Feb. 2017.

[92] S. Ke, D. Zhao, J. Liu, Q. Liu, Q. Liao, B. Wang, and P. Lu, "Topological bound modes in anti-PT-symmetric optical waveguide arrays," *Optics Express*, vol. 27, p. 13858, Apr. 2019.

[93] S. Ke, D. Zhao, Q. Liu, S. Wu, B. Wang, and P. Lu, "Optical imaginary directional couplers," *Journal of Lightwave Technology*, vol. 36, pp. 2510–2516, June 2018.

[94] C. M. Gentry and M. A. Popović, "Dark state lasers," *Optics Letters*, vol. 39, p. 4136, July 2014.

[95] H. Hodaei, A. U. Hassan, W. E. Hayenga, M. A. Miri, D. N. Christodoulides, and M. Khajavikhan, "Dark-state lasers: mode management using exceptional points," *Optics Letters*, vol. 41, p. 3049, June 2016.

[96] W. Langbein, "No exceptional precision of exceptional-point sensors," *Physical Review A*, vol. 98, Aug. 2018.

[97] H.-K. Lau and A. A. Clerk, “Fundamental limits and non-reciprocal approaches in non-hermitian quantum sensing,” *Nature Communications*, vol. 9, Oct. 2018.

[98] H. Haus, *Waves and fields in optoelectronics*. Englewood Cliffs, NJ: Prentice-Hall, 1984.

[99] Y. Zhang, T. Mei, and D. H. Zhang, “Temporal coupled-mode theory of ring–bus–ring mach–zehnder interferometer,” *Applied Optics*, vol. 51, p. 504, Jan. 2012.

[100] B. S. Ryvkin, E. A. Avrutin, and J. T. Kostamovaara, “Strong doping of then-optical confinement layer for increasing output power of high- power pulsed laser diodes in the eye safe wavelength range,” *Semiconductor Science and Technology*, vol. 32, p. 125008, Oct. 2017.

[101] J. Leuthold, M. Mayer, J. Eckner, G. Guekos, H. Melchior, and C. Zellweger, “Material gain of bulk 1.55 um InGaAsP/InP semiconductor optical amplifiers approximated by a polynomial model,” *Journal of Applied Physics*, vol. 87, pp. 618–620, Jan. 2000.

[102] J. P. Gordon, “Radiation forces and momenta in dielectric media,” *Physical Review A*, vol. 8, pp. 14–21, July 1973.

[103] D. Griffiths, *Introduction to electrodynamics*. Cambridge, United Kingdom New York, NY: Cambridge University Press, 2017.

[104] A. Hardy and W. Streifer, “Coupled mode theory of parallel waveguides,” *Journal of Lightwave Technology*, vol. 3, no. 5, pp. 1135–1146, 1985.

[105] H. Nishihara, *Optical integrated circuits*. New York: McGraw-Hill Book Co, 1989.

[106] G. Liu and S. S. Quek, *The Finite Element Method: A Practical Course*. Butterworth-Heinemann, 2013.

[107] J. Ma and M. L. Povinelli, “Applications of optomechanical effects for on-chip manipulation of light signals,” *Current Opinion in Solid State and Materials Science*, vol. 16, pp. 82–90, apr 2012.

[108] T. Veijola, H. Kuisma, J. Lahdenperä, and T. Ryhänen, "Equivalent-circuit model of the squeezed gas film in a silicon accelerometer," *Sensors and Actuators A: Physical*, vol. 48, pp. 239–248, may 1995.

[109] Y. Sun, M. Bao, H. Yang, and Y. Huang, "Modified reynolds equation for squeeze-film air damping of slotted plates in mems devices," *Pan Tao Ti Hsueh Pao/Chinese Journal of Semiconductors*, vol. 27, pp. 473–477, 03 2006.

[110] D. Leith, "Drag on nonspherical objects," *Aerosol Science and Technology*, vol. 6, pp. 153–161, jan 1987.

[111] J. Starr, "Squeeze-film damping in solid-state accelerometers," in *IEEE 4th Technical Digest on Solid-State Sensor and Actuator Workshop*, IEEE, 1990.

[112] H. Cai, K. J. Xu, A. Q. Liu, Q. Fang, M. B. Yu, G. Q. Lo, and D. L. Kwong, "Nano-opto-mechanical actuator driven by gradient optical force," *Applied Physics Letters*, vol. 100, p. 013108, jan 2012.

[113] T. F. D. Fernandes, C. M. K. C. Carvalho, P. S. S. Guimaraes, B. R. A. Neves, and P.-L. de Assis, "Center-of-mass acceleration in coupled nanowaveguides due to transverse optical beating force," *Journal of Lightwave Technology*, vol. 36, pp. 1608–1614, may 2018.

[114] H. Nishihara, *Optical Integrated Circuits*. McGraw-Hill Professional, jan 1989.

[115] G. A. West, J. J. Barrett, D. R. Siebert, and K. V. Reddy, "Photoacoustic spectroscopy," *Review of Scientific Instruments*, vol. 54, pp. 797–817, July 1983.

[116] P. Patimisco, A. Sampaolo, L. Dong, F. K. Tittel, and V. Spagnolo, "Recent advances in quartz enhanced photoacoustic sensing," *Applied Physics Reviews*, vol. 5, p. 011106, Mar. 2018.

[117] P. Patimisco, A. Sampaolo, H. Zheng, L. Dong, F. K. Tittel, and V. Spagnolo, "Quartz–enhanced photoacoustic spectrophones exploiting custom tuning forks: a review," *Advances in Physics: X*, vol. 2, pp. 169–187, Dec. 2016.

[118] L. Dong, A. A. Kosterev, D. Thomazy, and F. K. Tittel, "QEPAS spectrophones: design, optimization, and performance," *Applied Physics B*, vol. 100, pp. 627–635, May 2010.

[119] K. Liu, X. Guo, H. Yi, W. Chen, W. Zhang, and X. Gao, "Off-beam quartz-enhanced photoacoustic spectroscopy," *Optics Letters*, vol. 34, p. 1594, May 2009.

[120] H. Zheng, L. Dong, H. Wu, X. Yin, L. Xiao, S. Jia, R. F. Curl, and F. K. Tittel, "Application of acoustic micro-resonators in quartz-enhanced photoacoustic spectroscopy for trace gas analysis," *Chemical Physics Letters*, vol. 691, pp. 462–472, Jan. 2018.

[121] Z. Zhou, B. Yin, and J. Michel, "On-chip light sources for silicon photonics," *Light: Science & Applications*, vol. 4, pp. e358–e358, Nov. 2015.

[122] V. Passaro, C. Tullio, B. Troia, M. Notte, G. Giannoccaro, and F. Leonardis, "Recent advances in integrated photonic sensors," *Sensors*, vol. 12, pp. 15558–15598, Nov. 2012.

[123] P. Yoh-Han, *Optoacoustic spectroscopy and detection.* Academic Press, nov 1977.

[124] S. A. Miller, M. Yu, X. Ji, A. G. Griffith, J. Cardenas, A. L. Gaeta, and M. Lipson, "Low-loss silicon platform for broadband mid-infrared photonics," *Optica*, vol. 4, p. 707, June 2017.

[125] L. Rothman, I. Gordon, Y. Babikov, A. Barbe, D. C. Benner, P. Bernath, M. Birk, L. Bizzocchi, V. Boudon, L. Brown, A. Campargue, K. Chance, E. Cohen, L. Coudert, V. Devi, B. Drouin, A. Fayt, J.-M. Flaud, R. Gamache, J. Harrison, J.-M. Hartmann, C. Hill, J. Hodges, D. Jacquemart, A. Jolly, J. Lamouroux, R. L. Roy, G. Li, D. Long, O. Lyulin, C. Mackie, S. Massie, S. Mikhailenko, H. Müller, O. Naumenko, A. Nikitin, J. Orphal, V. Perevalov, A. Perrin, E. Polovtseva, C. Richard, M. Smith, E. Starikova, K. Sung, S. Tashkun, J. Tennyson, G. Toon, V. Tyuterev, and G. Wagner, "The HITRAN2012 molecular spectroscopic database," *Journal of Quantitative Spectroscopy and Radiative Transfer*, vol. 130, pp. 4–50, Nov. 2013.

[126] S. D. Russo, M. Giglio, A. Sampaolo, P. Patimisco, G. Menduni, H. Wu, L. Dong, V. M. N. Passaro, and V. Spagnolo, "Acoustic coupling between resonator tubes in quartz-enhanced photoacoustic spectrophones employing a large prong spacing tuning fork," *Sensors*, vol. 19, p. 4109, Sept. 2019.

[127] A. Mason, *Sensing technology : current status and future trends IV*. Cham: Springer, 2014.

[128] D. G. Rabus, *Integrated Ring Resonators: The Compendium (Springer Series in Optical Sciences)*. Springer, may 2007.

[129] M. D. Carlo and G. Mantriota, "Electric vehicles with two motors combined via planetary gear train," *Mechanism and Machine Theory*, vol. 148, p. 103789, June 2020.

[130] M. R. Tucker and K. B. Fite, "Mechanical damping with electrical regeneration for a powered transfemoral prosthesis," in *2010 IEEE/ASME International Conference on Advanced Intelligent Mechatronics*, IEEE, July 2010.

[131] T. Verstraten, G. Mathijssen, R. Furnémont, B. Vanderborght, and D. Lefeber, "Modeling and design of geared DC motors for energy efficiency: Comparison between theory and experiments," *Mechatronics*, vol. 30, pp. 198–213, Sept. 2015.

[132] T. Verstraten, R. Furnémont, P. López-García, D. Rodriguez-Cianca, B. Vanderborght, and D. Lefeber, "Kinematically redundant actuators, a solution for conflicting torque–speed requirements," *The International Journal of Robotics Research*, vol. 38, pp. 612–629, Jan. 2019.

[133] W. Q. Chu, Z. Q. Zhu, J. Zhang, X. Liu, D. A. Stone, and M. P. Foster, "Investigation on operational envelops and efficiency maps of electrically excited machines for electrical vehicle applications," *IEEE Transactions on Magnetics*, vol. 51, pp. 1–10, Apr. 2015.

[134] S. D. Pinto, P. Camocardi, A. Sorniotti, G. Mantriota, P. Perlo, and F. Viotto, "A four-wheel-drive fully electric vehicle layout with two-speed transmissions,"

in *2014 IEEE Vehicle Power and Propulsion Conference (VPPC)*, IEEE, Oct. 2014.

[135] S. D. Pinto, C. Chatzikomis, A. Sorniotti, and G. Mantriota, "Comparison of traction controllers for electric vehicles with on-board drivetrains," *IEEE Transactions on Vehicular Technology*, vol. 66, pp. 6715–6727, Aug. 2017.

[136] T. Verstraten, R. Furnémont, P. López-García, D. Rodriguez-Cianca, H.-L. Cao, B. Vanderborght, and D. Lefeber, "Modeling and design of an energy-efficient dual-motor actuation unit with a planetary differential and holding brakes," *Mechatronics*, vol. 49, pp. 134–148, Feb. 2018.

[137] W. R. Brown and A. G. Ulsoy, "A passive-assist design approach for improved reliability and efficiency of robot arms," in *2011 IEEE International Conference on Robotics and Automation*, IEEE, May 2011.

[138] S. Derammelaere, S. Dereyne, P. Defreyne, E. Algoet, F. Verbelen, and K. Stockman, "Energy efficiency measurement procedure for gearboxes in their entire operating range," in *2014 IEEE Industry Application Society Annual Meeting*, IEEE, Oct. 2014.

[139] K. Stockman, S. Dereyne, P. Defreyne, E. Algoet, and S. Derammelaere, "Efficiency measurement campaign on gearboxes," in *Energy efficiency in motor driven systems, Proceedings*, p. 11, EEMODS, 2015.

[140] F. Bottiglione, S. D. Pinto, G. Mantriota, and A. Sorniotti, "Energy consumption of a battery electric vehicle with infinitely variable transmission," *Energies*, vol. 7, pp. 8317–8337, Dec. 2014.

[141] P. Lazari, J. Wang, and L. Chen, "A computationally efficient design technique for electric-vehicle traction machines," *IEEE Transactions on Industry Applications*, vol. 50, pp. 3203–3213, Sept. 2014.

[142] L. Chen, J. Wang, P. Lombard, P. Lazari, and V. Leconte, "Design optimisation of permanent magnet assisted synchronous reluctance machines for electric vehicle applications," in *2012 XXth International Conference on Electrical Machines*, IEEE, Sept. 2012.

[143] L. Chen, J. Wang, P. Lazari, and X. Chen, "Optimizations of a permanent magnet machine targeting different driving cycles for electric vehicles," in *2013 International Electric Machines & Drives Conference*, IEEE, May 2013.

[144] P. Caillard, F. Gillon, M. Hecquet, S.-A. Randi, and N. Janiaud, "An optimization methodology to pre design an electric vehicle powertrain," in *2014 IEEE Vehicle Power and Propulsion Conference (VPPC)*, IEEE, Oct. 2014.

[145] E. Carraro, M. Morandin, and N. Bianchi, "Traction PMASR motor optimization according to a given driving cycle," *IEEE Transactions on Industry Applications*, vol. 52, pp. 209–216, Jan. 2016.

[146] G. Krebs, E. de Cecco, and C. Marchand, "Design approach of an axial flux motor for electrical powertrain vehicle," in *2012 XXth International Conference on Electrical Machines*, IEEE, Sept. 2012.

[147] Y. Mao, S. Niu, and Y. Yang, "Differential evolution-based multiobjective optimization of the electrical continuously variable transmission system," *IEEE Transactions on Industrial Electronics*, vol. 65, pp. 2080–2089, Mar. 2018.

[148] S. Mallik, K. Mallik, A. Barman, D. Maiti, S. K. Biswas, N. K. Deb, and S. Basu, "Efficiency and cost optimized design of an induction motor using genetic algorithm," *IEEE Transactions on Industrial Electronics*, vol. 64, pp. 9854–9863, Dec. 2017.

[149] A. G. Sarigiannidis, M. E. Beniakar, and A. G. Kladas, "Fast adaptive evolutionary PM traction motor optimization based on electric vehicle drive cycle," *IEEE Transactions on Vehicular Technology*, vol. 66, pp. 5762–5774, July 2017.

[150] L. R. Ramelan, E. Firmansyah, T.-H. Liu, S.-K. Tseng, and J.-W. Hsu, "An improved maximum efficiency control for dual-motor drive systems," in *2014 6th International Conference on Information Technology and Electrical Engineering (ICITEE)*, IEEE, Oct. 2014.

[151] L. Mooney and H. Herr, "Continuously-variable series-elastic actuator," in *2013 IEEE 13th International Conference on Rehabilitation Robotics (ICORR)*, IEEE, June 2013.

[152] G. Mantriota, "Power split transmissions for wind energy systems," *Mechanism and Machine Theory*, vol. 117, pp. 160–174, Nov. 2017.

[153] J. Ontanon-Ruiz, R. W. Daniel, and P. R. McAree, "On the use of differential drives for overcoming transmission nonlinearities," *Journal of Robotic Systems*, vol. 15, pp. 641–660, Nov. 1998.

[154] L. Sun, K. Feng, C. Chapman, and N. Zhang, "An adaptive power-split strategy for battery–supercapacitor powertrain—design, simulation, and experiment," *IEEE Transactions on Power Electronics*, vol. 32, pp. 9364–9375, Dec. 2017.

[155] E. L. Esmail, "Meshing efficiency analysis of two degree-of-freedom epicyclic gear trains," *Journal of Mechanical Design*, vol. 138, June 2016.

[156] E. Esmail, E. Pennestrì, and A. H. Juber, "Power losses in two-degrees-of-freedom planetary gear trains: A critical analysis of radzimovsky's formulas," *Mechanism and Machine Theory*, vol. 128, pp. 191–204, Oct. 2018.

List of Publications

Journal Papers

1. C. E. Campanella, M. De Carlo, A. Cuccovillo, and V. M. N. Passaro, "Loss-induced control of light propagation direction in passive linear coupled optical cavities," *Photonics Research*, vol. 6, p. 525, Apr. 2018.

2. M. De Carlo, F. De Leonardis, and V. M. N. Passaro, "Design rules of a microscale PT-symmetric optical gyroscope using group IV platform," *Journal of Lightwave Technology*, vol. 36, pp. 3261–3268, Aug. 2018.

3. M. De Carlo, F. De Leonardis, L. Lamberti, and V. M. N. Passaro, "Generalized modeling of optomechanical forces applied to PT-symmetric optical microscale resonators," *Journal of Lightwave Technology*, vol. 37, pp. 2178–2184, May 2019.

4. M. De Carlo, F. De Leonardis, L. Lamberti, and V. M. N. Passaro, "High-sensitivity real-splitting anti-PT-symmetric microscale optical gyroscope," *Optics Letters*, vol. 44, p. 3956, Aug. 2019.

5. C. E. Campanella, M. De Carlo, A. Cuccovillo, F. De Leonardis, and V. M. N. Passaro, "Methane gas photonic sensor based on resonant coupled cavities," *Sensors*, vol. 19, p. 5171, Nov. 2019.

6. M. De Carlo, F. De Leonardis, L. Lamberti, and V. M.N. Passaro, "Dynamics of optomechanically coupled suspended silicon waveguides," *Sensors and Actuators A: Physical*, vol. 301, art. 111714, Jan. 2020.

7. F. De Leonardis, R. Soref, M. De Carlo, and V. M. N. Passaro, "On-chip group-IV Heisenberg-limited sagnac interferometric gyroscope at room temperature," *Sensors*, vol. 20, p. 3476, Jun. 2020.

8. M. De Carlo and G. Mantriota, "Electric vehicles with two motors combined via planetary gear train," *Mechanism and Machine Theory*, vol. 148, art. 103789, Jun. 2020.

9. M. De Carlo, G. Menduni, A. Sampaolo, F. De Leonardis, V. Spagnolo, and V. M. N. Passaro. "Modeling and design of a semi-integrated QEPAS sensor," *Journal of Lightwave Technology*, 2020. Published online on the 13th Oct. 2020.

10. M. De Carlo, "Exceptional points of parity-time- and anti-parity-time-symmetric devices for refractive index and absorption-based sensing," *Results in Optics*. Accepted paper (Invited).

Conference Papers

1. C. E. Campanella, M. De Carlo, A. Cuccovillo, and V. M. N. Passaro, "Investigation of methane optical sensor based on absorption induced redirection of light propagation in coupled cavities," in *20th Italian National Conference on Photonic Technologies (Fotonica 2018)*. Institution of Engineering and Technology, 2018.

2. V. M. N. Passaro, M. De Carlo, F. De Leonardis, G. Menduni, L. Lamberti, and A. G. Perri, "Parity-time and anti-parity-time-symmetry integrated optical gyroscopes: A perspective for high performance devices," in *2020 22nd International Conference on Transparent Optical Networks (ICTON)*. IEEE, July 2020.

3. M. De Carlo, F. De Leonardis, V. M. N. Passaro, "Anti-parity-time symmetry for integrated optical sensing," In *2020 OSA Frontiers in Optics (FiO)*. OSA, September 2020.